NTNU

Norwegian University of
Science and Technology

Micromagnetic modelling and magnetic force microscopy of supermagnetism in patterned nanomagnetic arrays

Anders Strømberg

Nanotechnology
Submission date: June 2018
Supervisor: Erik Folven, IES
Co-supervisor: Einar Standal Digernes, IES

Norwegian University of Science and Technology
Department of Electronic Systems

Abstract

Advanced magnetic materials have played an important role in, and continue to pave the way for, innovative technological advancements. Modern day computers, sensors, and biomedicine would not be possible without the use of such materials. Assemblies of magnetic metamaterials, comprised of a complex microscopic structure, presents a new and promising opportunity to specifically tailor nearly all magnetic properties of a material. This thesis presents an in-depth, multipronged attempt at understanding and creating specific instances of such magnetic materials with emergent ensemble properties.

Micromagnetic modeling of stable (and ground) states of such structures have been carried out. The simulation results are used to predict and verify the observation of physical instances of corresponding structures. Emergent superferromagnetic and superantiferromagnetic behavior was found for structures of different lattice geometries, in two-dimensional, patterned permalloy thin film. Of note is the long-range order of the superferromagnetic states and the indication that certain structures can be coerced into both superferromagnetic and superantiferromagnetic metastable states.

Physical structures of ordered nanomagnets were designed and later fabricated at NTNU NanoLab's cleanroom facilities. The samples were inspected through the use of magnetic force microscopy at cryogenic temperatures and subjected to varying applied magnetic fields in order to classify the structures' behavior. A stable, physical, superferromagnetic state was clearly observed and classified for triangular lattice geometries. Similar states were found for square lattice geometries, in addition to indication of the presence of a switchable superantiferromagnetic state. Additionally, several auxiliary results were obtained and auspicious suggestions for further work is provided.

Sammendrag

Sofistikerte magnetiske materialer har hatt, og fortsetter å ha, en nøkkelrolle i utviklingen av innovative, teknologiske fremskritt. Høyteknologiske datamaskiner, sensorer og biomedisinske løsninger ville ikke vært mulig uten bruken av slike materialer. Sammenstillinger av magnetiske metamaterialer, bestående av intrikate mikroskopiske strukturer, tilbyr nye og lovende muligheter for å skreddersy nærmest alle materialets magnetiske egenskaper. Denne oppgaven presenterer en dyptgående, flersidig tilnærming for å forstå og skape spesifikke eksempler av slike magnetiske materialer med emergerende ensembleegenskaper.

Mikromagnetiske modeleringer av grunntilstander, og andre stabile tilstander, for slike strukturer er blitt gjennomført. Simulasjonsresultatene blir brukt til å forutse og bekrefte observasjonen av fysiske realiseringer av tilsvarende strukturer. Fremvoksende superferromagnetisk og superantiferromagnetisk oppførsel ble påvist for strukturer med forskjellig gittergeometri i todimensjonale, mønstrede tynnfilmer av permalloy. Spesielt interessant er langtrekkende innordning i de superferromagnetiske tilstandene samt indikasjoner til at visse strukturer kan bli påvirket til å innta både superferromagnetiske, og superantiferromagnetiske, metastabile tilstander.

Fysiske strukturer av ordnede nanomagneter ble designet og senere fabrikert ved NTNU NanoLabs renromsfasiliteter. Prøvene ble inspisert gjennom magnetisk kraftmikroskopi ved kryogeniske temperaturer og utsatt for ulike, påtrykte, magnetiske felt med mål om å klassifisere strukturenes oppførsel. En stabil, fysisk, superferromagnetisk tilstand ble tydelig observert og klassifisert for triangulære gitterstrukturer. Lignende tilstander ble påvist for kvadratiske gitterstrukturer, i tillegg til indikasjoner til tilstedeværelsen av en kontrollérbar superantiferromagnetisk tilstand. I tillegg ble det funnet flere interessante tilleggsresultater, og forslag til videre, lovende, arbeid er fremlagt.

Preface

This Master's thesis was written and submitted in partial fulfillment of the requirements for the degree of Master of Science from the Norwegian University of Science and Technology (NTNU). The degree is a part of NTNU's MTNANO study program, with a main profile in nanoelectronics. The work presented herein was carried out during the spring semester of 2018, under the guidance of Professor Erik Folven at the at the Department of Electronic Systems, NTNU, and co-supervised by PhD candidate Einar Standal Digernes. All techniques and theories were developed and mastered during the course of one semester, and the thesis is not a continuation of a previous project work.

The reader should be familiar with vector notation and fundamental conceptual physics. To supplement this fundamental knowledge, a thorough introduction to relevant theory will be discussed.

I would like to thank my supervisors, Professor Erik Folven and PhD candidate Einar Standal Digernes for their great help and collaboration during the process of this thesis work.

I am grateful to Erik Folven for posing an interesting thesis problem and for trusting me to play around with advanced, and expensive, experimental equipment. With his confidence I felt free to explore the instrument and develop new routines and techniques. This has made the long hours and days in the lab both exciting and scientifically rewarding. The meetings we have had together have spurred fruitful discussions and insight which has been invaluable to the results of this thesis, and his contagious passion for the subject has been a great motivating factor.

To Einar Digernes I am grateful for his time spent teaching me the ropes of the experimental setup, debugging technical errors and partaking in in-depth discussions with Erik. His guidance through both the technical equipment and the theoretical background, as well as feedback on this thesis, has been of tremendous help and for this I am thankful. I am also particularly thankful for his contribution by fabricating the physical samples studied in this thesis, which has made the entire thesis work possible. His great competence and patience has been an inspiration for both this and further work.

The Research Council of Norway is acknowledged for the support to the Norwegian Micro- and Nano-Fabrication Facility, NorFab, project number 245963/F50.

I would also like to extend my deepest gratitude to Ragnhild Sætra, for all your love and support throughout the years.

Finally, I would like to thank my friends and fellow students at the MTNANO program, whose brilliance and initiative have made my five years at NTNU an adventure.

Trondheim, June 8, 2018

Anders Strømberg

Contents

Chapter 1

Introduction

This first chapter will provide an introduction to the thesis work. First, some motivation and historic background information supporting the research is provided. This is followed by a section that presents related work and the state of the research field. Finally, the last section provides a project outline and an overview of the work carried out in relation to the thesis.

1.1 Motivation and background

Magnetic materials have always fascinated mankind, starting with the discovery of magnetic lodestones nearly three millennia ago. The lodestones are a type of magnetized mineral (magnetite, Fe_3O_4), that were later used for navigation as a predecessor to the compass, and were believed to be of a divine origin or harbor a living soul [1]. Fortunately, our scientific understanding of magnetism, and magnetic materials, have come a long way since then. Magnetism and magnetic materials are now crucial aspects of our technological world, essential to applications such as electric power generation, biomedicine and nearly all variations of consumer electronics [2–5].

Magnetic materials have had a tremendous technological impact on the world as we know it, and continues to be studied vividly. A growing subfield of magnetism-related research is the topic of spintronics. Spintronics is a research field concerning solid-state devices where the spin of the electron is utilized as an extra degree of freedom, in addition to its charge [6]. The spin of the electron is one of the microscopic origins of magnetism, and the field of spintronics is thus closely related to magnetism. The research field of spintronics has been growing since its conception along with the discovery of spin-polarized electron injection and the observation of the giant magnetoresistive effect (GMR) [7–9]. The observation of GMR won the Noble prize in physics in 2007, a testament to the vast scientific and technological value generated from its discovery. The study and application of spintronics have accompanied the semi-conductor industry on the path to pursue Moore's law of miniaturization and is now ubiquitously utilized in electronics and

computing devices, such as magnetic random access memory (MRAM) [6].

Nanoscale magnetic materials, where components have a dimension of submicron-size, have in the last few decades been a hot research topic and are suspected to bring about immense scientific and technological innovation [10, 11]. Miniaturization of technology, utilizing nanoscale magnetic components, allows for the possibility of high resolution imaging techniques with single-spin sensitivity, and high density, high speed magnetic storage devices [3, 12]. However, as these technologies based on down-scaling reach their fundamental limits, new solutions using different approaches must be explored in order to facilitate technological progress [3, 13, 14].

One way to battle current and future obstacles is to develop and apply new concepts in the design and fabrication of materials and components. One example of such new concepts is the emergent properties of assemblies of microstructures [15–17]. While textbooks and popular science are primarily concerned with presenting the simple, non-interacting microscopic states, the real world surrounding us is comprised of a multitude of interacting microscopic states acting as holistic systems with emergent behavior. An analogy, by example, to this so-called emergent behavior is the property of superconductivity. One atom alone cannot be superconducting, it is first through the assembly of a sufficient number of atoms that the property of superconductivity arises. The same principle can apply for other medium properties as well.

With the advent of fabrication techniques allowing for the precise structuring of magnetic materials in the form of nanoscale magnets, emergent properties of ensembles of such nanomagnets may provide new, novel material solutions. Properties such as superparamagnetism and superferromagnetism are examples of such emergent behavior and can be referred to collectively as supermagnetism [10].

The presence of such emergent properties opens up the possibility of tailoring specific magnetic and material properties, dependent on the ensemble parameters rather than the intrinsic material parameters. Applications of such structures might combine ensemble and material properties in order to meet desired material specifications, such as soft magnetic materials for high frequency imaging or nanomagnetic logic for ultra-low energy computing [18–20].

One interesting, proposed application of ensembles of interacting magnetic particles might be found in the area of unconventional computing. Unconventional computing is an alternative approach to boolean information processing, i.e., it strays from the omnipresent transistor, and explores systems where the whole behaves as more than the sum of its components, often utilizing magnetic structures [21].

1.2 Related work

There have been many studies directed towards the ensemble properties of self-assembled magnetic structures [22–26]. Some of these assemblies have shown supermagnetic behavior such as superparamagnetism in otherwise non-magnetic materials [27]. However,

a significant disadvantage to the bottom-up self-assembly approach is the inherent lack of control and reliance on thermodynamically metastable structures. If a change in the geometry of the ensemble structure is desirable, oftentimes a completely new system of self-assembly would be needed. A more rigorous, although sometimes time- and resource intensive, approach is to use a top-down fabrication method which gives complete control of the desired structure.

A top-down approach of patterning magnetic thin films is not a new approach in and of itself [28]. In fact, it is a well-developed process, utilized in the production of magnetic storage devices among other things, and it is generally considered a well-understood topic [29–31]. However, these approaches has focused on larger structures and have avoided interaction across magnetic regions in order to reduce unwanted cross-talk. In a supermagnetic metamaterial, however, the interaction between magnetic regions is desired, and indeed required, as it is the origin of the emergent properties of the ensemble. The use of structured magnetic thin films for the purpose of assembling *in-plane* magnetized materials with supermagnetic emergent behavior has not been investigated thoroughly. However, a recent study by Bedanta et al. [32] has presented indications of superferromagnetic behavior in *out-of-plane* magnetized nanodots.

There has, however, been efforts to *model* ordered arrays of nanomagnets that behave as an ensemble with supermagnetic properties. In a recent paper by Slöetjes et al. [33], ensembles of ordered, circular disks of an oxide ceramic material (LSMO) was simulated and found to exhibit various forms of supermagnetic ensemble properties. This thesis will build on the observations of Slöetjes et al. and go a few steps further. The oxide ceramic material will be replaced by a simpler alloy of nickel and iron, which is easier to fabricate, and in addition to micromagnetic simulations, real life tests of the ensembles will be performed.

If a long range, supermagnetic behavior can be observed in the fabricated samples, it will be a first indication of experimentally, well-controlled, in-plane supermagnetism in two-dimensional arrays. Additionally, the physical presence of a switchable superferromagnetic–superantiferromagnetic structure would present a completely new and exotic material system, which could have a multitude of use cases. Such switching would effectively enable a low-energy transition between net magnetized and demagnetized states.

1.3 Project outline

The work carried out in this thesis can be divided into two main parts, micromagnetic simulations, and imaging and manipulation of fabricated samples.

The simulation efforts presented here aims to demonstrate, characterize and probe the supermagnetic behavior and properties of nanomagnetic ensembles in permalloy thin films. These simulations are similar to the work carried out in a recently published paper by Slöetjes et al. [33], except that the magnetic material parameters in this work is

typical of a thin film of permalloy. The observation of qualitatively similar results show that the ensemble structure dominates the supermagnetic behavior, rather than the use of an exotic oxide material.

The second part of the thesis involves the fabrication, manipulation and imaging of structures corresponding to the simulated ensembles. As presented in this thesis, the work might appear to have been carried out sequentially, although that is not the case. Both simulations and physical experimental work were carried out in parallel, and knowledge acquired in either part could be utilized to gain understanding and spur further investigations in the other part.

In the following chapter, a theoretical foundation for magnetism, the micromagnetic model, and supermagnetism will be provided. Additionally, a brief theoretical introduction to the experimental techniques utilized in the thesis work will be given.

Following the chapter on theory, Chapters 3 through 5 will give specific detail of the methods and implementation used to carry out the different parts of the thesis work. Here, general methodology will be covered, while specific setups for specific results will be provided along with the results themselves.

Chapter 6 will present the obtained results and Chapter 7 will attempt to explain the observations through discussion based on the theoretical foundation in Chapter 2, as well as the techniques described in the methods chapters (Chapters 3 through 5).

Finally, Chapter 8 will summarize and provide a conclusion based on the discussed results. This chapter will also provide suggestions and ideas for further research. The chapter will, in addition to suggestions regarding the main results, also comment on further investigations of the auxiliary results.

Defining a coordinate system

As there will be discussions of three-dimensional systems and directions, a formal definition for a consistent coordinate system utilized in this thesis is appropriate. The coordinate system chosen is defined relative to the magnetic structure's (or the sample's) orientation. All structures will lie on a mutual plane, which will mostly be presented in the thesis as the plane of the paper sheet. The directions $\hat{\mathbf{x}}$ and $\hat{\mathbf{y}}$ will lie in the plane, and as a convention the x-axis will be aligned horizontally to the right, and the y-axis will be aligned vertically up. The z-direction will thus be pointing out-of-plane. This convention is particularly useful when also discussing the tip orientation of the MFM scans. A representation of the chosen coordiante system is conveyed in Figure 1.1

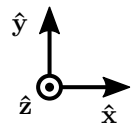

Figure 1.1: The coordinate system utilized in this thesis. The plane of the paper is parallel to the plane of the magnetic structures presented.

Chapter 2

Theory

This chapter will present the theoretical background needed to understand and discuss the methods and observations in this thesis. The chapter consists of three main parts. First, a section on classical magnetism is provided, where the concept of magnetism is thoroughly introduced in a way that facilitates the following discussion. Subsequently, the micromagnetic model is introduced, where the dynamics of magnetism in microscopic structures are formulated. Finally, the exotic topic of supermagnetism is discussed using the provided theoretical foundation of classical magnetism and the micromagnetic model.

2.1 Classical magnetism

In order to discuss the topic of the more advanced magnetic behavior studied in this thesis, it is necessary to provide a fundamental theoretical framework for traditional magnetism. This section will cover basic magnetism and magnetic material concepts useful to describing the project work and results.

The word *magnetism* is colloquially used to describe a set of related physical properties and phenomena, including magnetic fields, magnetic moments, and circulating currents. This section will not focus on the history of magnetism, briefly mentioned in the previous section, but will derive the fundamental physical description. As stated in Spaldin [34], there are mainly two complimentary routes for developing a fundamental magnetic theory; One involving a purely physicist's view of circular currents. The other, an engineer's approach, of considering magnetic poles. Of course, there are other approaches, such as considering magnetism the side effect of relativistic electrostatics, but such discussion is wide outside our scope [35]. For this thesis, the magnetic pole approach will be the most relevant as it fortunately provides a well-suited, bridging analogy for the concept of supermagnetism. However, in regards to physical units, the text will adhere to the Système International (SI) units and physical constants.

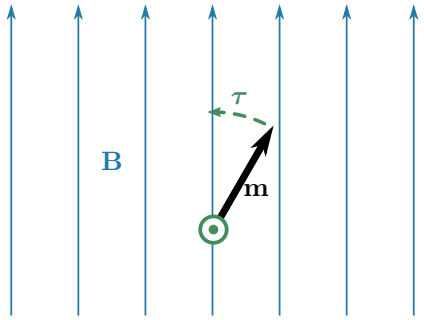

Figure 2.1: In an externally applied magnetic field, **B**, a magnetic dipole moment, **m** will tend to align itself along the magnetic field exerting a torque $\boldsymbol{\tau}$, as expressed in Equation 2.1.

2.1.1 Magnetic moment

The fundamental physical unit and origin of magnetism can be considered to be the magnetic dipole moment, or simply the magnetic moment. The magnetic dipole moment is the concept of a magnetic unit with two distinct ends, a north and a south pole, from which a solenoidal (divergence free) magnetic field is originating. Classical electromagnetic theory, as developed from Maxwell's equations [36], dictates that the magnetic field *must* be solenoidal, implying that magnetic monopoles cannot exist. Thus, the most basic magnetic moment is the magnetic dipole moment, similar, in many aspects, to the familiar bar magnet of everyday life.

A magnetic moment can be described as a vector, often denoted **m**, in that it has an orientation and a magnitude. The direction of the vector indicates the orientation of the north and south pole, and the magnitude indicates the strength of the interaction with an external magnetic field. More formally, when a magnetic moment, **m**, experiences an external magnetic field, **B**, it will tend to orient itself along the external field, exerting a torque, $\boldsymbol{\tau}$ to do so. Mathematically, the relation is expressed as [37]

$$\boldsymbol{\tau} = \mathbf{m} \times \mathbf{B}, \tag{2.1}$$

and since torque is expressed in units of N m (Newton meter) and the magnetic field in $\mathrm{T} = \frac{\mathrm{N}}{\mathrm{A\,m}}$ it is clear that the corresponding units of the magnetic moment is $\mathrm{A\,m^2}$ (which is intuitively correct if the approach of circular currents is considered, where the moment can be measured as a current in a loop enclosing an area) . An illustration of the torque-relation can be found in Figure 2.1. A magnetic moment that is not parallel to the field will be subject to a precession (Larmor precession) around the magnetic field direction (assuming some angular momentum). However, a magnetic moment that is parallel to the field, $\mathbf{m} \parallel \mathbf{B}$, will be in the minimum energy state.

There are many physical examples of objects that can be described as instances of the magnetic moment. To provide a first, physical counterpart to the *theoretical* magnetic

moment we can consider the magnetic moment of an atom. Atoms' magnetic moment mostly originates from the electrons in the atoms. The electrons themselves have an intrinsic magnetic moment due to their spin, which contributes with approximately one Bohr magneton, $\mu_B \approx 9.27 \times 10^{-24}\,\mathrm{A\,m^2}$ [4, 38]. In addition to the intrinsic moment, the electrons will have a magnetic moment associated with their orbital angular momentum, which will be in the same order of size as μ_B, making it convenient to express atomic magnetic moments in terms of the physical constant μ_B. The nucleus of the atom will contribute negligibly, and the atomic magnetic moment can (quite accurately) be expressed as a sum of the moments of its electrons [39].

However, since electrons in an atom pair up with electrons of the opposite spin, thus canceling each other's magnetic moments, a vast majority of atoms have a weak total magnetic moment. The vanishing net moment of electron pairs also makes it clear that the magnetic moment of atoms will depend on its electron *configuration*, which in turn can lead to interesting insights into the behavior of magnetic materials. In the following sections, the described microscopic origin of magnetism will be applied to describe the various types of macroscopic magnetism found in different types of materials.

2.1.2 Magnetic materials

Paramagnetism and diamagnetism

All materials must consist of some atoms with a specific atomic magnetic moment. For simplicity, we will refer to the atomic magnetic moment as $\boldsymbol{\mu}_m$. If the atomic magnetic moment is sufficiently weak (or the material structure is so that strong atomic moments are sufficiently separated) an atom's moment, $\boldsymbol{\mu}_m$, will not interact with its neighbors. In the absence of an externally applied field, each atom's moment will be oriented in a random direction. Thus, for any macroscopic material it is clear that $\sum \boldsymbol{\mu}_m = 0$, and the material's macroscopic magnetic moment will be non-existent. Instead of referring to the total magnetic moment of a material (which would incorporate the size of the material), it is common to express an average **magnetization** relating a small volume element, dV to its corresponding magnetic moment $d\mathbf{m}$,

$$\mathbf{M} = \frac{d\mathbf{m}}{dV}. \tag{2.2}$$

Thus, for linear and homogeneous materials the magnetization will be independent of its size.

In the previous example no external field was assumed. However, if the material is introduced to an external magnetic field, the microscopic atomic moments will experience a torque as described in Equation 2.1, and a total magnetic moment, $\sum \boldsymbol{\mu}_m \neq 0$, or a non-zero magnetization, $\mathbf{M} \neq 0$, will arise. The degree to which materials respond to magnetic fields in these weakly magnetic materials is the susceptibility, χ, which is defined through the relation

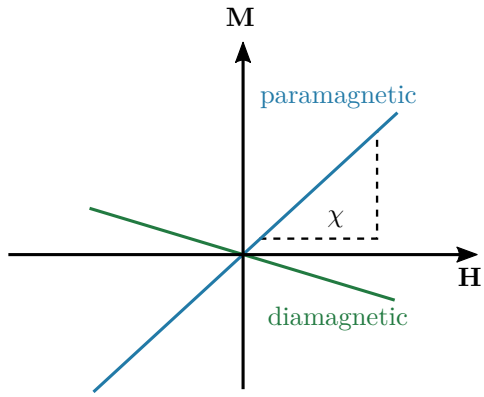

Figure 2.2: Typical magnetization response of paramagnetic (blue) and diamagnetic (green) materials in an applied field **H**. Critical to the illustration is the smaller magnitude in the response of diamagnetic materials. Also indicated is the slope of the paramagnetic material, signifying the susceptibility, χ. Note that at $\mathbf{H} = 0$, the magnetization is unequivocally zero for both materials.

$$\chi \mathbf{H} = \mathbf{M}, \tag{2.3}$$

where **H** is defined by $\mathbf{B} = \mu_0 \mathbf{H} + \mathbf{M} = \mu_0 (1 + \chi) \mathbf{H}$, and $(1 + \chi)$ is often denoted as the relative permeability, μ_r.

The sign of χ distinguishes between two types of weakly magnetic materials, paramagnetic ($\chi > 0$) and diamagnetic ($\chi < 0$) materials. A negative susceptibility, such as found in diamagnetic materials, indicates that the atomic moments will align opposite to the direction of the applied field. The mechanisms behind diamagnetism are not relevant and will not be covered here, but it is worth noting that *all* materials exhibit some diamagnetism but the effect is usually trivial compared to the other magnetic contributions.

Both paramgnetism and diamagnetism are examples of weak magnetic effects, where the material's constituent microscopic magnetic moments do not interract in a significant manner compared to the contribution from thermal energy, $k_{\mathrm{B}}T$. However the paramagnetic response is usually greater than the diamagnetic, and an illustration of the magnetization response (of para- and diamagnetic materials) to an external field is provided in Figure 2.2.

A natural objection to the presented theory on these weak magnetic responses would be to point out that there is seemingly nothing working against the mutual orientation of atomic moments along the applied field. Using a paramagnetic material as an example, the driving force behind favoring randomly oriented moments can be explained by thermal energy. First, consider the potential energy of a single atomic moment, $\boldsymbol{\mu}_m$ in an applied field **B** which can be formulated from Equation 2.1,

$$U = -\boldsymbol{\mu}_m \cdot \mathbf{B}. \tag{2.4}$$

For a paramagnetic material at a reasonable temperature, the energy gained by aligning with the field is much less than the available thermal energy $k_{\mathrm{B}}T$. Thus, the paramagnetic material's microscopic moments will flip in random orientations due to thermal energy, and only under a finite external field will there be a finite probabilistic favoring of aligning with the field. Note that the term *reasonable temperature* is used here, which is a subjective term and indicates the seemingly paradoxical fact that paramagnetic materials are not paramagnetic at all temperatures. The effect of temperature on the net magnetization will be covered in the subsequent sections.

Ferromagnetism

Ferromagnetism (FM) is the type of magnetism that most are familiar with from everyday life. In the FM set of materials, the microscopic magnetic moments are interacting and this leads to collective behavior that is distinctly different from the weakly magnetic materials. One of the most significant differences is the materials' ability to retain a remanent magnetization, even at no applied external field. This remanent magnetization stems from a long-range order that is possible in the material because the microscopic moments interact, and thus not only favor aligning along the external field, but also along the direction of the surrounding material's magnetic moment.

An example of a ferromagnetic material, and from which the set of materials gets its name, is iron (latin: ferrum). However, all pieces of iron are not permanent magnets, meaning that they do not have a finite net magnetization, even though their microscopic magnetic moments favor self-coherent alignment. Demagnetized FM materials (where microscopic spins favor alignment) can be explained by the existence of magnetic domains, separate regions of the material that will have a uniform magnetization. The magnetic moment of a particular domain does not necessarily align with other domains in the material. Thus, the total magnetization, summed over all the material's domains, can be trivial. The topic of magnetic domains is essential to this thesis and will be covered more in-depth in Section 2.1.3.

There is no doubt, however, that ferromagnetic materials can be permanently magnetized. This behavior is best captured through a discussion of magnetic hysteresis. A piece of ferromagnet that has never experienced an external field might have zero net magnetization. Applying and increasing a magnetic field, however, more and more of the internal magnetic moment will align in parallel. This will continue until the material reaches a state where an increase in the applied field will not yield an increase in the material magnetization. At this point, the magnetization level is saturated, which gives name to the quantity of saturation magnetization, $\mathbf{M}_{\mathrm{S}}$.

The next step in the hysteresis treatment is to decrease the applied field, resulting in a slow decline in the material's magnetization. At zero applied field, the ferromagnetic material will still retain some magnetization, the remanent magnetization, $\mathbf{M}_{\mathrm{r}}$. Decreasing the applied field further, by applying a magnetic field opposite to the initial direction, will further decrease the magnetization in the ferromagnetic material. At the point where

the material, yet again, exhibits zero net magnetization, the strength of the applied field is termed the coercivity of the material, $\mathbf{H}_c$, a measure of the material's "magnetic resilience". If the process is allowed to continue until negative magnetization saturation, and back to positive saturation, it will form a complete loop known as the hysteresis loop. This hysteresis loop is illustrated in Figure 2.3.

However, as mentioned in Section 2.1.2, the behavior of magnetic materials is temperature dependent. A ferromagnet's magnetic moments may be prone to switching between random orientations, given sufficient thermal energy. Thus, at high temperatures, an otherwise ferromagnetic material will behave as a paramagnet. The critical temperature where this behavior change occurs is termed the Curie temperature, T_C. Ferromagnetic materials at a temperature $T < T_\mathrm{C}$ will exhibit ferromagnetic behavior, but at a temperature $T > T_\mathrm{C}$, they will behave as paramagnetic materials.

Antiferromagnetism

There are other arrangements of magnetic moments that include strong interaction between moments. One example of this is antiferromagnetic behavior. Antiferromagnetic materials have neighboring moments oppositely aligned, effectively canceling each other's magnetic moments, resulting in a zero net magnetization. As the magnetic moments do not sum up to a significant magnetization, an antiferromagnetic material can be magnetized under an applied field, but will exhibit no remanent magnetization when the field is removed.

A closely related group of magnetic materials are the ferrimagnetic materials. These also have strongly interacting microscopic moments that are oppositely aligned with their neighbors, but the microscopic moments are not of the same magnitude. Until now we have assumed that all microscopic moments are identical, $\boldsymbol{\mu}_m$, however, this is not the case for all materials. This imbalance of moments leads to a non-zero net magnetization of ferrimagnetic materials, similar to the ferromagnetic case. And, just like the ferromagnetic materials, ferrimagnetic materials can retain remanent magnetization. This group of materials have found special use in magnetic storage devices for their ability to quickly change magnetization direction under an applied field. An interesting fact is that the very first discovered magnet, the lodestone mentioned in Section 1.1, is indeed a ferrimagnetic material [40].

An illustration of the microscopic magnetic moment distributions of antiferromagnetic and ferrimagnetic materials is provided in Figure 2.4.

2.1.3 Magnetic domains

As mentioned in Section 2.1.2, the microscopic magnetic moments can exhibit long-range order over a region of the material, a so-called magnetic domain. For a macroscopic material this order will not extend through the entire structure. Thus, for strongly coupled magnetic materials (i.e., ferro-, antiferro- and ferrimagnetic materials) the magnetic sub-

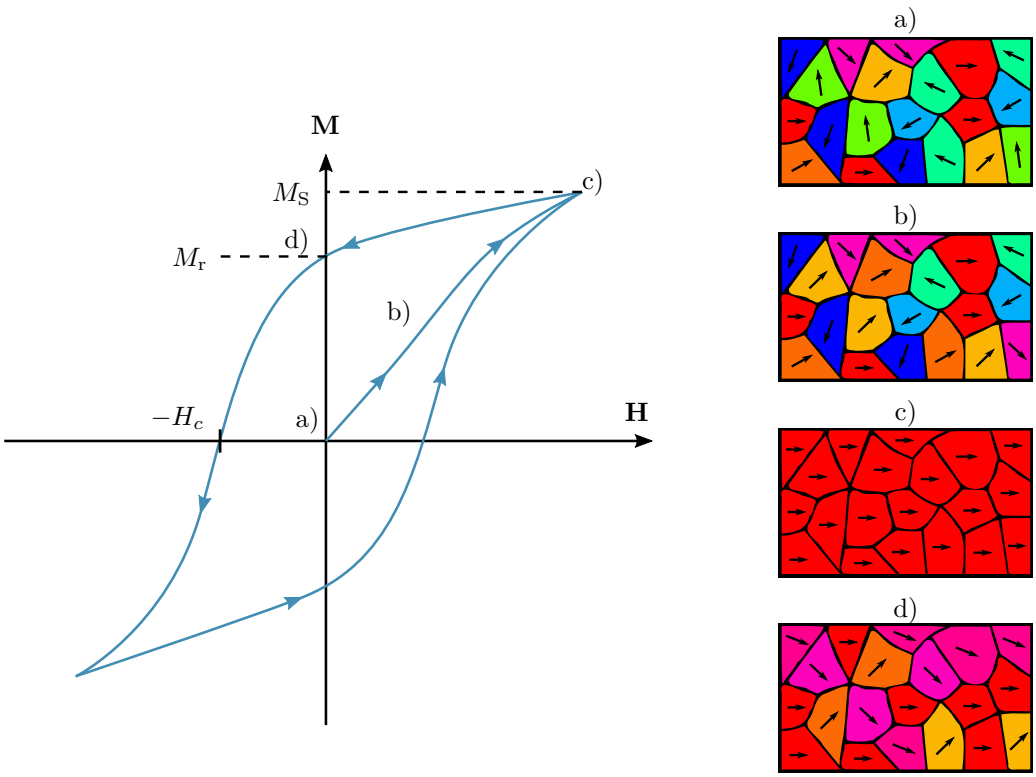

Figure 2.3: **Left:** Hysteresis curve of a ferromagnetic material. a) The relaxed ferromagnet with zero net magnetization. b) Increasing magnetization as more and more magnetic domains align along the applied field. c) Magnetization saturation, all possible magnetic moments are aligned with the field. d) The ferromagnet is yet again relaxed and retaining a remanent magnetization $\mathbf{M}_\mathrm{r}$. Also indicated is the coercivity, $\mathbf{H}_c$. **Right:** The magnetic domains of the ferromagnet at corresponding parts of the hysteresis curve. The domains are treated as individual magnetic moments of different magnitude. a) The material in its demagnetized state. Neighboring domains are not aligned, and all domains are randomly aligned resulting in a zero net magnetization. b) An increasing external magnetic field has begun to orient the domains along the magnetization direction (pointing to the right) resulting in a small net magnetization. c) Magnetization saturation, $\mathbf{M}_\mathrm{S}$, is reached. All possible moments are aligned with the applied field. d) The field is removed and the ferromagnetic material retains some remanent net magnetization, $\mathbf{M}_\mathrm{r}$. Note that this figure is a simplified illustration, as in reality the shapes and sizes of the domains can deform and shift.

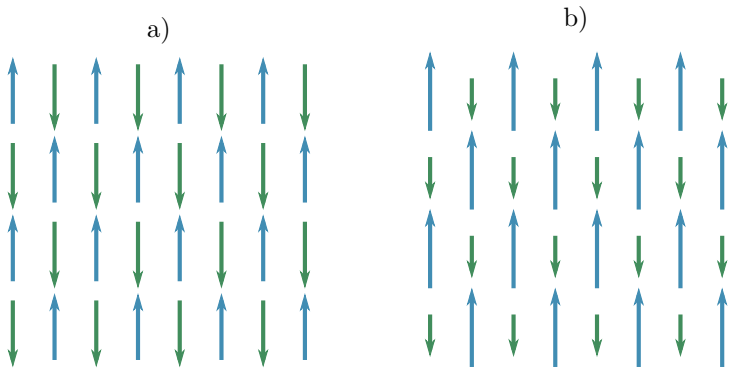

Figure 2.4: Illustration of magnetic moment distribution in a) antiferromagnetic materials and b) ferrimagnetic materials. Note that the net magnetization is zero in the antiferromagnetic case, but non-zero (along the blue direction) in the ferrimagnetic case.

stance will be divided into several magnetic domains. These domains can in turn have no net magnetization (antiferromagnetism) or significant net magnetization (ferro- and ferrimagnetism), but do not necessarily align with the magnetization of surrounding domains. These domains can thus be modeled as a single magnetic moment with a single direction and a magnitude that is proportional to the size of the domain. However, modeling a domain as a constant magnetic moment is a rather simple model, as it does not allow for the domain walls to change or move.

An example illustration of ferromagnetic domain structures, and its correspondence to the process of hysteresis is provided in Figure 2.3.

Of special significance to this thesis is the fringe case of magnetic structures containing only a single magnetic domain. Structures with a single magnetic domain is physically realizable if the magnetic structure itself is small enough that it is not energetically favorable to form domain walls within it. Such a magnetic structure, typically a magnetic nanoparticle, is termed a single-domain, or monodomain, magnet and will be discussed much throughout this thesis. A discussion of such monodomain nanoparticles will be provided in Section 2.2. Figure 2.5 provides a conceptual illustration of how a monodomain magnet may be fashioned from a ferromagnetic material.

The driving mechanisms for forming domains and domain walls will be covered more in-depth in the following section.

2.2 The micromagnetic model

In this section, the theoretical basis for the micromagnetic model will be provided. However, more specific information regarding how micromagnetic systems can be simulated on a computer by applying the micromagnetic model's concepts is covered in Chapter 3.

Now that the fundamental concepts of the different types of magnetic materials have been introduced, it is useful to provide a more quantitative model describing the inter-

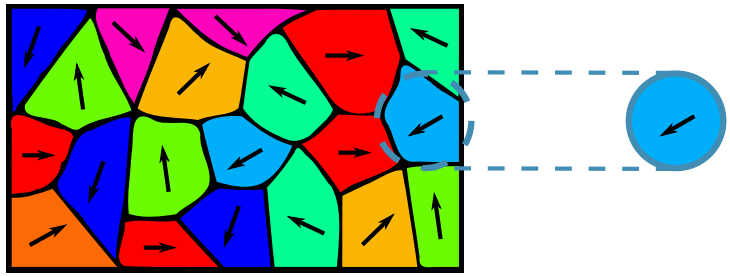

Figure 2.5: Illustration demonstrating how a small particle of a ferromagnetic material can be sufficiently small so that it contains only a single domain.

actions and energy contributions in a more detailed system. This section will present the so-called micromagnetic model. Relevant to the discussion are several energy terms, associated with internal states of the material, and the driving force towards equilibrium is the minimization of a system's total free energy.

The micromagnetic model is a so-called continuum approximation for magnetic solids, where the concept of individual atoms contributing to the magnetization with a magnetic moment is simplified. Instead, the continuum (i.e., space) is divided into discrete cells of uniform magnetization, which may contain a very large amount of atoms. For simplicity, we will denote the magnetization of a material by the relation

$$\mathbf{M} = M_{\mathrm{S}}\hat{\mathbf{m}}, \tag{2.5}$$

where M_{S} is the material's saturation magnetization and $\hat{\mathbf{m}} = \hat{\mathbf{m}}(\mathbf{r})$ is the magnetization unit vector as a function of the spatial coordinate $\mathbf{r}$. Thus, a magnetic material can be divided into discrete cells with a magnetization magnitude M_{S} and an orientation $\hat{\mathbf{m}}$. The description of magnetization assumed in Equation 2.5 is clearly valid for all materials with a well-defined $M_{\mathrm{S}}(\mathbf{r})$, given the continuum approximation.

2.2.1 Magnetic energy terms

Exchange energy

Up until this point, discussion of the interaction between microscopic magnetic moments has been limited to simply whether or not they tend to interact and whether the interaction is parallel or antiparallel. The driving force behind the aligning interaction is called the exchange coupling interaction. The exchange coupling interaction has its origin with the electrons of the material and their magnetic moments. The magnetic moment of an electron in an atom is comprised of both its intrinsic spin contribution and the orbital angular momentum contribution, both of which are quantum mechanical degrees of freedom. According to the Pauli principle, two fermions (e.g. electrons) may not occupy the same quantum state, which dictates that two electrons of the same orbital configuration must have oppositely aligned spins and thus approximately zero magnetic moment. How-

ever, states where multiple electrons have parallel spins (and thus a significant magnetic moment) are possible if the electrons have separate orbital angular momentum configurations. Electrons with parallel spins in separate orbital states can be favorable due to less coulombic interactions, decreasing the free energy of the system. For further details on the quantum mechanical mechanisms behind such configurations, the reader is referred to Kronmüller and Fähnle [41].

In quantitative terms, we can write the exchange energy as [4]

$$E_{\text{exch}} = -\frac{\mu_0 M_{\text{S}}}{2} \int_V \hat{\mathbf{m}} \cdot \mathbf{H}_{\text{exch}} \mathrm{d}V, \tag{2.6}$$

where the exchange field, $\mathbf{H}_{\text{exch}}$, is defined by

$$\mathbf{H}_{\text{exch}} = \frac{2A_{\text{exch}}}{M_{\text{S}}^2} \boldsymbol{\nabla}^2 \hat{\mathbf{m}}. \tag{2.7}$$

In Equation 2.7, the term A_{exch} denotes the exchange stiffness, a material parameter of units $\mathrm{J\,m^{-1}}$, related to the magnetic torque exerted by two neighboring magnetic moments.

From Equation 2.6, it is clear that the energy associated with the exchange coupling, E_{exch}, will be minimized by aligning all microscopic moments in the material. However, an alignment of all microscopic moments in an entire material is not the observed behavior of macroscopic ferromagnets. Recalling the formation of magnetic domains as discussed in Section 2.1.3, it is clear there must be other contributions to the system's total free energy which does not favor aligning *all* microscopic magnetic moments.

Magnetostatic energy

In a monodomain ferromagnet, the net magnetization will be significant. Since the magnetic field must be a divergence free field, the magnetic material must sustain a magnetic stray field outside the material. The stray field is associated with a high energy cost, and works against the magnetization of the ferromagnet which is why it is often referred to as the demagnetizing field, $\mathbf{H}_{\text{d}}$. The energy associated with the demagnetizing field can be found in a similar fashion to Equation 2.6, by considering the interaction of the material's magnetization with the field. This gives the relation,

$$E_{\text{demag}} = -\frac{\mu_0 M_{\text{S}}}{2} \int_V \hat{\mathbf{m}} \cdot \mathbf{H}_{\text{d}} \mathrm{d}V, \tag{2.8}$$

and since $\mathbf{H}_{\text{d}}$ and the magnetization direction, $\hat{\mathbf{m}}$ are oppositely aligned, the E_{demag} term is minimized only by a small stray field, $\mathbf{H}_{\text{d}}$.

Thus, there is a competing energy term to balance the domain forming E_{exch} term, the E_{demag} term. Magnetic domain formation is a balance between minimization of both these two terms. The dual competition between E_{exch} and E_{demag} is illustrated in Figure 2.6.

Looking at Figure 2.6 while considering Equation 2.6, it is rather obvious that the

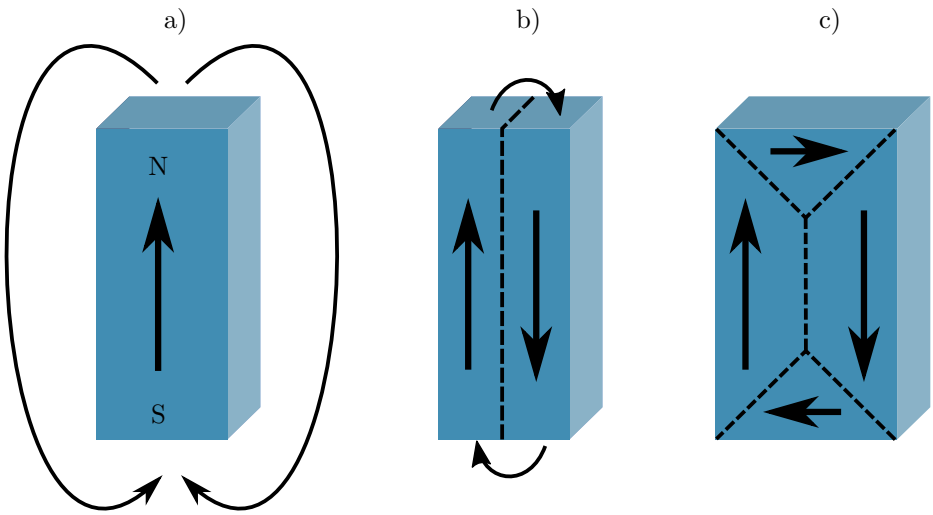

Figure 2.6: Illustration of domain formation. a) A hypothetical bar magnet with a single magnetic domain. This single domain configuration leads to a minimum E_{exch}. However, a high E_{demag} makes it an unstable configuration. b) A second domain is introduced, drastically minimizing the E_{demag} contribution at the expense of an increase in E_{exch}. c) The introduction of two new domains has seemingly totally minimized E_{demag}, although with a further increase in E_{exch}. Exactly how the domains of a magnet will arrange themselves depend on the exact quantitative magnitudes of the magnetostatic energy and the exchange energy.

increase in exchange energy only occurs at the domain walls, indicated by the dashed lines. Through the bulk of each individual domain, the magnetization is uniform and aligned with $\mathbf{H}_{\text{exch}}$. It is only at the domain borders that an energy increase can be observed. Thus, it is not the amount of distinct domains that contributes to an increase in free energy, but the amount of domain wall.

A domain wall is not a discrete change in magnetization direction, but is a gradual turning of the magnetization over a finite width, δw. The thickness, δw, of a domain wall is determined (mostly) by the exchange stiffness of the material A_{exch}. Thus, the domain wall is a small, magnetically frustrated volume that is proportional to the boundary areas, and the wall thickness, of each domain. An illustration of the domain wall and its frustrated microscopic moments is provided in Figure 2.7.

The formation of new domains is governed by the free energy balance between minimizing the energy cost of the domain boundaries and the energy cost of the stray (demagnetizing) field. As mentioned, the domain walls are not discrete boundaries, but a volume of material where the magnetic moments are changing over a certain width, δw. The domain wall volume will be smaller if the change in magnetic moment can occur over a shorter width, and thus the amount of frustrated microscopic moments will be reduced. In other words, a thinner domain wall will be energetically favorable as there is less energy cost associated with the exchange energy. The exchange stiffness, A_{exch}, that determines

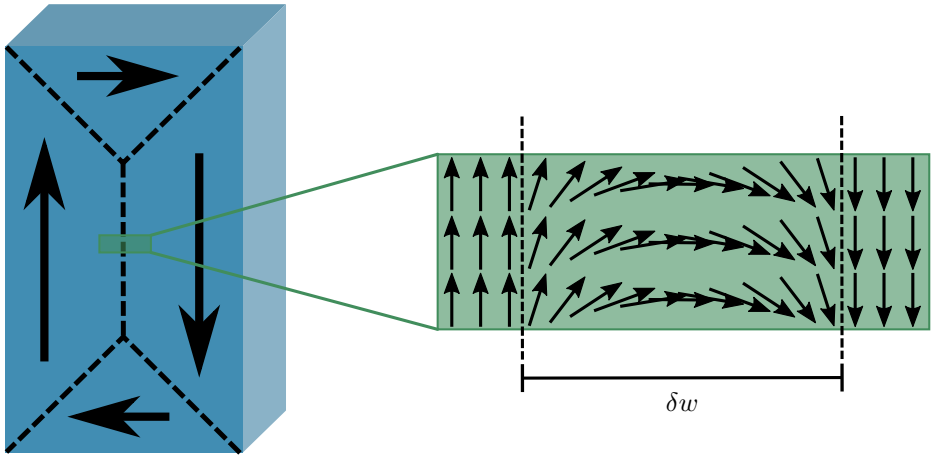

Figure 2.7: The microscopic magnetization of a domain wall between two oppositely aligned domains is illustrated in the green inset. Note that type of domain wall illustrated here, where the magnetization orientation turns in plane, is an example of a Néel wall, typical of magnetic thin films. The other configuration, more common in bulk magnets, is Bloch orientation where the magnetization turns out of plane forming a helix-like shape. Also indicated is the domain wall width δw.

the domain wall thickness can thus be expressed as a change in polar angle, $\delta\phi$, that the material can sustain over a small distance, δl. An illustration of the exchange stiffness and its effect on the width of a domain wall is provided in Figure 2.8.

The magnetostatic energy is also the main driving mechanism behind so-called shape anisotropy. Shape anisotropy is the effect that the geometrical confines (in other words the shape) of a magnetic object will dictate which direction or set of directions that the magnetization will tend to align along. Non-spherically shaped ferromagnets will have preferred magnetization directions where the stray field is minimized. The favorable alignment of magnetic moment along the length of an object can be intuitively understood by considering a long bar magnet. A magnetization direction along the length will align H_d so that it is much smaller than if the magnetization were to be oriented perpendicular to the long axis. A spherical magnet on the other hand, cannot exhibit shape anisotropy due to its complete symmetry.

Applied field energy

There is a magnetic interaction between the externally applied field, $\mathbf{H}_\mathrm{ext}$, and the magnetic moments of a material. The energy contribution due to this interaction is simply

$$E_\mathrm{ext} = -\mu_0 M_\mathrm{S} \int_V \hat{\mathbf{m}} \cdot \mathbf{H}_\mathrm{ext} \mathrm{d}V. \tag{2.9}$$

Minimizing this energy contribution is the driving force causing the magnetization to tend to align along the applied field. The energy contribution described in Equation2.9

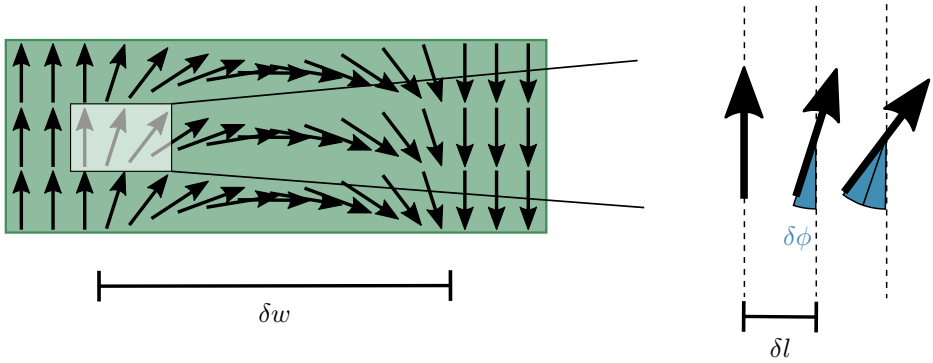

Figure 2.8: The domain wall width is dictated by the exchange stiffness, which may be visualized as the possible change in magnetization angle, $\delta\phi$, over a finite length, δl, in any given material.

is sometimes called the Zeeman energy [4].

Magnetocrystalline anisotropy

Inherent to some magnetic materials is an anisotropy related to the crystallographic structure of the material. The property of crystal-dependent magnetic anisotropy is called the magnetocrystalline anisotropy, and it describes how the magnetization of the material will favor aligning along certain crystallographic directions. The directions which are favored are termed the easy axes, and the directions which are the least favored are termed the hard axes. If a system only has a single axis of high symmetry, it is termed a uniaxial anisotropic system. Thin films of complex oxide systems, such as (001) oriented $La_{0.7}Sr_{0.3}MnO_3$ (LSMO) can have two sets of easy axes, making it a biaxial anisotropic system [42].

Magnetocrystalline anisotropy is associated with an energy contribution related to the degree of symmetry. For a certain magnetization direction in a uniaxial system this contribution can be expressed as

$$E_{\text{anis}} = \int_V K_{u1} \sin^2 \theta \mathrm{d}V, \tag{2.10}$$

where K_{u1} is the material (crystal) first order uniaxial magnetocrystalline anisotropy constant, and θ is the angle difference between the magnetization and the easy axis orientations.

An illustration of magnetocrystalline anisotropic (and isotropic) magnetization behavior is provided in Figure 2.9. For the iron-nickel alloy named permalloy (Py), the material most studied in this thesis, the magnetocrystalline anisotropy is negligible [43].

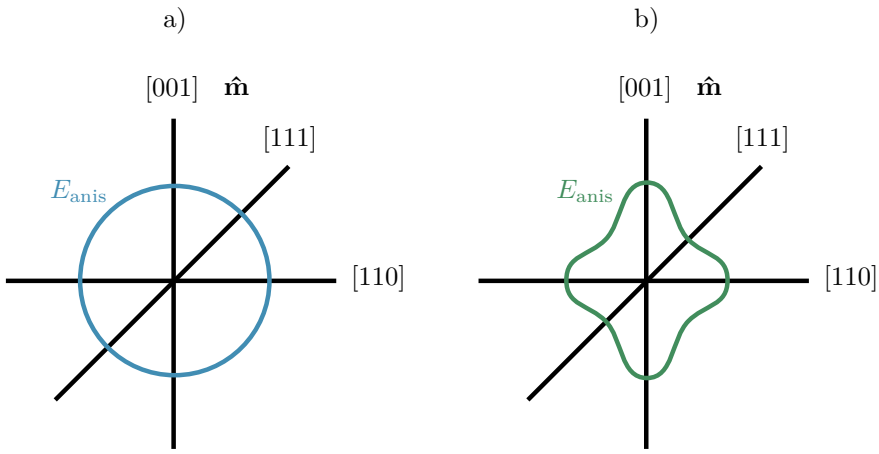

Figure 2.9: Magnetocrystalline anisotropy energies, for a given magnetization direction, $\hat{\mathbf{m}}$, along indicated crystallographic directions. a) No magnetocrystalline anisotropy, the direction of magnetization has no effect on the magnetocrystalline anisotropy energy. b) Magnetocrystalline anisotropy, clearly showing a set of easy axes with energy minima along [111] and hard axes with energy maxima along [110] and [111].

Thermal energy

The last energy contribution is simply the thermal energy, providing a contribution of $E_{\text{thermal}} = k_{\text{B}}T$, where k_{B} is the boltzmann constant. The thermal energy contribution is temperature dependent and can completely change the macroscopic behavior if the temperature is changed sufficiently, as discussed with regards to the Curie temperature in Section 2.1.2. In a regime where the thermal energy is of sufficient magnitude compared to the other contributions, it will provide a degree of random orientation in the magnetization.

Total energy

By summing all these contributions it is possible to quantify the total energy of the system. The total energy can be expressed as

$$E_{\text{tot}} = E_{\text{exch}} + E_{\text{demag}} + E_{\text{ext}} + E_{\text{anis}}. \tag{2.11}$$

By the second law of thermodynamics, any thermodynamical system can be said to follow the principle of minimum energy [44]. The internal energy of a system, such as the one defined by the micromagnetic model by Equation 2.11, will decrease towards a free energy minimum at equilibrium. In other words, the total state of our micromagnetic system is stable if the sum of the free energy contributions is at a minimum. However, it is worth noting that the minimum does not have to be a global minimum, known as a ground state. The system can also reside in local minima, known as stationary states or metastable states.

2.3 Supermagnetism

Supermagnetism in itself is not a well-established term but refers to a set of related physical concepts. It encompasses several novel magnetic phenomenon such as **superparamagnetism**, **superferromagnetism**, and **superantiferromagnetism** which will be discussed in the following section. Common to them all is the involvement of ensembles of individual magnetic particles. These particles are usually monodomain, and assembled in a superstructure with its own parameters such as pitch, stacking orientation and bounding area. Assembling simple constituents in a superstructure is similar to a metamaterial setup, and gives rise to metamaterial properties, where the mutual behavior is qualitatively different from the sum of its constituent parts.

To understand the ensemble properties arising once the magnetic particles are assembled in a superstructure, it is useful to discuss the individual magnetic particle behavior. As mentioned in Section 2.1.3, the formation of domains is a balance between the magnetostatic energy from a large, ordered region and the exchange energy from sustaining a domain wall. The former grows with the volume of a particle, and the latter contribution grows with the surface area of the domain walls. In a particle of radius r, the growth of energy contributions from the stray field and the domain walls can be expressed as an r^3-dependency and an r^2-dependency, respectively. For large particles, the volume dependent magnetostatic energy dominates and leads to the formation of domain walls which reduces the amount of parallel magnetized volume. However, for small particles the energy cost of domain wall formation can become larger than the magnetostatic energy cost of a single domain in the total volume. Thus, there will be some critical radius where the magnetostatic energy of a completely uniform magnetization is surpassed by a higher cost of exchange energy required to form a domain wall. In other words, there is a critical radius such that the particle will contain only a single domain, and this radius can be shown to be [4]

$$r_{\mathrm{c}} \approx 9\frac{(A_{\mathrm{exch}}K_{\mathrm{u}})^{1/2}}{\mu_0 M_{\mathrm{S}}^2}, \tag{2.12}$$

where K_{u} is the uniaxial anisotropy constant. However, it must be stressed that Equation 2.12 is only valid for a spherical particle with some uniaxial anisotropy, and the domain wall is a so-called Bloch wall, which is a bit different from the Néel wall illustrated in Figure 2.7. The model systems used in this thesis are comprised of flat, two-dimensional disks which are created of a material, permalloy, with negligible magnetocrystalline anisotropy. For the two-dimensional case with sufficiently flat disks, the magnetization is expected to lie mostly in-plane. In-plane magnetization only supports a Néel wall, as illustrated in Figure 2.7, and the expression for the permalloy thin film nanomagnets is different from the system described by Equation 2.12. Despite these differences, Equation 2.12, demonstrates the concept of a critical radius and its dependence on the exchange stiffness and saturation magnetization. With the requisite that small nanomagnets are monodomain, each particle in an ensemble of such monodomain magnetic particles may act as a single magnetic moment. The magnetic moment of a uniformly

magnetized, tiny magnet is often termed a macrospin or superspin, and can have magnitudes much larger than the magnetic moment of individual atoms ($10^6\mu_B \gg 1\mu_B$) [10].

Furhter in this section, an introduction to common supermagnetic effects will be handled, following the approach outlined by Bedanta and Kleemann [10].

2.3.1 Superparamagnetism

If the monodomain particles are sufficiently spaced out, the stray fields emanating from a single particle would be too weak at the neighboring particle for the particles to be dipolarly coupled. Instead, each monodomain magnet would act independently, and their spin would jump between random orientations due to thermal energy. The state of the ensemble is termed superparamagnetic (SPM) when the particles act independently, analogous to the atomic spins of paramagnetic materials. In fact, the analogy is very accurate with the difference being that the atomic or molecular magnetic moments are replaced by the macrospins of the magnetic particles.

At a temperature above the Curie temperature of the bulk material which the particles are fashioned of, T_C^b, all particles would act as paramagnetic particles and the ensemble would effectively be a normal paramagnetic material. However, at $T < T_C^b$, the particles would act ferromagnetically, and thus they have a large net moment, a macrospin. In other words, it is a necessary requirement that the particles themselves are in a bulk FM regime, in order for the ensemble to be in the SPM regime.

Depending on the anisotropic nature of the individual particles, SPM ensembles can be divided into either isotropic or anisotropic SPMs. If the particles have a significant degree of anisotropy, the magnetization of each particle will jump between the available easy axes. However, if the particles are completely isotropic, the magnetization may lie along any orientation. The last type of isotropic SPMs are the most relevant to this thesis, as the studied material system, permalloy (Py), film is an approximately isotropic magnetic material [45].

In isotropic SPM, the system can be treated in the exact same way as normal paramagnetic materials by the Langevin description [46]. Thus, under an externally applied field magnitude, H, the mean dipole moment, m, (in the applied field direction) can be expressed

$$\mu_0 m H = m\left(\coth(x) - \frac{1}{x}\right), \tag{2.13}$$

where $x = \mu_0 m H / k_B T$. Note that the dipole moment m is that of the single-domain nanomagnet macrospin, not the magnetic atom or unit cell (as it would be for regular paramagnetic materials). The similarities between paramagnetic and SPM materials leads to SPM behavior that is identical to paramagnetic behavior, but with extremely large moments, and thus large susceptibilities, which provides a new, novel material property.

2.3.2 Superferromagnetism

As the macrospins have magnetic moments which are three to five orders of magnitude the strength of atomic (or molecular) moments, the dipolar coupling can cause inter-particle interactions [10]. The dipolar, inter-particle interaction will be more relevant at decreasing temperatures as the thermal energy does not dominate, and can lead to interactions over significant distances even for systems which are not physically percolated. If the interaction is strong enough to catalyze long-range order in the particle ensemble, the system can be described as a superferromagnetic (SFM) system.

The predicted SFM state may occur for increased particle concentrations, where the inter-particle distance is sufficiently short that it allows magnetic inter-particle interactions. Depending on the exact geometry of the particle stacking, the interactions can align the macrospin moments so that they form FM-like regions. An illustrative example of SFM stacking can be found in Figure 2.10. The macrospin moments can be thought of as reinforcing each other's directions through magnetic interactions and may align collectively along the same direction. The free energy minimization of each particle will be dominated by the free energy minimization of the entire ensemble.

It can be hypothesized whether the stacking geometry will direct the collective behavior along certain lattice-defined easy axes, such as the most densely packed directions. For some systems the lattice-defined directions might overcome the magnetocrystalline anisotropy of the material itself, which has been shown by simulations in a recent paper but is otherwise not well-studied in literature [33, 47].

However, the long-range order introduced by the SFM behavior cannot extend through space indefinitely. Such long-range order would lead to an energy-costly stray magnetic field thus washing out the energy minimum allowing the collective SFM behavior. Instead, a large ensemble will create FM-like SFM domains, where each "super-domain" exhibits SFM behavior with a net magnetic moment in an individual orientation. Separate SFM domains allow for a net magnetization of zero, despite long-range order across particles in most of the sample, thus minimizing the demagnetizing field. This behavior reinforces the analogy of an SFM system to a regular FM system, as the FM domains are simply replaced by SFM domains. Figure 2.11 provides and analogue to the FM domains illustrated in Figure 2.3, for the SFM domain regime.

While there have been many theoretical studies of such SFM systems, experimental evidence has been elusive or limited to small subsets of a material in self-assembled systems [10].

2.3.3 Superantiferromagnetism

For some lattice structures, the macrospin nanomagnets might favor aligning their magnetization in a different scheme, where they are not all parallel. The macrospins may align anti-parallel due to a geometric stacking that favors antiparallel alignment. Thus, the system can behave superantiferromagnetically (SAFM). The SAFM phenomenon is

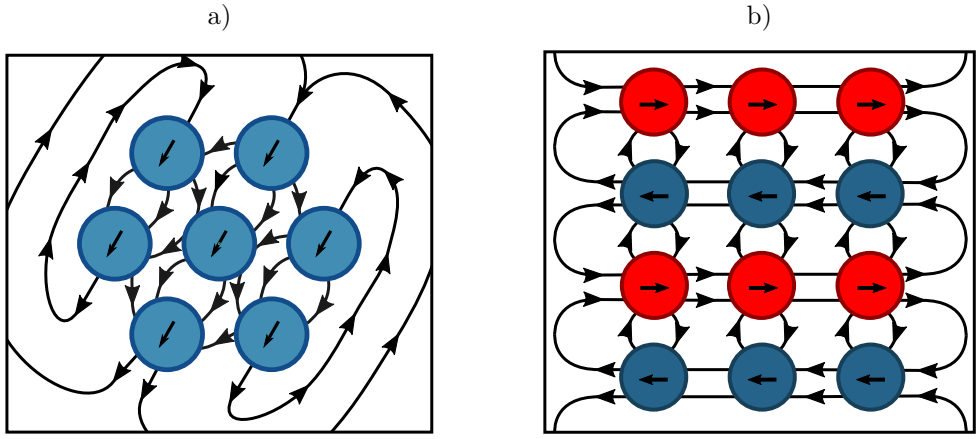

Figure 2.10: Supermagnetic behavior as a function of stacking geometry. a) SFM behavior of circular nanomagnets in a two-dimensional, trigonally stacked lattice. The black field lines, representing $\mathbf{H}_{\text{demag}}$, illustrates how this arrangement might facilitate parallel alignment, resulting in a significant net magnetization. b) SAFM behavior of magnetic nanodisks in a two-dimensional square stacked lattice. Here the field lines support antiparallel alignment. Note that the net (macroscopic) magnetization of such a long-range ordered structure would be zero.

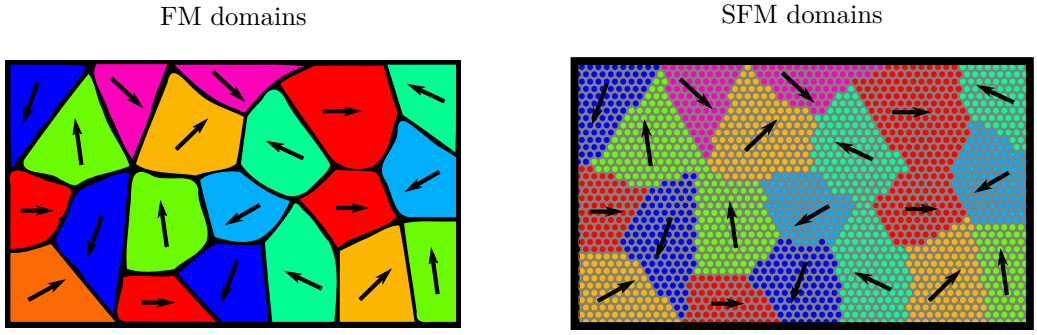

Figure 2.11: Illustration demonstrating the comparison of similar domains in ferromagnetic and superferromagnetic materials. Note that due to the monodomain nature of the nanomagnets in the SFM, the borders can only exhibit angles concurrent with the lattice, as each particle must have a well-defined orientation. This last fact is only a simplification, and real-life examples might have particles with more complex magnetic structure.

completely analogous to regular antiferromagnetic behavior, where the microspins (i.e., atomic magnetic moments) are aligned in an antiparallel fashion. The antiparallel arrangement would lead to a virtually non-existent magnetization due to the macrospins' moments canceling each other out, at least when the material is viewed on a macroscopic scale. If viewed with considerable resolution the material might have significant magnetization in local regions, the size of the magnets themselves. An illustrative example of how SAFM might manifest in a square lattice can be seen in Figure 2.10b. The SAFM state will not be further discussed here.

2.4 Magnetic force microscopy

Magnetic force microscopy (MFM), is an experimental technique that can be used to image the vertical stray magnetic field above a sample. It is an example of scanning probe microscopy (SPM), which offers sub-wavelength (of visible light) resolution which would not be possible with other optical techniques.

The technique is based on the interaction between a tip mounted on a microscopic cantilever. In MFM, the distinguishing feature separating it from other SPM techniques is the use of a magnetized tip. This magnetized tip is the basis for the interaction between the sample and the instrument. Its apex is sharply defined, from atomically sharp to rounded to a few nanometers, and this single point of interaction defines the limit of the achievable resolution.

As the tip will exhibit a small magnetic moment, it can interact with the demagnetizing field of the sample. A favorable magnetic interaction, i.e., a field aligned with the tip's magnetic moment, would attract the tip and a non-favorable interaction would repulse the tip. The magnetic interaction is the root of all contrast in MFM, and is exploited in a more sophisticated way as described in the following paragraphs. However, it is important to note that because the tip is aligned perpendicularly to the sample the MFM will only be able to observe the perpendicular component of the stray field. Despite this restriction, MFM can be enough to give a good indication about the micromagnetic structure of the sample.

The tip is mounted on a cantilever that facilitates deflection or even an oscillating motion of the tip. A laser beam that is reflected off the back side of the cantilever can be used to determine the amplitude of the deflection by self-interferometry, measuring the path difference (or the reflected angle can be detected by a sectioned photovoltaic cell). An illustration of a basic MFM setup can be found in Figure 2.12.

In MFM's most simple form, the cantilever could be static and sweeping across the sample at a constant height. While scanning, the cantilever deflection could be monitored by the laser beam and mapped to the point on the sample, in order to create a crude map of sample-tip interactions by deflection. However, this scanning scheme would introduce a lot of noise, and the deflection due to magnetic interaction would be hard to separate from background fluctuations.

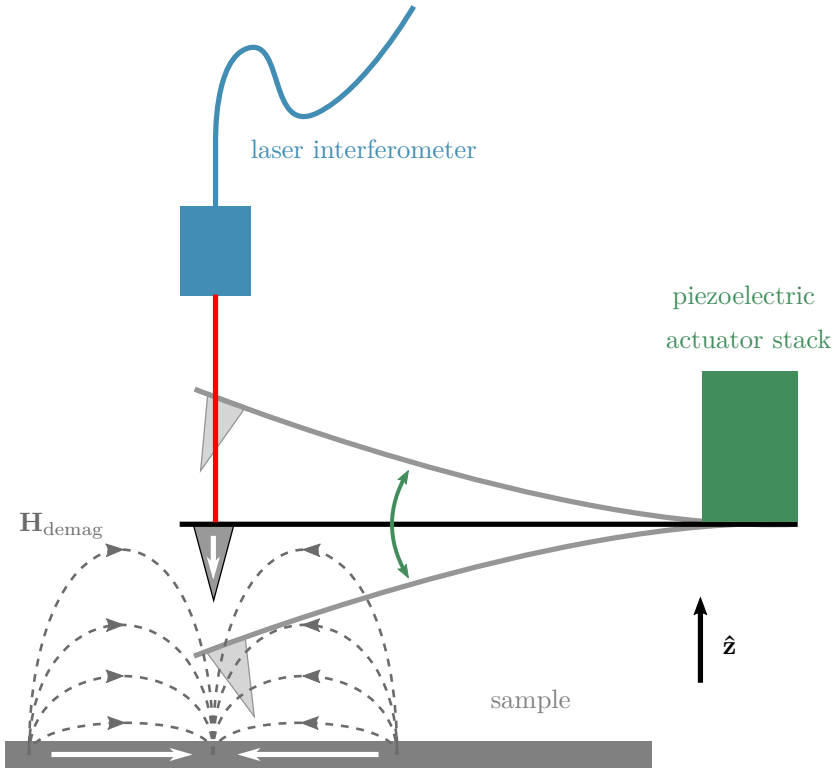

Figure 2.12: Simplified MFM schematic. The green piezoelectric actuator stack incurs an oscillating motion in the cantilever. The cantilever deflection is detected by the blue laser interferometer. The oscillation of the cantilever will be modulated by the gray field lines, $\mathbf{H}_{\text{demag}}$, which interacts with the magnetic moment of the tip. The white arrows indicate the magnetic moment of the tip, and the in-plane magnetic moments of the sample.

Instead, the cantilever is dynamically driven by a piezoelectric stack (which also facilitates the fine scanning motion) inducing an oscillating motion at a specific frequency. The cantilever is finely tuned so that it has a well-defined resonance frequency, f, and when driven at this resonance frequency the amplitude of the cantilever oscillation is maximized. If the cantilever with the magnetized tip was brought into contact with a magnetic stray field, the force due to the magnetic interaction would modulate the resonance frequency of the cantilever, as can be realized by considering the driven harmonic oscillator system. This resonance frequency change will result in a change in the amplitude, as it is now driven at a frequency slightly offset from resonance, $f_{\text{piezo}} = f + df$. The change in amplitude can be detected and recorded by the laser interferometer, and again mapped to create an image of the vertical stray field above the sample.

However, the approach of measuring the amplitude would require that the amplitude is damped sufficiently fast so that the recorded amplitude change is a function of the current probe position. If the amplitude change is too slow, the probe will have scanned further on, thus not mapping the correct amplitude changes to the correct positions. Amending this shortcoming can be done by performing an even more sophisticated MFM operation: The resonance frequency change will lead to an instant change in phase between the driving piezoelectric stack and the oscillation response of the cantilever. This phase change is very sensitive and easy to detect, making it the ideal physical measure of magnetic interaction contrast.

The MFM can thus be very sensitive to small changes in the magnetic stray field, but translating the contrast due to phase or amplitude changes into quantitative meaningful data is not straightforward. The technique is still an immensely useful qualitative technique, as the magnetic contrast alone is enough information to determine the micromagnetic state of the sample, which the MFM plainly provides. However, the technique has its shortcomings, and analyzing data captured through MFM is not a trivial task. The difficulty of translating MFM measurements to meaningful information on micromagnetic domains is obvious when considering that the MFM only measures the demagnetizing field at a single side of the sample, and only the vertical component of the field. While the needle can be assumed to have a magnetic moment that is completely aligned along its length, the absolute orientation (i.e., whether the moment is pointing up or down the tip) is usually unknown. This fact, that the absolute orientation of the needle is usually unknown, further complicates the analysis.

There is a vast amount of details left out of this discussion of the MFM and its modes of operations, but the discussion is kept brief and complimented by a thorough methods section on the MFM measurements carried out in this thesis, in Chapter 5.

2.5 Electron beam lithography

Electron beam lithography (EBL) is a flexible, state of the art fabrication technique used for micro- and nanofabrication. It is similar to the common photolithography used for

mass production in the electronics and semiconductor industry. Instead of light as the transfer medium, it utilizes an electron beam.

The sample to be patterned is coated with a thin film of electron-sensitive resist. A digitally controlled electron beam traces a pattern on the sample, delivering a well-defined dose of electrons to the predefined areas of the sample. The resist will change its chemical structure as a result of the electrons from the beam, making it more or less soluble. Thus, when a special developer chemical is applied, a thin film with the desired pattern will be left on the sample.

The advantage of using an electron beam instead of light is a much greater achievable resolution, as the electrons in the electron beam are accelerated to such high energies that their wavelength is less than the wavelength of light. As wave diffraction is the major resolution-limiting factor in light-based photolithography it is clear that the EBL has a much greater potential for high resolution patterning. In addition to the high resolution, the EBL pattern is defined according to a digital design file, as opposed to a physical, optical mask, which allows for great flexibility and quick prototyping without the need to reinvest in a costly mask.

One drawback to the serial nature of the electron beam is the speed at which it can develop patterns. As it has to travel across the sample and write the pattern, it is severely affected when writing a large and complex design. When using light on the other hand, the entire sample is patterned in a parallel fashion, leading to very fast production times. However, the flexibility and superior resolution of EBL makes it the ideal candidate as a scientific tool for researchers who do not need to mass produce samples.

As the resist in itself is only a generic polymer material, the EBL process is usually combined with other techniques, such as etching or metalization, in order to pattern the desired the material. One such technique is lift-off, in which a target material is coated on top of the sample after developing a patterned resist. The target material will adhere to the sample substrate in the regions where the resist has been removed, creating a negative pattern. Then, the resist is removed with a sufficiently strong solvent and the target material which was deposited on the resist is removed with it. Thus, a complex pattern may be applied by the lift-off process to any material which can be easily deposited and coated on a sample, e.g. by electron beam evaporation.

Chapter 3

Micromagnetic modeling

3.1 Introducing simulations

This thesis has involved simulations of micromagnetic systems by the use of MuMax3's GPU-accelerated, open-source simulation software. This software was developed by researchers at Ghent University and is well-documented in an article by Vansteenkiste et al. [48]. It solves the time- and space dependent magnetization evolution of micromagnetic systems involving nano- or micro scale magnetic components. This activity is often termed micromagnetic modeling.

Simulations like these are an extremely valuable tool that can complement experimental data, provide new insights and in a quick way establish a path forward. Although simulations can never replace real-life experimental data, they can provide a reasonable educated guess on the genuine behavior of physical systems. However, when simulating complex systems and unintuitive phenomena, careful consideration must be applied to the computational setup in order to provide results whose validity can be trusted. This section will present such considerations relevant to the thesis work.

In this thesis, micromagnetic modeling has been used as a way to probe the parameter space of desired phenomena, and to verify the analysis of other experimentally obtained data. The first application has proved extremely useful in order to prototype and develop refined samples of nanomagnet ensembles.

In this chapter the micromagnetic modeling will be discussed. First, the method applied in MuMax3 will be presented briefly. For further detail on the implementation and verification of MuMax3, the reader is referred to the original paper by Vansteenkiste et al. [48]. The second section of this chapter will present the setup of the micromagnetic modeling performed in the thesis, with justification for methodological assumptions.

3.2 Simulating micromagnetic systems

By applying the micromagnetic model outlined in Section 2.2, it is possible to map out the forces and interactions of a well-defined system. However, in order to calculate the time- and space dependent evolution of such a system, we must establish a new, time-dependent piece of the puzzle describing such systems. The time-dependent puzzle piece can be found by considering the Larmor-precession mentioned in Section 2.1.1, as will be presented in the following theoretical framework.

3.2.1 Theoretical framework

By introducing a dimensionless torque (the Landau-Lifshitz torque), denoted $\boldsymbol{\tau}$ (units s^{-1}), it is possible define the time evolution of magnetization as the differential equation

$$\frac{\partial \hat{\mathbf{m}}(\mathbf{r},t)}{\partial t} = \boldsymbol{\tau}, \tag{3.1}$$

where we again have utilized the micromagnetic simplification that the magnetization $\mathbf{M}$ can be expressed in terms of the reduced magnetization unit vector, $\hat{\mathbf{m}}$. Equation 3.1 can be seen as a result of Equation 2.1. This torque, expanding on the simplified representation in Equation 2.1, can be analytically expressed in terms of the Landau-Lifshitz-Gilbert equation [49–51],

$$\boldsymbol{\tau} = \gamma_{\mathrm{LL}} \frac{1}{1+\alpha^2} \Big(\hat{\mathbf{m}} \times \mathbf{H}_{\mathrm{eff}} + \alpha \big(\hat{\mathbf{m}} \times (\hat{\mathbf{m}} \times \mathbf{H}_{\mathrm{eff}}) \big) \Big), \tag{3.2}$$

where γ_{LL} is the Landau-Lifshitz gyromagnetic ratio ($\mathrm{rad}\,\mathrm{T}^{-1}\,\mathrm{s}^{-1}$), α is the dimensionless Landau-Lifshitz damping parameter and $\mathbf{H}_{\mathrm{eff}}$ is the effective magnetic field. The term effective field is here defined such that it includes all contributions detailed in Section 2.2, in addition to some more specific details left out for the sake of brevity (e.g. the Dzyaloshinskii-Moriya interaction).

The system described by Equations 3.1 and 3.2 can be solved analytically, but only for a few simple systems [52–55]. However, for the complex systems of interest the dynamic behavior must be solved numerically.

There are two major numerical approaches to solving solutions described by a (set of) differential equations; The finite-difference method and the finite-element method. In the finite-element method, the function's domain (usually real-space) is divided into small pieces with simple geometrical confines, such that the system can be described as a sparse matrix. The dynamic equations are approximated for each element and assembled to solve the state of the full system. The finite-difference approach on the other hand is a more direct representation of the partial differential equations where the functions' domain is divided into a regular grid of finite differences, transforming the continuous nature of the analytical equations into discrete differences. The dynamical equations can then be applied and solved through regular matrix solving techniques.

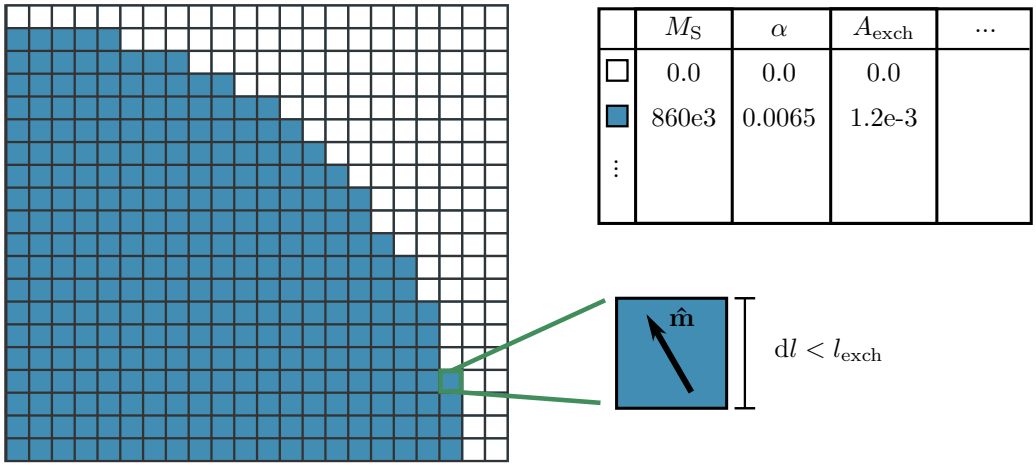

Figure 3.1: Representation of MuMax3's computational grid. The grid consists of discrete cells which are assigned material parameters, such as the white non-magnetic region and the blue Py-like region. The size of the cells are so that $dl < l_{exch}$ and the magnetization in each cell can be assumed uniform, here indicated as $\hat{\mathbf{m}}$. The cells will also have a finite depth, and layers of such grids can be used to model systems with three-dimensional geometry.

When approximating a continuous, dynamic system with a discrete one, a natural consideration is the resolution of the approximation. The resolution in this case can be thought of as the size of a grid point in the finite-difference matrix. If physically significant details are described at length scales smaller than that of the finite grid the numerical approach would not be a good representation. On the other hand, if the dominating dynamic mechanisms can be described well by a finite-difference grid of a certain resolution, there is nothing to gain, other than increased simulation costs, by reducing the grid size. In order for the approximation to be valid, a single discrete cell must be well-described by a uniform magnetization. For a micromagnetic system, this smallest element of uniform magnetization can be found by considering the exchange interaction and the exchange stiffness, A_{exch} as described in Section 2.2.1 and Figure 2.8.

The largest length at which the magnetization safely can be assumed uniform is termed the exchange length, l_{exch}. This length is defined as [48]

$$l_{exch} = \sqrt{\frac{2A_{exch}}{\mu_0 M_S^2}}. \tag{3.3}$$

If the discrete computation cell is less than l_{exch} the assumption of cell magnetization uniformity holds, and there is no need to increase the resolution further. Thus, the finite-difference micromagnetic grid can be well illustrated by the discrete grid in Figure 3.1.

3.2.2 MuMax3

The method utilized in this thesis is finite-difference discretization. The open-source software MuMax3 provides a GPU-accelerated, intuitive framework for performing flexible micromagnetic modeling experiments. It utilizes a mesh of orthorhombic cells to describe the micromagnetic system and can incorporate complex systems of multiple sets of distinct material parameters. By the use of powerful graphics cards, the GPU-accelerated approach can be significantly faster (two to three orders of magnitude) than a simple CPU-based approach. Fortunately, powerful graphics cards developed for high-end gaming systems are readily available and may provide a great computational setup for quickly exploring micromagnetic systems in a research setting.

MuMax3 provides a great method for defining the geometry of a system-of-interest by scripting simple shapes and geometries by the constructive solid geometry convention. It can also read bitmap files and translate any complex geometric description to a corresponding computational grid. Once the system's geometry, material composition, material parameters, initial magnetization and magnetic fields are described, the computational system is in its initial state and the resulting dynamics are ready to be explored by running the simulation.

There are mainly two interesting approaches to "running the simulation" that can reveal insights into the behavior of the system. It might be interesting to look at the direct time-evolution of a system from its initial state. Observing the time-evolution of a system can be done in MuMax3 simply by letting the time progress in finite steps and update the system matrix for each step according to Equation 3.1. However, this approach will only compute a specific path through the complex energy landscape describing the whole system, as it will follow the direction of steepest descent. Following the path of steepest descent might leave the system trapped in metastable state, a local energy minimum, and is not guaranteed to provide realistic or useful insights of the system's true nature, unless the experiment is particularly well-designed.

The other approach is to solve for the ground state, or the relaxed state, of the system. Fortunately, MuMax3 provides a great and simple method of numerically finding the ground state of the system through the use of its `relax()` function. Several numerical solvers, such as the Runge-Kutta methods, are implemented and may be chosen for any appropriate use-case. Utilizing numerical solvers specialized to find the global minimum of a complex function, a stable, low-energy state for an initially frustrated system setup may be found. The *true* ground state is not guaranteed to be found this way, although choosing an appropriate numerical algorithm will increase the likelihood of finding a true ground state.

The `relax()` can also be used to provide a time-evolution picture by changing a parameter in the system, such as the applied magnetic field, and let the numerical solver relax the system. As long as the parameter is changed gradually with relaxations between each step, this approach is a good approximation of corresponding real-life experiments. The approximation is good assuming the system relaxes to the stable state on a time-scale

faster than the time-scale of the changing input parameter.

As MuMax3 accounts for a complete micromagnetic picture, it can provide output states and parameters at any time during the simulations. Saving these states allows for a detailed picture of the interactions and magnetic energies in any complex micromagnetic system. The ability to obtain such a detailed picture makes the simulations an extremely valuable asset for exploring new phenomena in micromagnetic systems without the need for expensive experimental guessing.

In addition to the direct state output, MuMax3 provides an output mode where it generates the expected observed image through the use of an MFM. As MFM has been the chief experimental, investigative technique in this thesis, this output mode has proven invaluable to the verification and analysis of experimental results.

More details on the specific implementation of the `relax()` function and MuMax3 in general can be found in the article by Vansteenkiste et al. [48].

3.3 Modelling supermagnetism in patterned nanomagnetic arrays

In this section the specifics and practicalities of the simulations performed in this thesis will be detailed. The simulations were performed in order to investigate patterned nanomagnetic arrays and their supermagnetic behavior. The goal of the performed micromagnetic modeling has been two-fold: Firstly, to provide an indication of the expected behavior of the designed systems over a large span of parameter space and how this behavior would be manifested in experimental observation. Secondly, to provide complimentary insights into the micromagnetic dynamics observed in the obtained, physical experimental results.

3.3.1 Computational setup

The typical approach to simulations can be summarized as a few simple steps. First, to provide a well-defined starting point, the geometry was defined according to a set of specific parameters or as a subset of a greater parameter space. Then, the material parameters were defined, the specifics of which are described in Section 3.3.2. Finally, the initial setup was completed by defining an initial magnetization and externally applied magnetic field.

After the setup, the system would be relaxed to a low-energy state by MuMax3's `relax()` function. Then, optionally, a parameter such as the applied field was changed and the system was again relaxed. This process was repeated until the desired experiment reached its endpoint, either by completing the predefined parameter space or by the system reaching some predefined end state.

3.3.2 Magnetic material

The target material for this thesis is permalloy, a magnetic alloy of 80%-20% nickel-iron, often abbreviated Py. It has a high permeability and is easily deposited onto a sample as a thin film, making it ideal for this study where ease of fabrication is an important material aspect. Permalloy thin films as fabricated in this study are polycrystalline and is considered to be an isotropic magnetic material, i.e., it does not exhibit magnetocrystalline anisotropy [45, 56].

Based on previous experimental work the following material parameters were used to best describe the Py thin films at cryogenic temperatures (in this case around 5 K), as Py was the target temperature for experimental observation. The magnetic saturation, M_S for Py was set to $860 \times 10^3\,\mathrm{A\,m^{-1}}$, the exchange stiffness A_{exch} to $1.2 \times 10^{-3}\,\mathrm{J\,m^{-1}}$ and the Landau-Lifshitz damping parameter, $\alpha = 0.0065$. All anisotropy constants were set to the default values, resulting in a completely isotropic material (assuming negligible magnetocrystalline anisotropy). These values are simple approximations and proper justification for them should be established, which can be done through a method that will be outlined in Section 8.1.

Given these material parameters, the exchange length, l_{exch}, for Py can be calculated by Equation 3.3 and found to be approximately 5.1 nm. Thus, the computational grid can have a maximum cell size of 5.1 nm, but oftentimes the computational cell was significantly smaller than this maximum value. The reason for not choosing an increasingly smaller value is due to the way MuMax3 is implemented, where it is computationally advantageous to have a number of cells that is equal to a power of two. This computation advantage leads to the unintuitive result that a higher resolution simulation might compute faster than a lower resolution simulation.

Permalloy was used as the magnetic material of which the nanomagnets were comprised. The matrix material in which the magnets were "embedded" was free space, in the sense that the magnets were fashioned to be free standing, two-dimensional nanomagnet lattices on a substrate.

3.3.3 Geometric description

Throughout this thesis, a great number of geometric setups and different geometric parameters were explored. All geometries can be described as a two-dimensional planar design, patterned in a thin film of permalloy. For simulation purposes, the thin film was set to 15 nm in thickness. Assuming no out-of-plane magnetization, this film thickness was achieved by defining the computational mesh size in the z-direction to be 15 nm, thus also eliminating the need for extra (and computationally costly) two-dimensional layers. Deviations from this thin film thickness in the experimental results can simply be compensated by increasing M_S and thus the effective magnetic moment of each particle.

Some simulations of continuous thin films were performed for calibration and verification purposes, but will not be detailed here.

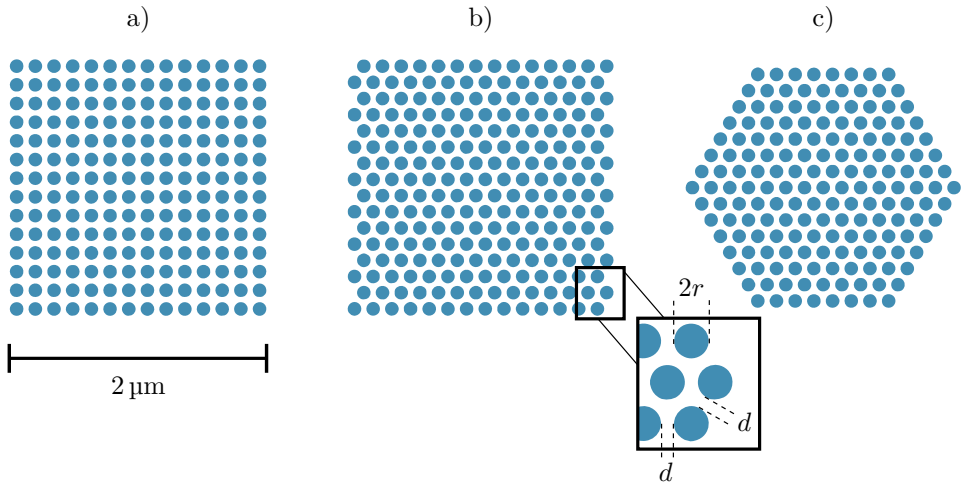

Figure 3.2: Geometric layout of nanodisk ensembles. All disks have a diameter of $2r = 100\,\text{nm}$ and a spacing $d = 40\,\text{nm}$. a) A $2\,\mu\text{m} \times 2\,\mu\text{m}$ square lattice. b) A trigonal lattice with a square bound of the same size. c) A trigonal lattice that is bound by a hexagonal shape. Note the jagged, vertical edges in b) compared to c). Geometries with a bounding area of size $5\,\mu\text{m} \times 5\,\mu\text{m}$ were also used, but are not shown.

The nanomagnets' geometry was defined as a flat cylinder spanning the entire z-space of the computation (i.e., 15 nm), and a large set of different radii were tested, spanning from 50 nm to 250 nm.

The way the disks were assembled is referred to as the stacking, and was either done in a trigonal lattice or a square lattice. The square lattice is simply described by two basis vectors of length equal to the stacking pitch and directed orthogonally to each other. The trigonally stacked latices have basis vectors with an angle of $\theta = 60°$ between them. The pitch of the stacking was defined by the sum of the diameter and the inter-particle spacing. This spacing was varied over a range from 30 nm to 100 nm, representing cases from high inter-particle interactions to low inter-particle interactions.

An additional aspect of the geometric description is the size and the bounding shape of the nanoparticle ensemble itself. Previous simulations have assumed a large, periodic lattice, where boundary effects of the ensemble termination will be neglected [47]. However, this thesis will limit the ensemble sizes in order to accurately describe the experimental counterpart, which are ensembles that *are* finitely bounded. There are two major size scales used, one that has a bounding box with sides of length 2 µm, referred to as a small structure, and one which has a bounding box with sides of length 5 µm referred to as a large structure.

For a squarely stacked lattice, a natural bounding shape is a square. However, the trigonally stacked lattice is more complicated when bounded by a square shape, as bounding a trigonal lattice with a square shape would lead to either halved nanomagnets or a bounding side which has a jagged formation. In order to limit the effect, and also inves-

tigate the qualitative difference, of a finite bounding of the trigonal lattice, two bounding shapes were used: the square (with two jagged bounding sides) and the hexagon. The hexagon was chosen as it results in densely packed borders, similar to the borders in a square bounded area of a square stacked lattice.

Examples of the described geometry, as initialized in MuMax3, is provided in Figure 3.2.

In addition to the stacking geometries described above, the basic geometry of the nanoparticle magnets can be changed. For instance the particles could be made slightly ellipsoidal in order to provide a uniaxial easy axis due to the shape anisotropy. While the simulations were performed over a large parameter space and many different geometries, the main focus of this thesis will be the square and hexagonally bound, trigonally stacked lattices of circular disks.

3.3.4 Magnetization model

In order to have a completely defined initial state, the remaining magnetization configuration must be described, as there is no natural undefined value. MuMax3 will initialize a default state as randomly magnetized, meaning that each cell in the computational grid is assigned a random direction. While a random state might be a good starting point in that it does not introduce anisotropy, it is not a physically typical starting state. Physical systems will tend to have a degree of anisotropy which might reinforce a uniform, rather than random, initial state.

For most simulations, the starting state was thus not the random magnetization state but a uniform magnetization in a specified direction. This choice of a uniformly magnetized start state was made in order to best match the experimental situation where a strong, applied magnetic field can ensure that the state of the physical sample is uniformly magnetized along the applied field direction. As a 5 T field can be applied with the available equipment, this assumption of uniformity can easily be fulfilled with the available methods

In MuMax3, the magnetization direction is conveyed through the use of an angle-dependent color map, and reading MuMax3's output requires some familiarization. In Figure 3.3 three different structures have been initialized with three different magnetization directions. These three directions, 0°, 45°, and 90°, have been the main initializing magnetization directions throughout the simulation work of this thesis. Figure 3.3 also displays the three main types of geometries most heavily investigated, which will be discussed in-depth throughout the thesis.

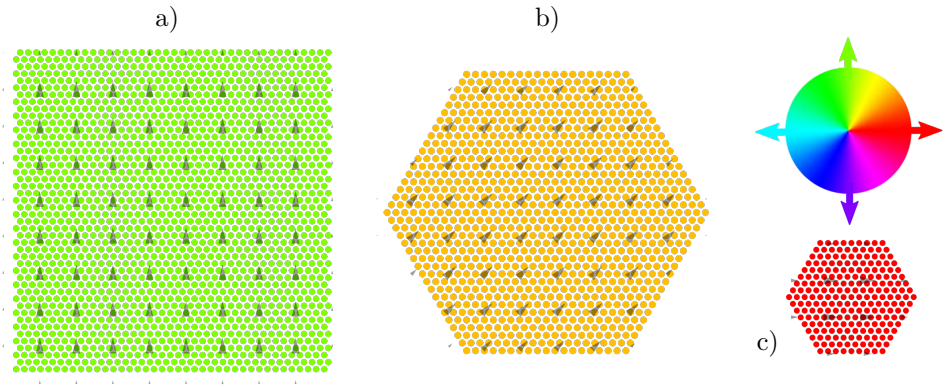

Figure 3.3: Three defined simulation geometries in their initial state, with different prescribed start magnetizations. a) A 5 µm × 5 µm trigonal lattice that is square bounded, with a uniform vertical magnetization. b) A 5 µm wide, hexagonally bound, trigonal lattice, with a 45° uniform magnetization. c) A 2 µm wide, hexagonally bound, trigonal lattice, with a horizontal uniform magnetization. The colorchart provided is MuMax3's colormap, relating the in-plane angle of magnetization to the displayed color. Also provided are small grey arrows indicating the magnetization of the structures, although this extra visual aid will not be utilized beyond this figure.

Chapter 4

Sample fabrictaion

In addition to investigation of ensembles of ordered, thin film nanomagnets through the use of simulation, physical samples were made using microfabrication techniques. This chapter will describe a design process developed for creating complex samples with large parameter spaces, followed by a brief presentation of the fabrication process.

4.1 Flexible mask design process

Considering all the variables of the geometric design described in Section 3.3.3, it is clear that the variation in sample design is vast and possibly time-consuming to implement. The traditional way to develop the digitally defined designs for EBL masks is to use a specialized EBL mask design software editor. Such an editor can help the design process by repeating structures, and even simple parameterization of the design can be implemented. However, given the desire to vary disk radius, disk spacing, disk elongation, lattice directions, lattice bounding shape, and lattice field sizes, the design job is simply not feasible with the available software.

To cope with the large parameter space, an extremely flexible, and time-saving, design method using an open-source Python package, gdsCAD, has been developed for this thesis. The method allows for the use of the intuitive Python language to construct complex geometric designs from simple shapes through the use of common programming methods (e.g. looping over a large parameter- or configuration space). For the purpose of this thesis and related work, several general purpose utility functions and specialized stacking functions were implemented. The process, with some of the implemented functions, is detailed in Appendix A.

4.2 Fabrication process

The sample designs were fabricated by co-supervisor, and PhD candidate, Einar Standal Digernes at the NTNU NanoLab clean-room facilities.

4.2.1 Electron beam lithography

Electron beam lithography (EBL) was performed using the he Elionix ELS-G100, a state-of-the-art, 100 kV EBL system with a 100 MHz pattern generator.

First, a silicon wafer is prepared for EBL by cleaning with acetone, followed by isopropyl alcohol and blowing dry with clean compressed nitrogen gas. The sample was then dehydration baked for 5 minutes on a 150 °C hotplate.

A uniform thin film of electron sensitive resist, CSAR62 (AR-P 6200), was made by a standard spin coating process onto the silicon wafer. The coating parameters were chosen to achieve a 100 nm thick film. The sample was soft baked for 3 minutes on a 150 °C hotplate.

Following the coating, the digitally designed pattern was transferred by selective exposure to the electron beam. A base dose of 100 $\mu C\,cm^{-2}$ was utilized with a beam current of 500 pA.

The exposed resist was then removed in CSAR62 developer solution (AR 600-546) by submersion for 60 s. The submersion was followed by a bath in isopropyl alcohol for an additional 60 s and blown dry with compressed nitrogen gas.

The end result of the EBL process was a silicon wafer covered with a thin, approximately 100 nm, layer of resist with a pattern that is the inverse of the digitally defined mask.

4.2.2 Permalloy deposition and lift-off

Permalloy deposition was carried out by electron beam-evaporation. A thin film of permalloy, approximately 15 nm thick, is deposited by electron beam evaporation while rotating the sample. Additionally, a thin layer of 2 nm aluminum was deposited as an oxidation barrier.

After deposition, the resist and the thin film on top of the resist was removed in an ultrasonic bath of the CSAR62 stripper (AR 600-71). The sample was left in the bath for approximately 5 min, followed by a rinse with isopropyl alcohol and blown dry with nitrogen gas.

The final part of fabrication was to inspect the quality of fabrication with a scanning electron microscope (SEM).

The fabrication process steps are summarized in Figure 4.1.

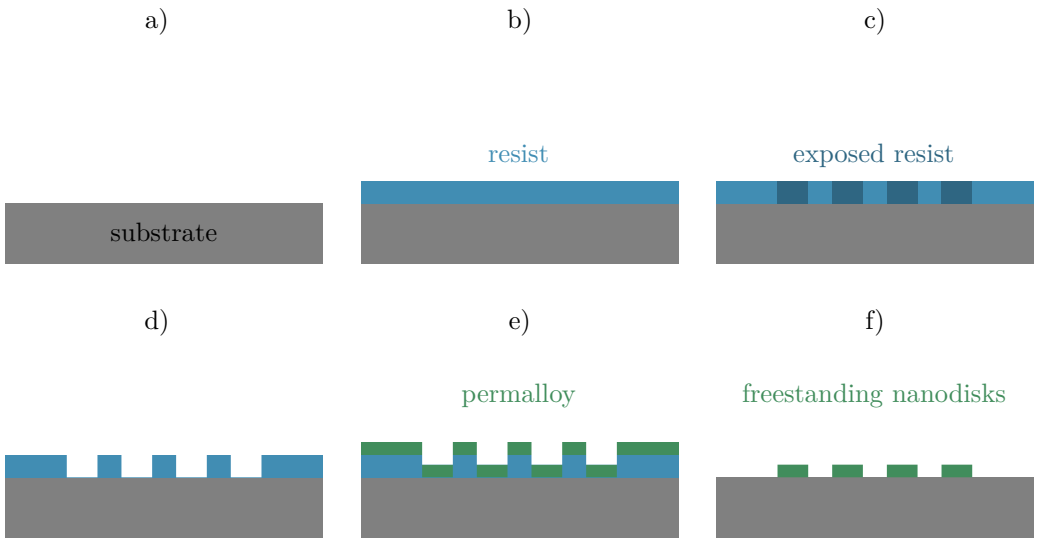

Figure 4.1: EBL and lift-off fabrication process steps. a) The substrate, a simple silicon wafer, is prepared for EBL processing. b) The substrate is coated with a thin film of an electron sensitive resist. c) The resist is patterned by EBL, using the digitally designed mask. Dark regions indicate the areas that have been exposed to the electron beam. d) The sample is submerged in a developer solution which dissolves the exposed regions, leaving a pattern of only unexposed resist. e) A thin film of Py is deposited by E-beam evaporation. f) Lift-off procedure. The sample is submerged in a strong solvent and the remaining resist is removed, simultaneously removing the permalloy deposited on top of the resist. The sample is left with free-standing nanodisks of Py.

Chapter 5

Magnetic force microscopy

This chapter will cover the experimental use of magnetic force microscopy to image the fabricated structures of magnetic nanodisks and detail how experiments involving applied fields were performed. The first section will cover the experimental setup, including information on the instrument and its auxiliary equipment. Following this, an overview of the most relevant experimental processes and the collection of data will be described in detail.

5.1 Magnetic force microscopy setup

5.1.1 Technical specifications

The MFM system used in this project was the AttoAFM/MFM I, manufactured by Attocube systems. It is operated with a MFMR-10 magnetic tip provided by Attocube with a thickness of approximately 3.5 µm and a cantilever width of approximately 30 µm. The tip parameters are provided in Table 5.1. It is coupled with an AttoDRY1000 XL cryostat, which provides cryogenic cooling to below 4 K, with a 5 T split coil electromagnet providing the possibility to interact with a sample through the application of strong magnetic fields.

The cantilever detection module is based on interferometric measurements using a laser with a wavelength of 1310 nm, directed to the cantilever head by a fiber optic cable from the control unit. The remote placement of the control unit allows the laser operation to be unaffected by the cryogenic temperatures. Additionally all the electronics driving the piezoelectric actuators and scanners are also placed in a separate control unit, providing

T [µm]	W [µm]	L [µm]	C [N m^{-1}]	f [kHz]
3.50 ± 0.10	30 ± 1	229 ± 0.5	4.7 ± 0.4	90 ± 5

Table 5.1: Specifications of the utilized MFM tips. The listed parameters are thickness, T, the width, W, the length, L, the spring constant, C, and the resonance frequency, f.

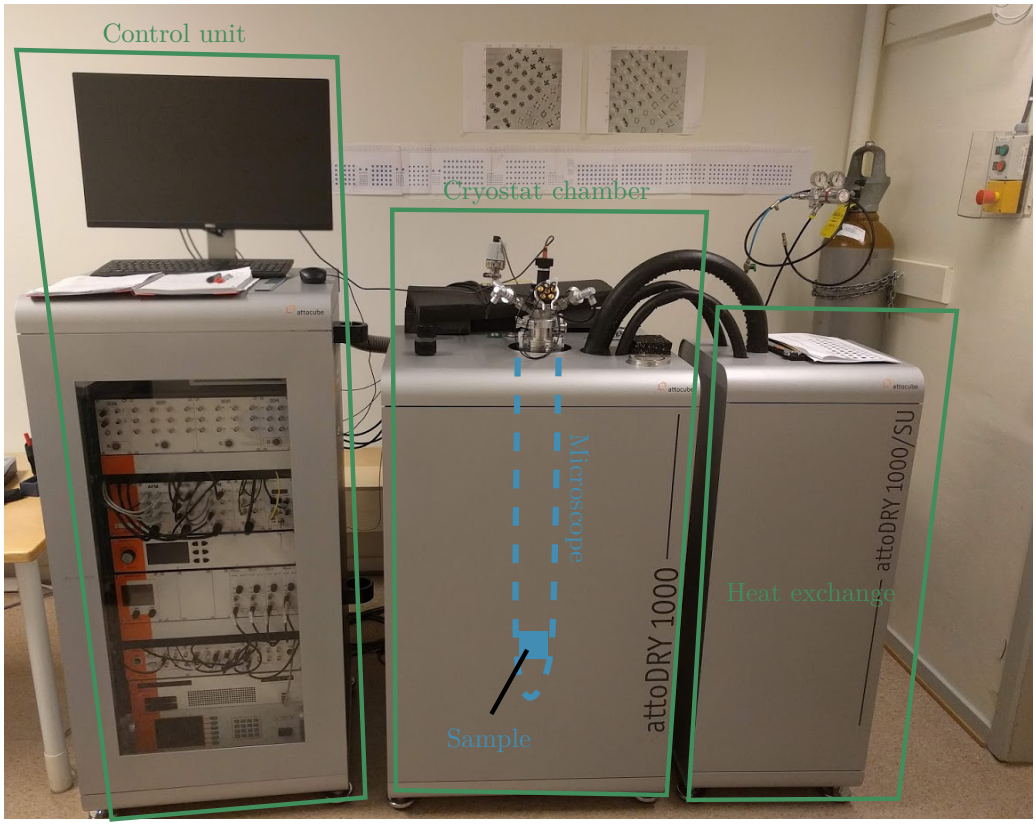

Figure 5.1: Photograph of the MFM equipment used in this thesis. All components are controlled via the electronic rack and computer in the control unit. The sample is placed in the microscope which is shaped as a long stick. In the photograph the microscope is loaded into the cryogenic chamber. The chamber is cooled by the cryostat, which is indicated on the right. Note that the visible part of the cryostat is in reality only the heat exchanger, as the main part of the cryostat and pump is located off camera.

reliable operation at extremely low temperatures.

The MFM equipment used in this thesis can be seen in the photograph in Figure 5.1. The proximity and the rigid connection of the cryostat unit, which is continuously pumping liquid helium into the microscope chamber, is a source of much vibration and noise. The noise from the cryostat is manifested in the measurements as a periodic disturbance matching the frequency of the pump.

5.1.2 MFM startup routine

As the system has been nonoperational for an extended period of time, and serving no other users, quite some time was spent optimizing imaging parameters. This section will go through the steps of setting up the microscope, while providing details for optimal operation and the parameters used while observing the micromagnetic samples.

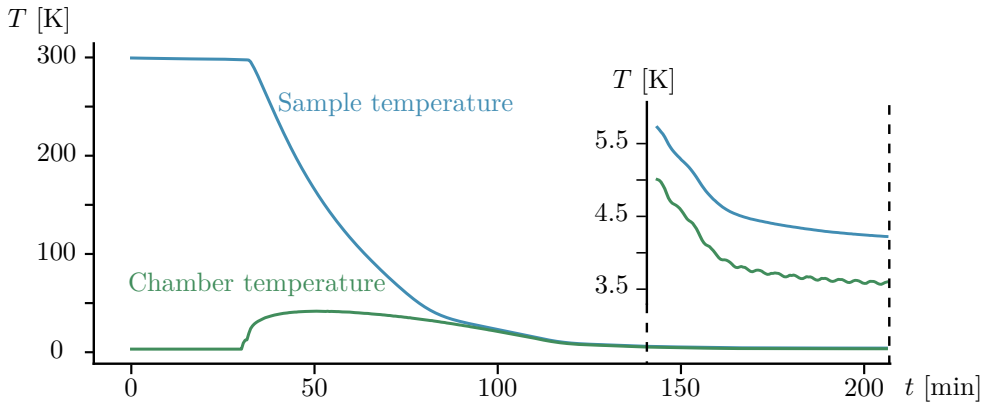

Figure 5.2: Temperatures of chamber and sample following insertion of the room temperature microscope with the sample. The insertion process happens at around $t = 30\,\text{min}$. From the enlarged inset it is clear that the temperature has reached equilibrium at around around $t = 200\,\text{min}$. Note that at these temperatures, a change of just 1 K is a substantial relative increase of the total thermal energy.

The sample was mounted on the stage by applying a conservative amount of high vacuum grease between the sample and holder. Additionally, a small drop of conductive, silver-based adhesive was applied to a corner of the sample in order to establish electrical contact between sample and grounding plate. Once the sample and tip was mounted, the microscope (with sample) was loaded into the cryostatic chamber, pumped to a vacuum of at least $1.0 \times 10^{-4}\,\text{mbar}$ before 20 mbar of helium gas was introduced to the chamber. The microscope was then left to cool to cryogenic temperatures. The measured sample temperature decreased to below 5 K in about 2.5 h, although the microscope was normally not utilized until more than 24 h after insertion to avoid excessive thermal drift due to non-equilibrium temperature gradients. A typical cool down of the sample after insertion into a pre-cooled chamber is provided in Figure 5.2.

Once the microscope was cooled and all optical and electronic systems were powered up, a quick calibration process was performed. The following calibration process was always carried out after system shut downs. First, a component named the dither, which fine-tunes the distance between the laser from the optical fiber and the cantilever head, was adjusted so that the interferometric detection was the most sensitive. The dither adjustment was done by scanning a small range of distances, corresponding to a few wavelengths, while recording the self-interfering amplitude. The dither bias was then set to correspond to the steepest point in the recorded bias-amplitude plot. An example of such a dither spectroscopy is provided in Figure 5.3. This figure seems to present a perfect sinusoidal graph, which is a testament to the equipment's low noise level and the dither's precision. The instrument is perfectly able to resolve the self-interference of a 1310 nm light wave.

Subsequently, the cantilever was excited to oscillation by a small excitation voltage of about 10 mV (for low-temperature (LT) measurements). To find the cantilever-tip

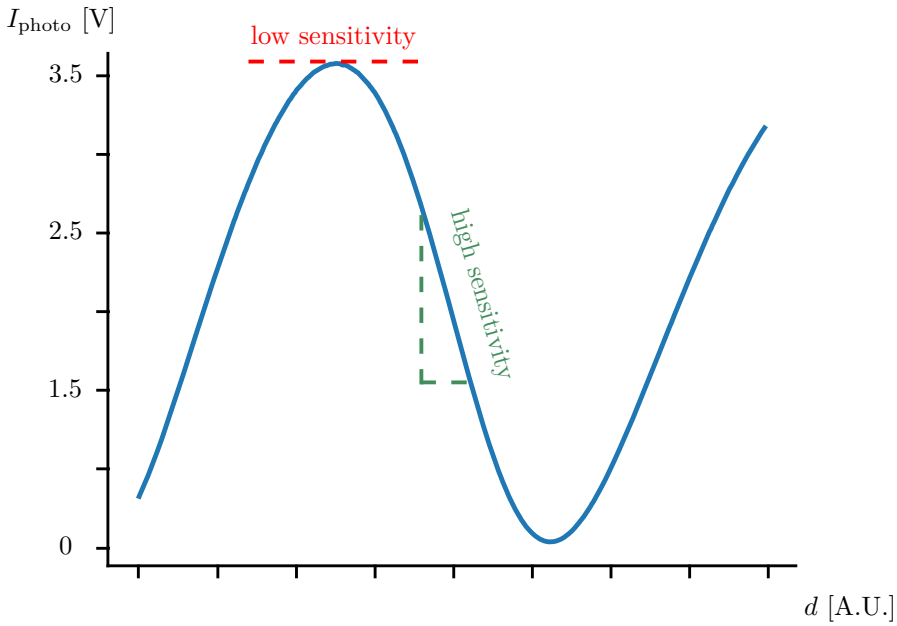

Figure 5.3: Dither spectroscopy from the MFM. The intensity measured by the photovoltaic cell I_{photo} is used to find the dither bias, d, of maximum slope. Utilizing a point of maximum slope ensures a highly sensitive working point. Indicated in green and red are the slopes of a good working point and a poor working point, respectively.

resonance frequency, a window of frequencies from 70 kHz to 90 kHz was scanned and the peak precisely identified by iterating the scans over narrower frequency ranges. The excitation amplitude was then adjusted so that the freely oscillating cantilever produced an interferometric amplitude of 1.0 V. The values of these parameters are based on experience and instructions from the manufacturer, but small deviations have shown to have little to no impact on the image quality or resolution (to within a reasonable range, of course). A crucial detail, however, is the calibration of the zero-point of the phase once the cantilever is oscillating. The quantity termed *the phase* is the relative phase difference between the recorded interferometric amplitude and the actuators' driving force producing the oscillating motion. Once the cantilever is freely oscillating at the resonance frequency, this phase is set to zero. Using this mode as the zero-point implies that any deviation from the zero-phase is a deviation from the freely oscillating cantilever driven at resonance frequency. An obtained resonance curve is provided in Figure 5.4.

The next step is to approach the sample, i.e., bringing the tip into contact with the sample. A tip oscillating close to a sample is expected to experience a damped amplitude. To avoid breaking the tip by crashing into the sample (while approaching), a soft threshold of about 80% of the freely swinging amplitude is specified as the threshold of contact. An autoapproach procedure is performed where the microscope slowly scans the tip closer to the sample, and if the amplitude is above the threshold of contact, the coarse steppers are used to jump across the scanned (and safe) z-region. Once the tip has coarsely stepped

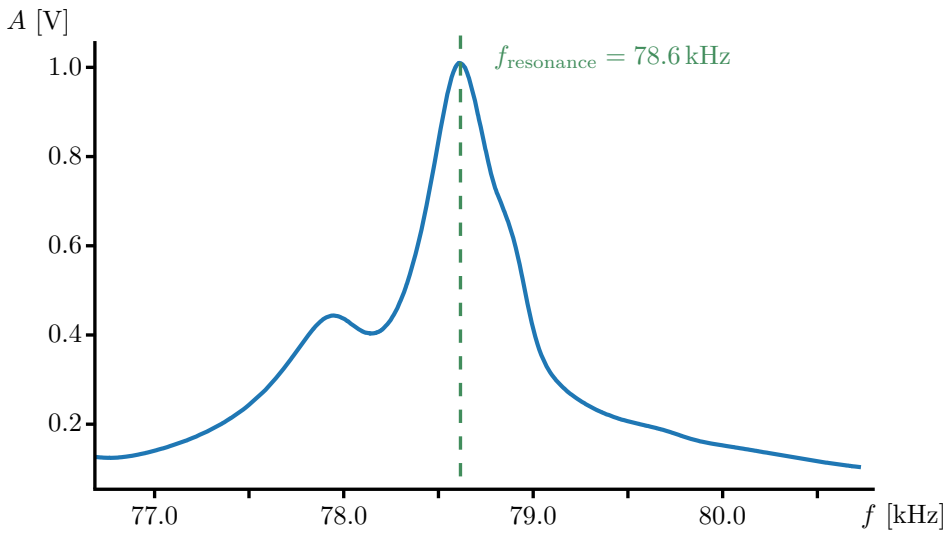

Figure 5.4: Resonance curve for a freely oscillating cantilever, where A is the detected amplitude. Indicated in green is the resonance frequency at $f_{\text{resonance}} = 78.6\,\text{kHz}$, the peak frequency. Note the small peak to the left of the main peak. This extra peak indicates a minor resonance frequency, which might be due to a defect in the cantilever or tip which perturbs the free motion of the main oscillating mode. The tip used to obtain this graph is therefore sub-par and should be changed.

into a scan range where the threshold of contact is reached, the autoapproach procedure is concluded. What follows is a slow approach in order to observe a sharp break-off point in the amplitude, due to the tip experiencing physical contact (manifested as abrupt van der Waals forces). The value of the break-off point is recorded, and the amplitude level corresponding to soft-tapping (i.e., the cantilever tapping the surface when extended close to the amplitude) is defined as 80% of this value. A feedback loop, outputting the z-position based on an amplitude input is used to stabilize the tip in the soft-tapping height.

5.1.3 Scan setup

For atomic force microscopy (AFM) scans (i.e., height profile scans), the feedback loop would be left on. Leaving the feedback loop on is done in order for the tip to be scanned across a region of the sample and simultaneously recording the required z-output to maintain the soft-tapping position. For AFM scans, scan speeds of about $1\,\mu\text{m}\,\text{s}^{-1}$ to $2\,\mu\text{m}\,\text{s}^{-1}$ were used, coupled with a feedback loop update rate at about 1 Hz to 5 Hz. The values were optimized for each scan in order to balance resolution and image quality with acquisition time.

However, for MFM imaging, where the interesting quantity is the vertical component of the stray magnetic field, the tip must be lifted from contact. Lifting the tip is done in order to eliminate atomic forces and pick up solely magnetic interaction between the tip

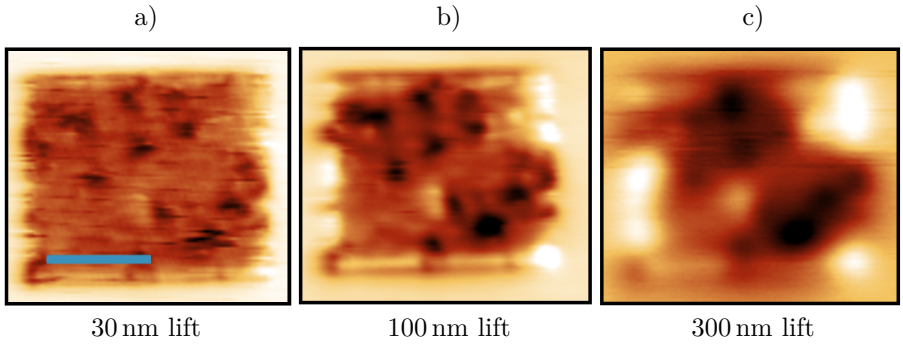

Figure 5.5: MFM images demonstrating the effect of lift height. a) An MFM image of a trigonal lattice of 100 nm disks and 30 nm spacing, taken at a lift height of 30 nm. The blue scale bar is 3 µm long. b) The same structure, obtained with a lift height of 100 nm. c) The same structure, obtained with a lift height of 300 nm. The color values are scaled for maximum perceptual contrast.

and sample. The distance the tip is lifted from the soft-tapping position prior to acquiring and MFM scan is termed the lift height. The lift height was quickly identified as one of the major factors in image quality and image fidelity.

Lifting too much leaves too little magnetic contrast, and results in an image that does not represent the magnetic microstructure of the sample, as the field contributions from different regions are overlapping (and weak). On the other hand, if the lift height was not high enough, the resulting image would not result in a realistic representation of the structure. In fact, it would lead to images showing a sample exhibiting mostly out-of pane magnetization, and only in one direction. The effect of lift-height is illustrated in Figure 5.5.

In Figure 5.5, it is clear the white contrast is not visible until the lift height is at least 100 nm. The appearance of contrast at increasing height can be a sign of some disturbance by the tip, or at least a low-fidelity image, at lower lift heights. The effect can be hypothesized to be a result of interfering magnetic interaction from the magnetic tip affecting the sample, and in that way either aligning the sample's magnetic moment out-of plane or inducing a vortex state while scanning. Regardless of the specific dynamics, it is clear that the tip is affecting the sample, and this disruption might change the magnetization of the sample, which should be taken into account when analyzing the acquired images.

The lift height was continuously adjusted by going into soft-tapping mode and re-lifting in order to optimize the quality of the resulting image.

Once lifted, an MFM image was acquired by scanning the tip over a predefined region. For MFM scans, the data acquired per point was the phase change, as discussed in Section 5.1.2. The number of lines (i.e., number of datapoints) and the scan speed was optimized to balance the acquired resolution with a feasible acquisition time. Typical MFM scan speeds were varied from $5\,\mu m\,s^{-1}$ to $60\,\mu m\,s^{-1}$. The effect of scanning at a

faster pace resulted in high contrast data points being smeared in the scanning direction.

This concludes the scan setup description. In the next section, the operation of the system, as used to obtain the results, will be covered.

5.2 MFM operation

Throughout the operation of the MFM, recalibration of system properties was performed continuously to ensure the best image quality. The imaging process consisted of moving the scan head to the desired region of the sample, going into soft-tapping contact, lifting and then scanning with specified parameters. Following is a few other considerations that affected the MFM data acquisition.

Drift in the system due to temperature gradients could severely affect the image quality. The cryostat's cooling power is not adjustable, so in order to ensure an extremely stable temperature and avoid non-equilibrium temperature gradients, a small heating element controlled by a PID feedback loop was used to hold the temperature stable at $(5.000 \pm 0.002)\,\mathrm{K}$. At these extremely low temperatures, a seemingly minuscule change in the absolute temperature is a great relative increase in the available thermal energy.

Another crucial parameter is the effect of the tip condition. The tip is theoretically expected to behave as a small, non-disturbing, magnetic test-dipole, analogous to the small test-charge used to construct electric field lines in electromagnetic theory. However, the tip must have a finite size. To compensate for the necessary finite size, the apex of the tip is fabricated to be as sharp as possible, so that it effectively behaves as a single magnetic dipole. If the tip is damaged or defectively fabricated, it might have a jagged apex or even multiple apices. Multiple apices would result in double pick-up, as each apex would provide magnetic contrast corresponding to the point on the sample directly beneath it. Other errors in the tip, such as demagnetization of the magnetic cobalt coating would also be deprecating to the MFM acquisition process. An example of the importance of the tip condition is provided in Figure 5.6.

5.2.1 Applying an external magnetic field

The experimental work consisted of more than purely imaging the ensemble structures. In addition to MFM imaging, the samples were subjected to various applied magnetic fields. A magnetic field was applied in order to probe hysteresis behavior and to investigate the collective behavior of the ensembles under magnetic influence. To apply magnetic fields the 5 T split coil electromagnet was utilized, although never operated anywhere near full capacity.

The electromagnet allows magnetization along a static axis, although the sample could be crudely rotated in-plane in order to achieve other magnetization directions. Fields were directed along the static axis in both directions, and is thus similar to the process found in hysteresis experiments. While changing the applied field, the tip was brought into soft-tapping mode with the feedback loop enabled, in order to avoid crashing caused

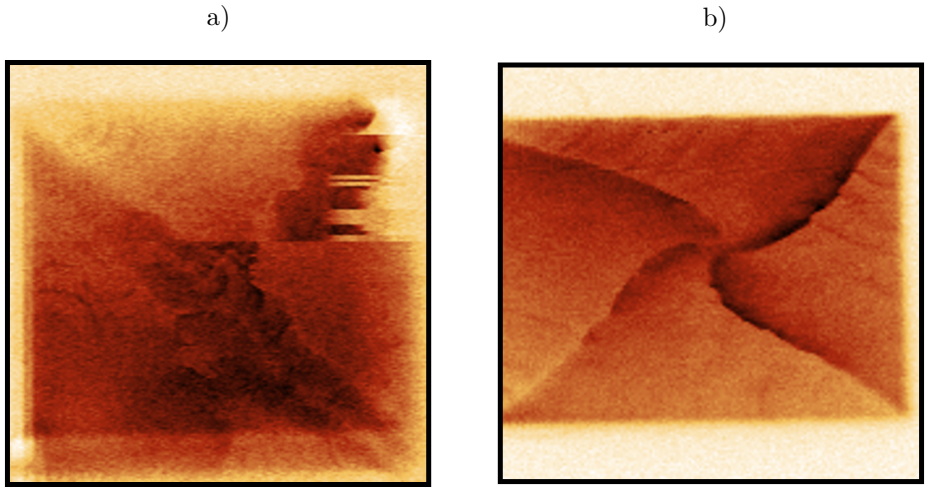

Figure 5.6: MFM images demonstrating the difference between sub-optimal and optimal tip condition. a) An MFM image obtained with a tip that is suspected to have blunt or jagged apex. Some features seems to appear doubled and overlapping. b) A nice Landau structure in Py appears after tip swap, where all features are clear and true. One peculiar observation of the latter image is the spiral shape found in the Py Landau shape, which is expected to have straight, diagonal domain walls. The structure is 5 µm × 5 µm continuous Py thin film. Note the slightly elongated, rectangular shape of the structure in b), which in reality is a square structure. The observed elongation is due to non-linear responses in the piezoelectric fine scanning actuators, which should be considered when analyzing data from the MFM. The elongation phenomenon is especially prominent at the edges of the scanning window.

by an increased magnetic interaction with the sample. Once the desired applied field was reached, regular MFM scans could be performed to provide information about the micromagnetic state of the sample subjected to the applied field.

The field strengths experienced by the sample were a maximum of $\pm 100\,\mathrm{mT}$, although the most investigated range was between $\pm 20\,\mathrm{mT}$. The electromagnet is capable of resolving the applied magnetic field strength to within $\pm 0.1\,\mathrm{mT}$.

Specific experimental procedures are briefly detailed along with the relevant results in Chapter 6.

Chapter 6

Results

This chapter will detail the observations found in the micromagnetic modeling, sample fabrication results, and MFM experiments and imaging. A discussion of the results will be provided in the following chapter.

Throughout this thesis, fortunately, a great deal of interesting results have been obtained. The main focus will be the apparent superferromagnetic behavior of ensembles composed of trigonally stacked circular disks. Some interesting, auxiliary results will be briefly mentioned but not emphasized in the following presentation. Suggestions and ideas for further work to continue investigation of both the main and the auxiliary results will be provided in Section 8.1.

6.1 Micromagnetic simulations

This section will present the most relevant results from the micromagnetic modeling as described in Chapter 3.

6.1.1 Simulated relaxed states

In order to explore the ensemble properties as a function of stacking and disk parameters, a large set of simulations were performed. The results presented will focus on structures of 100 nm diameter disks with 30 nm spacing, as these are the most investigated structures by both simulations, and MFM, in this thesis. The scale and details of such geometry is also physically realizable with the chosen fabrication method.

Figure 6.1 provides simulation results from the relaxed structures after one of three main magnetization directions. It appears that magnets of similar colors are grouped in distinct regions. In Figure 6.2, a close-up of the fine detail of a similar structure is provided.

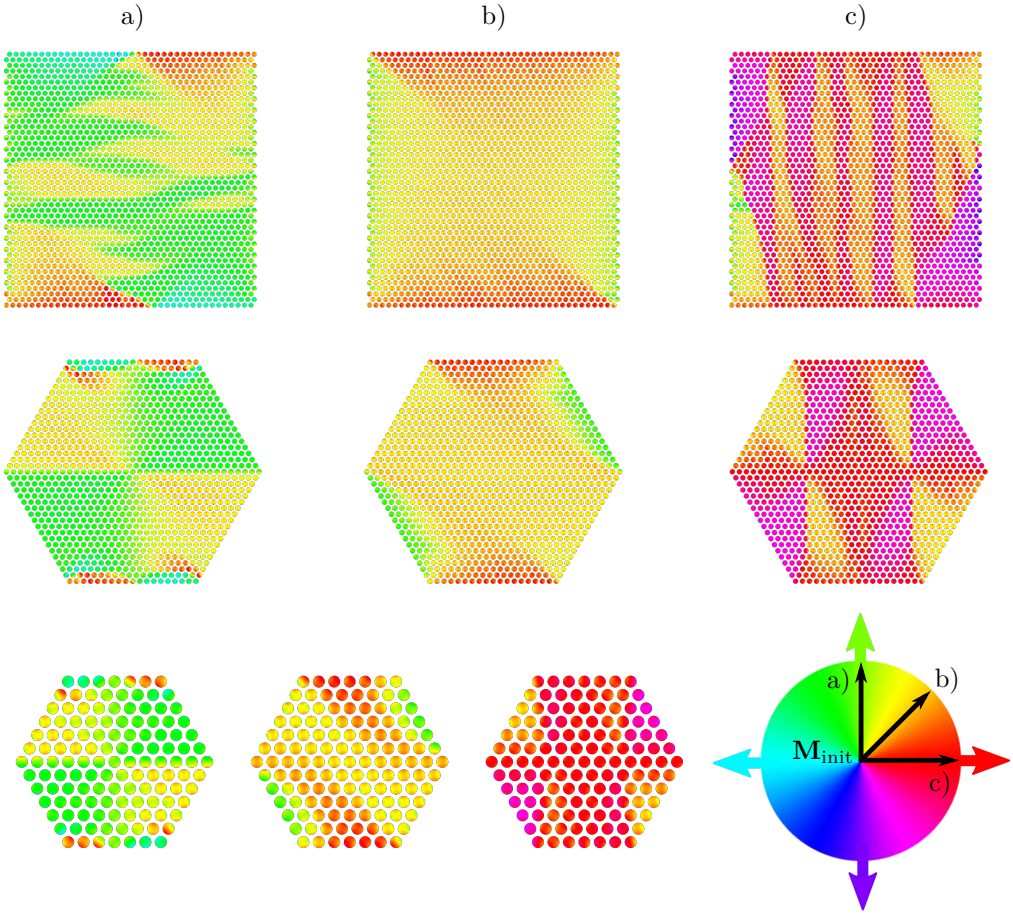

Figure 6.1: Simulated relaxed states, after an initial uniform magnetization along the a) vertical direction, b) 45° direction, and c) horizontal direction, also indicated in the color chart. All structures are assemblies of 100 nm diameter disks and 30 nm spacing. Top row: Trigonal lattice, 5 µm × 5 µm square bound. Middle row: Trigonal lattice, 5 µm hexagonally bound. Bottom row: Trigonal lattice, 2 µm hexagonally bound. The larger appearance of the bottom row is simply due to a higher magnification of these smaller areas. Note the distinct colored regions formed in all structures.

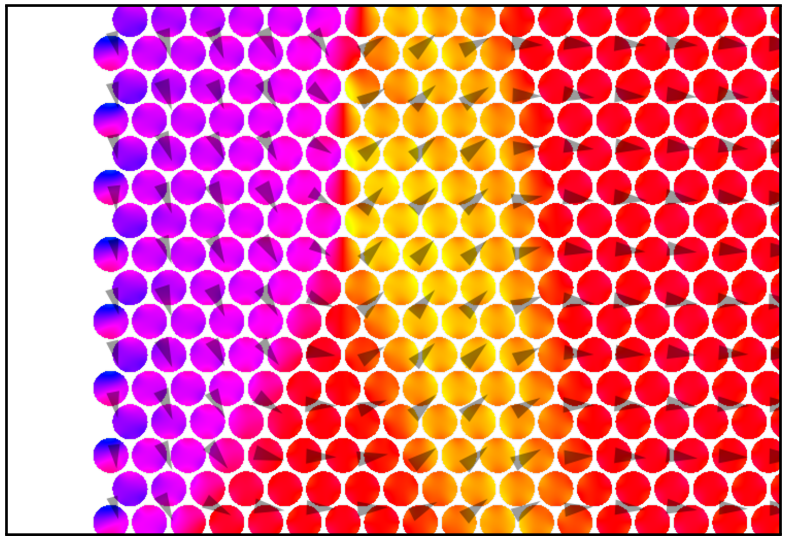

Figure 6.2: Close-up of the simulated relaxed state of an assembly of 100 nm diameter disks with 10 nm spacing. The assembly was subjected to a uniform magnetization along the horizontal direction (red). Note the three distinctly colored regions, their interfaced boundaries, and the relative direction of these regions.

6.1.2 Anisotropy analysis

In order to determine whether anisotropy effects emerge from the collective behavior of the ensembles, the results were analyzed with respect to magnetization direction. Specifically, the analysis determined the amount of MuMax3's computational cells that were aligned along certain directions. As the trigonal lattice is suspected to incur a threefold symmetry, it is expected that three easy axes with 60° separation (along the densely packed directions) are coupled with three hard-axes with an offset of 30° (along the sparsely packed directions).

One approach to investigate the stacking effect on anisotropy is to sort each computation cell into one of two regions: One region of all cells that have a magnetization direction which is closest to the densely packed directions, and another region that has a magnetization that is closest to the sparsely packed directions. An example of such classification is provided in Figure 6.3.

A more quantitative approach to analyzing the distribution of magnetization directions is to sort the cells into bins of 1° width, over all possible angles. The amount of cells in each bin can be divided by the total amount of magnetized cells in the simulation in order to establish the fraction of cells along any particular direction. An example of such sorting is provided in Figure 6.4.

For an isotropic material in a demagnetized state, the distribution of cells with a magnetization along each direction is expected to be completely uniform. For an initially uniformly magnetized state such as the ones simulated, an isotropic system is expected

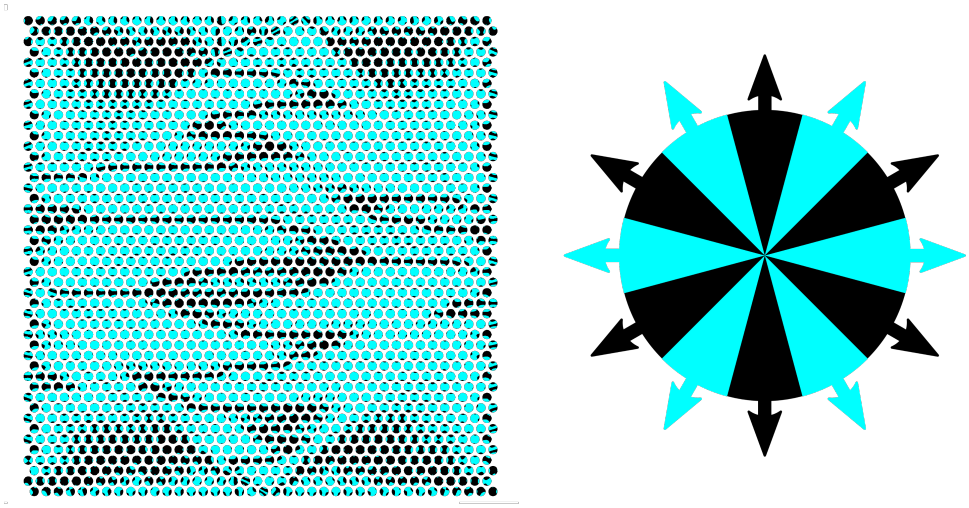

Figure 6.3: The structure from Figure 6.1a) (top row), where the computation cells are classified according to their magnetization direction. The blue color shows the cells that are closer to a suspected easy axis. Cells that are closer to a suspected hard axis are indicated in black. Illustrated on the right is the discrete color map representing the sorting classification. Note that the color map has 50 % of each color, while the structure does not seem to have this equal distribution.

to have a distribution with a peak around the initial direction. For anisotropic systems, the expected distribution should have peaks around easy axes and minima around hard axes.

6.1.3 Simulated MFM images

This chapter will, among other things, present a series of MFM acquired images, and therefore a quick note on their representation is appropriate. These images will be presented as a colormap, where each point in the two-dimensional image is colored according to the degree of interaction with the tip. As mentioned in Section 2.4, the interaction is due to the vertical component of the stray field, and the magnetic interaction will modulate the oscillation of the tip so that a phase difference between the driving electronics and the recorded amplitude is incurred. This phase difference is the value that is plotted as a color in the presented MFM images. For simulated MFM images, however, there is no need to plot the phase difference (which is a rather indirect quantity) and the z-component of the stray field above the sample can be plotted directly. The scale of the color value is dependent on the acquired image, and is scaled and presented in arbitrary units in order to maximize perceived contrast for the specific image. Generally, a brighter color indicates a stronger interaction with the tip while a darker color indicates an opposite interaction.

Simulated MFM observations were obtained with native MuMax3 functionality. The

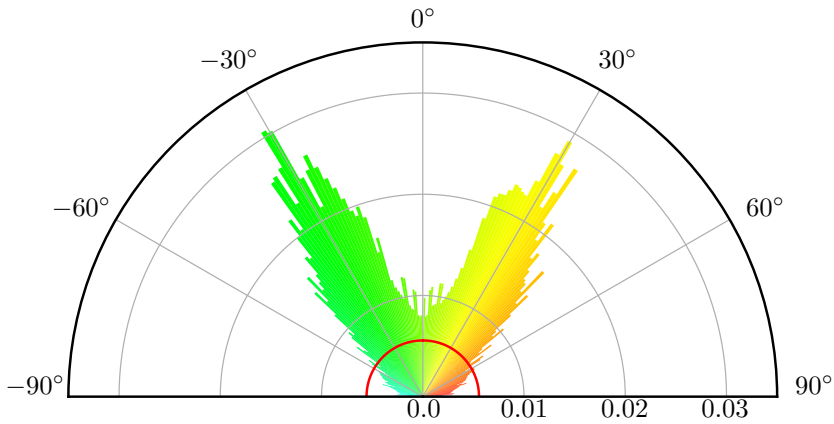

Figure 6.4: Quantified presence of magnetization directions from simulation. The data is gathered from the ensemble in Figure 6.1a) top row, with 100 nm diameter disks and 30 nm spacing, initialized along the 0° direction. The radial axis shows the fraction of total cells in the simulation. Thus, the peak value at 30° indicates that roughly 3 % of the cells have a magnetization at $(30.0 \pm 0.5)°$. The red line indicates a theoretically completely isotropic distribution at $r = \frac{1}{180}$. The color of the dots is concurrent with the MuMax3 color map, simply to ease visualization.

images are obtained by extracting the z-component of the magnetic field at each point above the sample at a specified lift-height and calculating how this field would interact with a magnetic dipole tip. While these simulated images only provide the theoretically ideal MFM images, they can give a hint in regards to what to expect from the experimentally obtained MFM images. Increasing the lift-height naturally reduces the amount of fine-details of the micromagnetic state resolved, which might be a more accurate representation of the experimental case. An example of such generated MFM images is provided in Figure 6.5.

6.1.4 Applied magnetic field

In order to gain insight into the ensembles' behavior under a changing applied magnetic field, additional simulations were performed where an applied external field was gradually changed. The ensembles were initialized with random magnetization followed by a saturating field with a field strength of −70 mT. The applied field was then increased from 0 mT to 20 mT with an increase in steps of 1 mT. The simulation tests were performed on disk sizes that had shown monodomain behavior (50 nm and 100 nm diameter) and near-monodomain behavior (150 nm diameter). The tested spacing range reflected the physically fabricated samples, i.e., 30 nm to 50 nm.

An example of a test involving varying applied magnetic fields, performed on a hexagonally bound, 5 µm wide, trigonal lattice with 100 nm diameter disks and 30 nm spacing is provided in Figure 6.6.

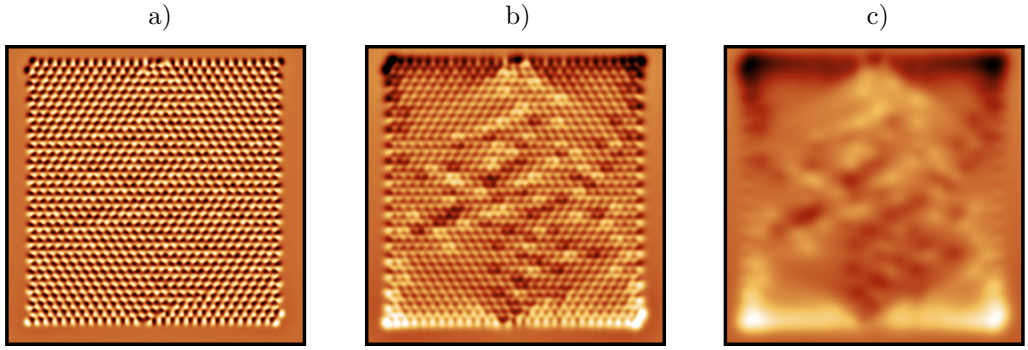

Figure 6.5: Simulated MFM images of the ensemble from Figure 6.1a) top row. a) 75 nm lift, the individual disk's magnetization is resolved, which is not achievable with the available experimental equipment. b) 150 nm lift, the micromagnetic structure is finely resolved. c) 300 nm lift, details are somewhat blurred, but an overall magnetization can be observed. The real MFM images will be obtained at about 100 nm to 200 nm lift and will be resolved to somewhere between b) and c).

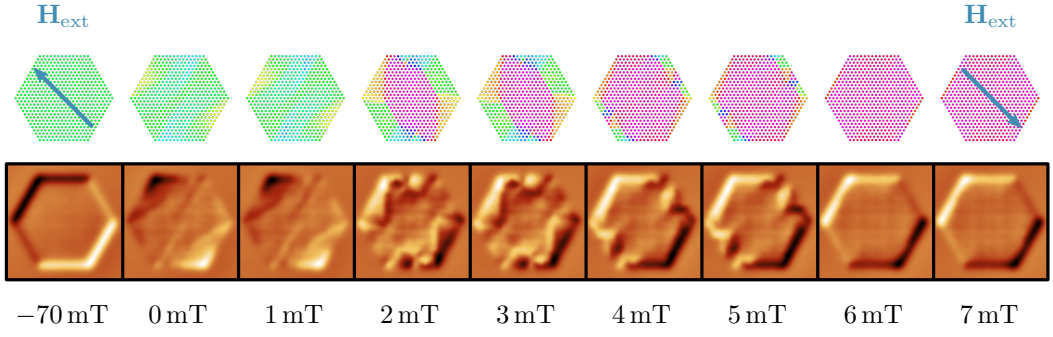

Figure 6.6: A simulated, trigonal lattice, 5 µm hexagonally bound, ensemble is exposed to varying applied magnetic fields. The applied field, $\mathbf{H}_{\text{ext}}$, is aligned along a 45° direction, as indicated by the blue arrows. Top row: Magnetization by color, following the MuMax3 color map. Bottom row: Simulated MFM images of corresponding structures.

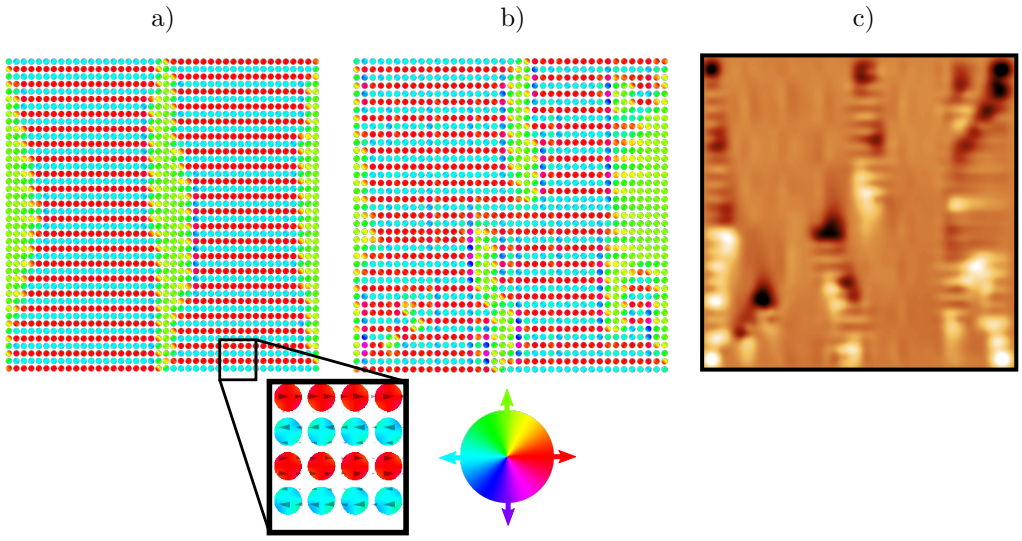

Figure 6.7: Simulation of 5 µm × 5 µm ensembles with a square lattice stacking. a) 100 nm disks with a spacing of 20 nm. b) 100 nm disks with a spacing of 30 nm. Note the anti-parallel alignment of the macrospins in some regions (red and cyan are oppositely aligned). c) Simulated MFM image of the structure in b). Note the regions of antiparallel macrospins are concurrent with the low-contrast regions in the MFM.

6.1.5 Square lattice ensembles

Simulations were carried out for other systems as well, including square stacked lattices of circular disks. This section highlights a few interesting results, although the focus points of the thesis are the states observed in trigonal lattices. A few selected examples of square lattice relaxed states are provided in Figure 6.7.

One particularly interesting example of such a square lattice ensemble is provided with full-detail in Figure 6.8.

6.2 Inspection of fabricated samples

The fabricated samples were inspected with a scanning electron microscope (SEM) following lift-off of Py. The SEM images convey a successful fabrication process, with pristine pattern fidelity, as seen in Figure 6.9. However, some parts of the fabricated samples showed signs of incomplete lift-off, also provided in Figure 6.9. Fortunately, the majority of the structures showed complete lift-off, and exhibited well-fabricated patterns.

The samples were additionally inspected with MFM, and a MFM image of a region where incomplete lift-off is observed in the SEM image is provided in Figure 6.10.

The samples were also inspected with AFM scans of the surface. These scans revealed some microscopic defects at the edges of the individual nanomagnets, as shown in Figure 6.11. The edges had specular defects with a height of approximately 10 nm to 15 nm,

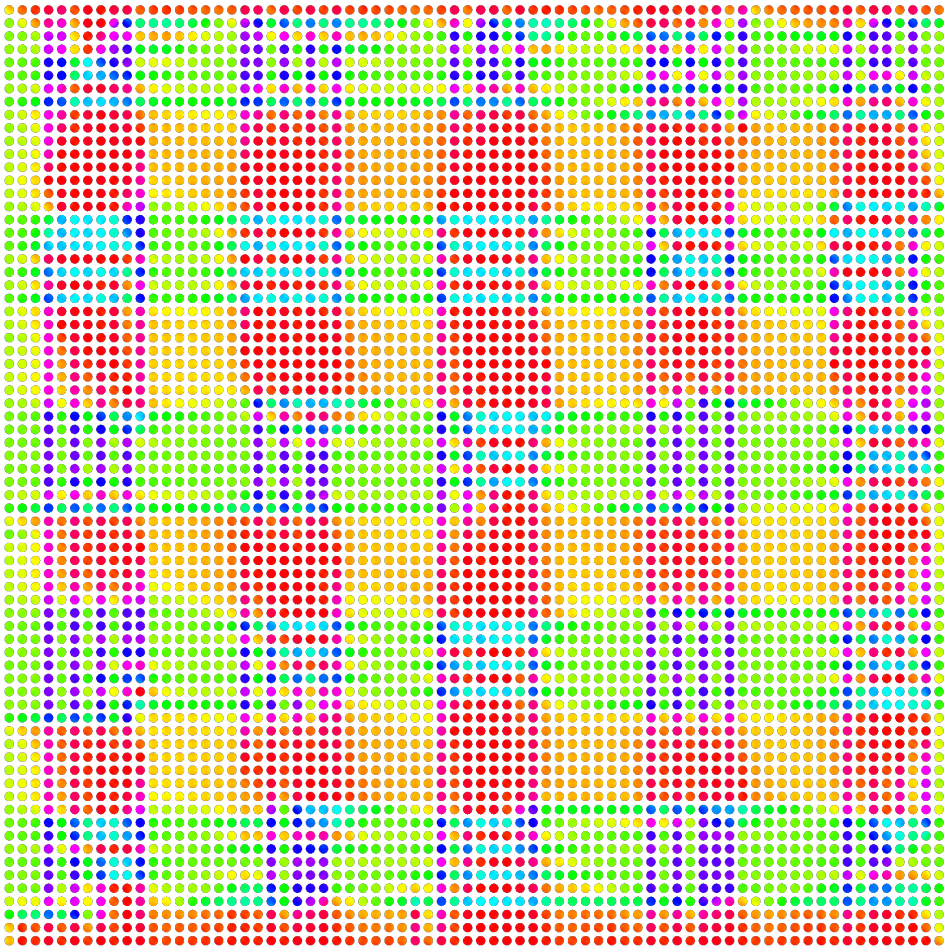

Figure 6.8: Simulation of a relaxed square lattice ensemble of particular interest. The disks are 100 nm in diameter and with a spacing of 20 nm. Note the long-range ordering of both SAFM and SFM domains.

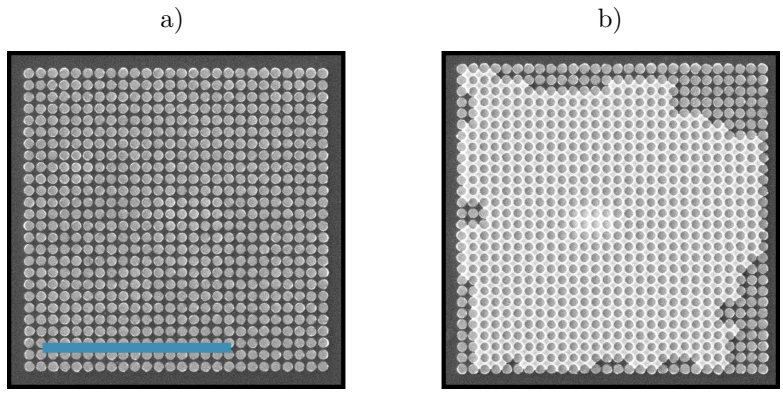

Figure 6.9: SEM image of a squarely stacked ensemble of nanomagnets, with a disk diameter of 150 nm and an inter-magnet spacing of 40 nm. a) The image clearly demonstrates a successful fabrication process with crisp details and completely regular stacking. The blue scale bar is 3 µm wide. b) A SEM image of a similar structure, demonstrating incomplete lift-off. A continuous thin film of Py with embedded nanomagnets can be seen.

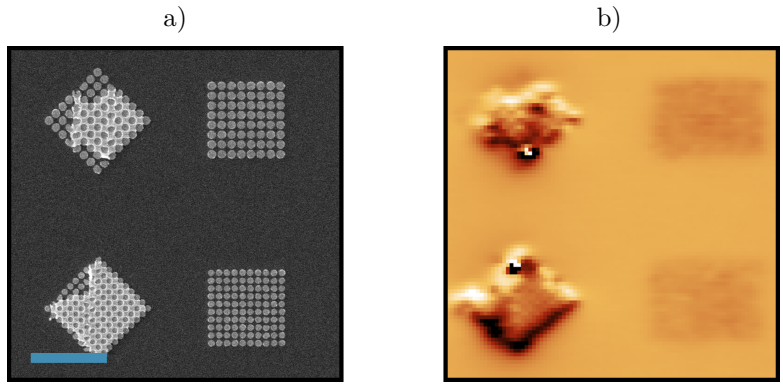

Figure 6.10: The effect of incomplete lift-off on the acquired MFM images. Left: SEM image showing the incomplete lift-off for the structures on the left side. The blue scale bar is 2 µm wide. Right: The MFM image obtained of these structure show that the incomplete lift-off structures exhibit a significantly stronger interaction with the tip, as expected. Note that the correctly fabricated structures have almost no magnetic contrast, due to the MFM contrast being scaled for the strong interaction with the left-side structures.

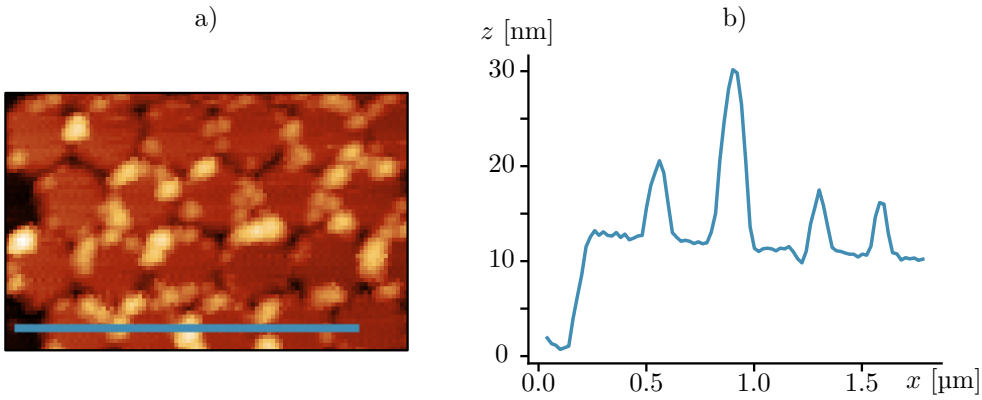

Figure 6.11: Defects in fabrication. a) An AFM image of a trigonally stacked lattice, the disks are about 200 nm in diameter. Specular defects are visible. b) Height profile along the blue line indicated in a). From the line profile it is possible to determine the height of the defects to about 10 nm to 15 nm.

as seen in the provided height profiles in Figure 6.11.

However, it is also worth noting that not all samples exhibited these kinds of defects.

6.3 Magnetic force microscopy imaging

This section will present the results from experimental MFM observation and manipulation of ensembles through the use of an applied field. The section represents the bulk of the results from this thesis. While there are interesting results beyond those presented here, the focus will be on the results pertaining to the supposed SFM states observed in trigonal lattices of circular disks.

6.3.1 Magnetic microstructure

As mentioned in Chapter 5, the initial MFM scans were too close to the sample and interaction from the tip cause them to behave as structures with no stray fields indicative of in-plane magnetization. However, lifting the tip to about 100 nm above the surface revealed the first indication of magnetic microstructure. Figure 6.12 provides an example of micromagnetic structure imaged at a good lift height, for a 5 µm × 5 µm square bound, trigonal lattice of 100 nm disks with a spacing of 30 nm.

6.3.2 Net magnetized states

By applying an external field and imaging the behavior of the ensemble with the MFM, more information can be gained about the state and the behavior of the fabricated system. To further investigate the ensemble from the previous section, an external magnetic field was applied at 45° to the ensemble's bounding edges. The magnetic field was gradually

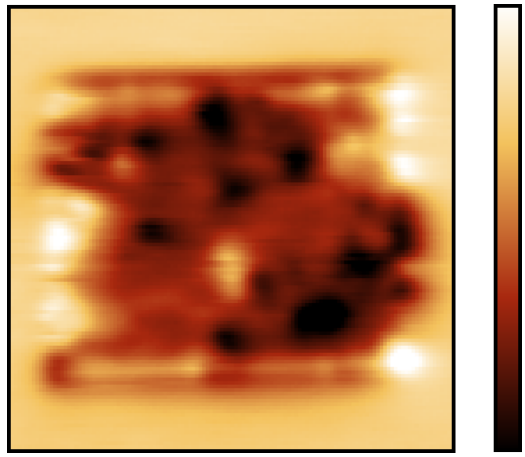

Figure 6.12: MFM image of the fabricated sample. The ensemble consists of a trigonal lattice of 100 nm diameter disks with a spacing of 30 nm in a square field with 5 µm side lengths. The color map ranges from black to white as indicated on the left. It represents the stray field interaction with the tip in the form of a phase modulation, given in arbitrary units to maximize perceived detail contrast.

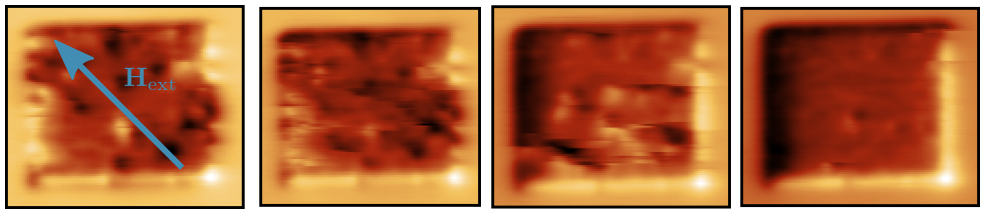

Figure 6.13: MFM images of the ensemble from Figure 6.12 in an increasing applied magnetic field. The field direction is indicated by the blue arrow. The ensemble clearly exhibits a transition into a state of near-uniform magnetization, at 10.0 mT.

increased in steps of 2.5 mT, and MFM scans were performed (while still applying the field) at each step. The resulting MFM images are presented in Figure 6.13.

Examining the MFM image obtained with a field strength of 7.5 mT closely, it appears there are some horizontal stripes marking a change in the imaged structure. These stripes are parallel to the scan direction, and are indicative of the tip interacting with the sample and thereby changing the magnetization of the sample. The supposed tip-sample interaction was further investigated after the first 7.5 mT scan. Instead of increasing the applied magnetic field to 10 mT, the tip was lifted an additional 20 nm and a new image was captured. The purpose of the tip lift was to ensure a scan where the tip interacted less with the sample than in the first scan. The images captured in this process are presented in Figure 6.14.

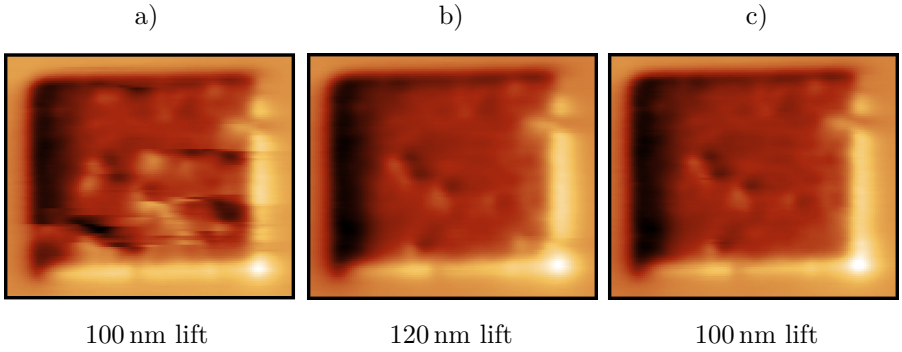

Figure 6.14: MFM images of the ensemble (from Figure 6.12) transitioning to a net magnetized state. Note that the applied field is kept constant. a) Scanned at 100 nm lift height. The structure seems to be affected by the magnetic scanning tip, and appears to switch states while being scanned. b) The structure is scanned at a higher 120 nm lift height, ensuring less interaction. The net magnetized state is observed. c) The magnet is scanned at the same lift height as in a), showing no signs of disturbance from interaction with the tip.

6.3.3 Magnetic anomalies in net magnetized SFM state

While the observed state at 10 mT is nearly uniform, it is not completely uniform, and there are some persistent magnetic anomalies. These anomalies produce a stray field from points inside the ensemble that shows up in the image acquired by MFM. It was found that by increasing the field strength further, the anomalies could be eliminated. Some anomalies required higher field strengths to remove. The elimination of one such anomaly while increasing the field strength from 7.5 mT to 10 mT is shown in Figure 6.15. Furthermore, the elimination of the anomalies seemed permanent, as they were not reintroduced when re-lowering the applied magnetic field.

6.3.4 Remanent SFM magnetization

The previously presented MFM data has shown that the ensembles are capable of exhibiting magnetized states while under an applied field. After removing the external magnetic field, the ensembles were again imaged with the MFM. The acquired MFM images show that the ensemble did remain in a net magnetized state. The process was repeated for a field applied in the opposite direction (denoted as a negative field strength), and the ensemble again exhibited a net magnetization, this time in the opposite direction to the initial remanent state. The MFM images are provided in 6.16

A surprising observation from this experiment is the fact that the remanent magnetization seems to have a slightly different orientation than the applied magnetic field. While the field is applied, the magnetization clearly corresponds with the applied field direction, diagonally across the ensemble. However, the remanent magnetization in both cases in Figure 6.16 seem to be parallel to the horizontal edges of the ensemble.

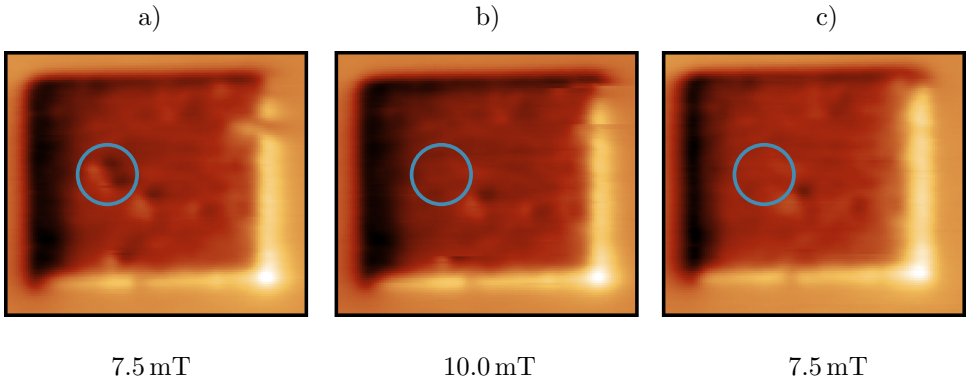

Figure 6.15: Elimination of a magnetic anomaly from the structure in Figure 6.14. a) MFM image acquired at 7.5 mT applied magnetic field strength. The anomaly is indicated in blue. b) Once an external field strength of 10 mT is applied, the anomaly can no longer be observed. c) The anomaly does not reappear when returning to the original field strength (7.5 mT).

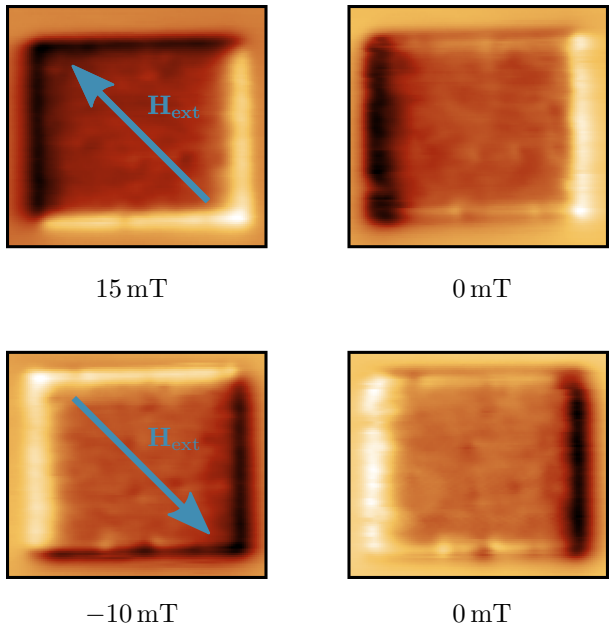

Figure 6.16: MFM images of ensemble before and after removal of the applied magnetic field. The structure is the same as in Figures 6.12 to 6.15. Top: A field in the positive direction is removed, and a net magnetization is observed. Bottom: A field in the negative direction is removed, and the ensemble manifests a net magnetization in the opposite direction to the top case.

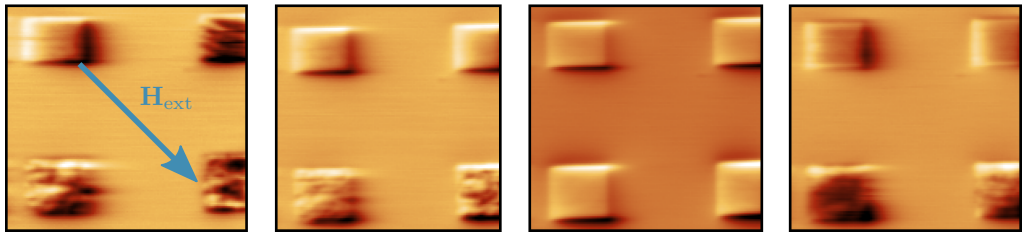

Figure 6.17: MFM images of ensembles experiencing a strong applied magnetic field which is subsequently removed. The ensembles in the top row of each image have disks with a diameter of 100 nm, and the bottom row 150 nm. The left column in each image are ensembles of 40 nm spacing and the right column 30 nm spacing. All ensembles are trigonal lattices of circular disks.

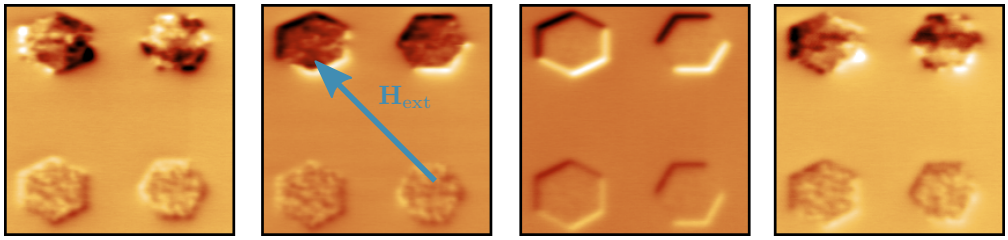

Figure 6.18: MFM images of hexagonally bound ensembles experiencing a strong applied magnetic field which is subsequently removed. The ensembles in the top row of each image have disks with a diameter of 100 nm, and the bottom row 150 nm. The difference between the left and right column is simply a rotation of 30°. All ensembles are trigonal lattices of circular disks.

6.3.5 Effect of ensemble parameters

Up until this point, the only ensemble that has been considered is the one with 100 nm diameter disks and 30 nm spacing. This section aims to include results from examples of other ensemble compositions, in an attempt to establish differences in the observed behavior.

Looking first at the ensembles that are the most similar to the one discussed until now, a similar experimental procedure was performed. Figure 6.17 provides a series of MFM images detailing the behavior of four ensembles undergoing a strong applied field which is subsequently removed. The four ensembles includes the previously discussed ensemble, in addition to ensembles of either a 50 nm increase in diameter, a 10 nm increase in spacing, or both.

The effect of the lattice boundary shape was also tested. Figure 6.18 provides an example of hexagonally bound trigonal lattice ensembles. The figure also includes ensembles with smaller disks, of 50 nm diameter.

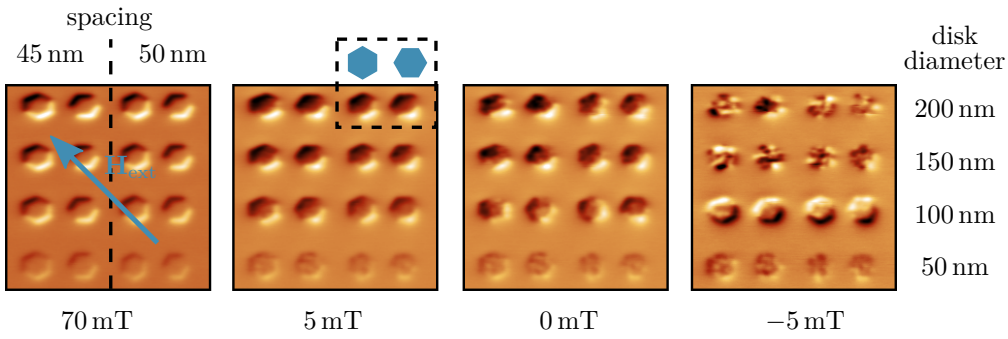

Figure 6.19: MFM images of hexagonally bound ensembles experiencing a strong applied magnetic field which is subsequently removed. All ensembles are trigonal lattices of circular disks. The diameter of the disks are indicated on the right. The disk spacing is indicated for the first image, and applies to all images. The pair of columns with the same spacing are rotated 30° with respect to each other. Note the different states of the ensembles of different diameter disks in the last pane.

In addition to fabricating ensembles of different shapes, the size limitation of the ensembles was also tested. A set of hexagonally bound ensembles, similar to the once shown in Figure 6.18 except with an ensemble horizontal diameter of 2 µm instead of 5 µm, can be seen in Figure 6.19.

6.3.6 Rotation of net magnetization

While acquiring images of the ensembles from Figure 6.19 experience a ramping magnetic field, a notable observation was noticed. For the ensembles with disk diameters of 100 nm the ensemble magnetization seemed to rotate in correspondence with the field strength, as shown in Figure 6.20.

6.3.7 Auxiliary MFM results

In addition to the main results presented in the previous sections, this section will detail some auxiliary results of note that have not been heavily investigated or discussed in depth.

Square lattice ensembles

The bulk counterpart to the presented trigonal lattice ensembles are the square lattice ensembles. All the experiments performed on the trigonal lattice ensembles were also carried out on the square lattice ensembles. These experiments further confirmed the observations presented in Sections 6.3 through 6.3.5. The rotating magnetization mentioned in Section 6.3.6, however, was not found for the square lattices.

One image series of note is provided in Figure 6.21, and will be discussed in the next chapter.

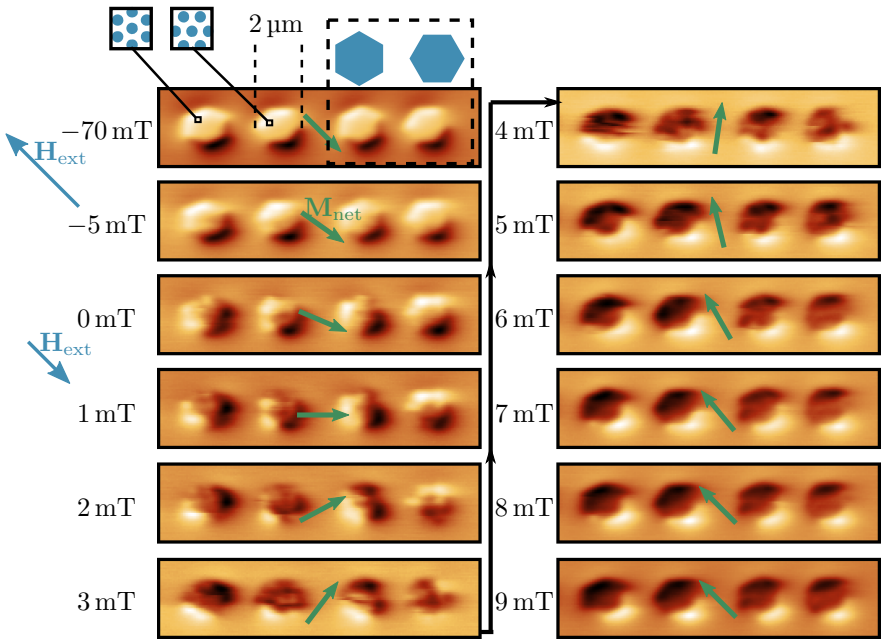

Figure 6.20: Ensemble magnetization, $\mathbf{M}_{\text{net}}$, rotating with increased applied magnetic field (along a 45° diagonal). The green arrow indicates the apparent magnetization direction of the ensembles. The blue arrows indicated the applied field, $\mathbf{H}_{\text{ext}}$. Instead of switching magnetization suddenly, the net magnetization seems to change gradually by rotating in-plane. However, the rightmost structure is an exception to this rotation, as it changes more or less spontaneously.

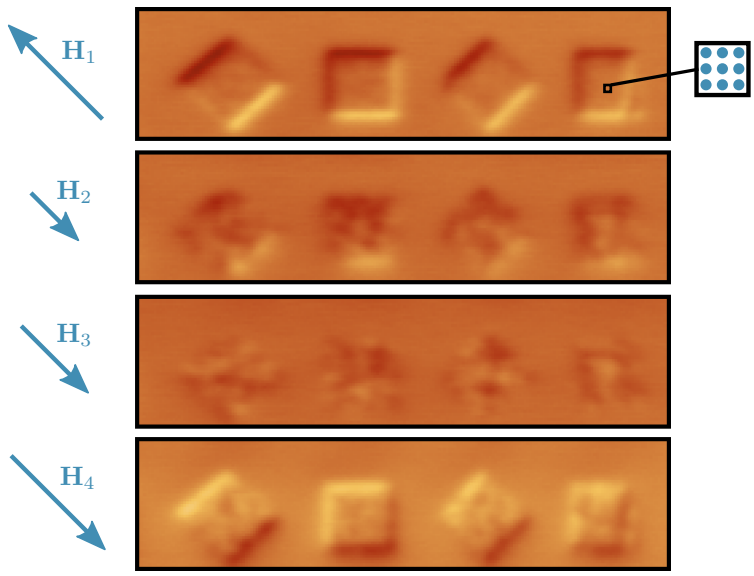

Figure 6.21: Square lattice ensembles imaged with MFM. The ensembles are first saturated with a strong field in one direction, followed by an increasing field in the opposite direction. In other words, using the notation H_i for the field magnitudes, then $H_1 < 0\,\mathrm{mT} < H_2 < H_3 < H_4$. Note the low contrast on the third pane.

Stacked ellipses

In addition to ensembles of circular disks, some ensembles of stacked elliptical disks were fabricated. These disks have a varying degree of shape anisotropy (depending on the ratio of the major to minor axis) and it is expected that the shape emulates a uniaxial anisotropy contribution to the SFM state. Not surprisingly, anisotropy favoring magnetization along the elongated direction of the ellipses was observed and quite prominent, as shown in Figure 6.22.

Appended results

Other results, not directly related to the topic of supermagnetism, but rather emergent behavior of magnetic ensembles, are provided in Appendix B.

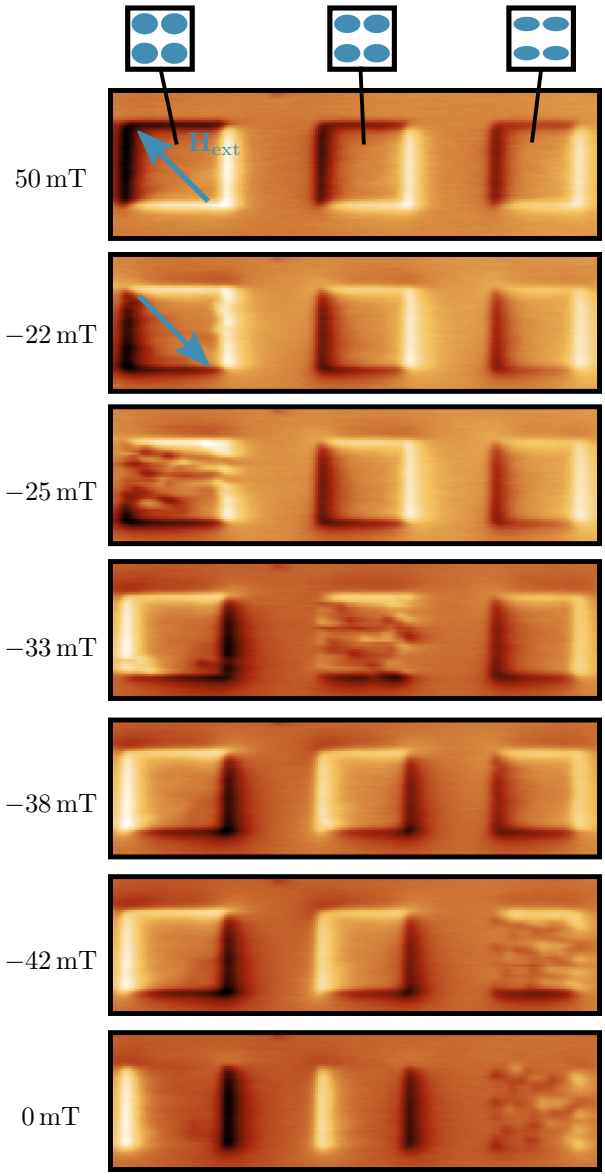

Figure 6.22: Ensembles of squarely stacked ellipses in an applied magnetic field. The ellipses are elongated in the horizontal direction. The eccentricity of the magnetic ellipses grows towards the right, as illustrated (exaggeratedly) in the top insets. The different eccentricity leads to a switch in magnetization direction at different applied field strengths. Note the final pane with no applied field, and also no apparent net magnetization of the most elliptical ensemble.

Chapter 7

Discussion

This chapter will refer to the results presented in Chapter 6 and disucss their relevance with respect to the topic of supermagnetism. The results are coupled with a discussion provided in the context of the theory in Chapter 2 and the methods presented in Chapters 3, 4, and 5.

The discussion will be presented in the same order as the results, starting with the simulations and ending with the experimental MFM results. However, there will be cross-references between relevant results that should be discussed concurrently. Finally, a review of discrepancies between the simulated results and the experimentally observed results will be provided.

7.1 Simulated supermagnetism

7.1.1 Superferromagnetic behavior in trigonal lattices

Superferromagnetic domains

The simulation results quickly indicated that the total ensemble behavior was able to sustain a remanent magnetization in the absence of an applied magnetic field. Indication of remanent magnetization can be seen by the calculated ground states provided in Figure 6.1, where it is clear that they have a net magnetization in the absence of an applied field.

Additionally, the ensemble states exhibit long-range ordering in larger regions of uniform magnetization (similar to the formation of FM domains). The observed long-range ordering is consistent with the suspected formation of superferromagnetic (SFM) domains, discussed in Section 2.3.2 These regions will be referred to as SFM domains. The SFM domains were also found to have a favorable magnetization direction parallel to the lattice's densely packed directions, which can be seen from Figure 6.3 and 6.4. As there is no magnetocrystalline anisotropy in the material, and no reason to suspect that the simulation method has an inherent, threefold symmetrical anisotropy error, the observed

threefold symmetry must be due to the lattice geometry.

It is possible to argue that the anisotropy might be an effect of the finite bounding area of the ensembles. A threefold symmetry effect of the bounding area would be a relevant point if the effect was only observed for the hexagonally bound ensembles. However, the effect is demonstrated for the squarely bound ensembles, which does not exhibit any threefold symmetry. Therefore, the only remaining cause of such a threefold symmetry is the trigonal lattice stacking of the nanomagnets.

Thus, it seems that the lattice stacking is able to influence magnetic hard and easy axes for the SFM material, even though the FM nanomagnets exhibit no such magnetic anisotropy. All these findings are indicative of superferromagnetic behavior.

It is worth noting that for the simulated range of spacing, 10 nm to 50 nm, the dipole coupling is sufficiently strong in order to induce the observed long-range ordering. A larger spacing is expected to reveal SPM or super-spin glass behavior, although this was not thoroughly investigated.

Superferromagnetic boundaries

Another interesting observation is the interface between two non-parallel SFM domains, referred to as SFM domain walls. The SFM domain walls were found to range from soft and wide to sharp and narrow. In other words, the change in magnetization from one SFM domain to another could be gradual and take place over a large region of many nanomagnets, or it could happen in the space of a single nanomagnet. For the square stacked lattices, regions of antiparallel magnetization were found to have no SFM domain wall in the magnetic material at all, only an abrupt change in magnetization across two neighboring nanomagnets. In general, sharp SFM domain walls were found to be more frequent between SFM domains with a greater difference in magnetization directions. This SFM domain wall behavior is supported by the binary-colored image presented in Figure 6.3, where the black regions can be seen to correspond to SFM domain walls. This SFM domain wall behavior is quite different from FM domain wall behavior, as FM domain walls are larger for a greater change in magnetization (due to the exchange stiffness).

The different schemes of SFM domain wall change is particularly well illustrated in Figure 6.2. The purple-to-red and red-to -yellow transitions are transitions of 60° magnetization change, and the SFM domain walls are smooth and follow the supposed easy axes. However, the purple-to-yellow transition, which is a 120° transition is more abrupt and the disks at the border are only quasi-monodomain. The abrupt SFM domain walls seem to follow the hard axes. The tendency for SFM domain walls to lie along hard axes is an interesting behavior that is certainly manifested in the simulations. However, why such behavior is observed is hitherto unknown and could be worthy of a potential future investigation. If physical MFM scans of fabricated samples shows signs of SFM domain walls along stacking directions, this could be utilized as definite evidence for the SFM state.

7.1.2 Superantiferromagnetism in square lattices

Square lattices proved to behave quite different from the trigonal lattice. Most notably, they were seen to exhibit superantiferromagnetic (SAFM) behavior, where the disk magnetizations are ordered in an anti-parallel fashion. The square lattice ensembles could also fall into SFM states, depending on the magnetization direction and lattice parameters.

The SAFM behavior was only found in disks of size 150 nm and below, and there seemed to be certain disk spacings that were ideal. In order to achieve a maximal amount of domains with SAFM ordering, the optimal disk spacing seems be in the vicinity of 30 nm to 40 nm. The fact that there is a narrow optimal range where SAFM is the preferred ground state indicates that it will be hard to experimentally determine the state. The narrow SAFM parameter space might explain the lack of the clear experimental observation of SAFM states. However, simulated MFM images show that the state should have little (or no) magnetic contrast, which would be a clear indicator that the ensemble is in a SAFM state. Considering Figure 6.21, the low contrast in the intermediate state could be explained by SAFM states. (Simulated MFM images demonstrating this is provided in Figure 6.7.)

7.1.3 Simulated MFM results

The results of the simulated MFM images are not themselves worthy of much discussion, as they are mostly used as a tool to identify the expected MFM images acquired by experimental means. They provide a way to analyze the experimentally acquired images in order to establish a picture of the micromagnetic structure within the sample.

Studying the simulated MFM image in Figure 6.5, it is clear that contrast will only be available where the magnetization of the sample changes significantly over a small region. The contrast will be strong where magnetic north or south poles are in vicinity of other poles of the same polarity. White contrast will be observed where there is an abundance of south poles, while black contrast will be observed where there is an abundance of north poles. Additionally, uncompensated poles, e.g. south poles at the edge of a structure that do not have neighboring north poles, will incur a stray field indicative of a region of south pole abundance. This last part can be observed along the horizontal edges of the structure in Figure 6.5. It is clear that the structure, which is magnetized vertically up in the image, has a black edge on top and a white edge at the bottom, indicating a net magnetization in that direction.

The most useful piece of information provided by the simulated MFM images was the fact that the structures might have complex SFM domain formation although the MFM image indicates a structure with a rather uniform magnetization. An example of a complex domain formation yielding simple MFM images can be seen in Figure 6.5.

Also, one additional, interesting result is the nature of SAFM materials in an MFM image. As apparent from Figure 6.7, the SAFM regions are completely free of magnetic contrast, and the only visible contrast seemingly stems from the SFM domains.

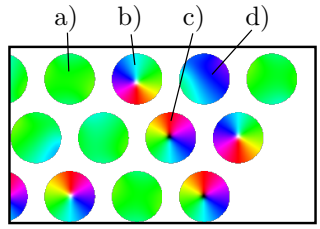

Figure 7.1: Simulated 150 nm diameter disks, exhibit monodomain and vortex states. To facilitate discussion, this illustration is provided to display the possible states of a nanomagnet. a) Monodomain state, completely uniform magnetization. b) A vortex state, where the topological vortex magnetization is pointing out of the plane. c) A vortex state oriented opposite of b). d) A near-monodomain state, that is not completely uniform but has some change of magnetization, although no topological vortex.

7.1.4 Applied magnetic field

When simulating applying an external magnetic field, the simulation results show that the magnetization of the ensemble switches through a mechanism that can be described as a sudden change. The change is sudden within the resolution of the change in applied field strength, i.e., it might be possible to observe intermediate steps if the field was changed in smaller steps than 1 mT. For ensembles with no vortex states, (see Figure 7.1), the behavior is similar to the change of magnetization in an anisotropic magnetic material. The applied field strength must overcome a coercivity barrier in order to change the magnetization. Once the barrier is passed, a new SFM domain with magnetization parallel to the applied field is formed. This behavior can be observed in the provided simulation results in Figure 6.6. The new domain then grows and can be seen to dominate the ensemble more for increasing applied field strength. In the figure, the magnetization is saturated at about 6 mT, which can be construed to be the applied field corresponding to a magnetization representing material parameter M_S of the SFM structure.

However, if vortex states are present, as they were for larger disks with an initializing field of insufficient strength, the magnetization reversal mechanism is more gradual. The presence of disks with a vortex state facilitates the switching of some neighboring magnets before others. The result might thus be a more gradual reversal, starting with the vortex state magnets as nucleation spots. The observed effect of vortex disks is interesting as it may provide a qualitative reference point for experimental MFM observations, although specific results are not provided in this thesis. The vortex states might explain the discrepancy between the experimentally observed in-plane rotation where the simulated results show a sudden change.

7.1.5 Superdupermagnetism

A final curiosity observed is the complex state observed in Figure 6.8, consisting of long-range order of both SFM and SAFM domains, a “superdupermagnetic” state. The provided superdupermagnetic state was observed in small disks (50 nm) with tight stacking

(around 20 nm), and similar states were found for similar structures.

While the superdupermagnetic state might be hard to achieve experimentally, the result can be ascribed some significant value. Similar superdupermagnetic states were found in ensembles of neighboring parameters, ranging from 50 nm to 100 nm in disk diameter and 10 nm to 30 nm spacing. These structures are physically realizable, and the fact that superdupermagnetism was observed for different initial magnetization might point towards feasibility with respect to observing such a state in physically fabricated samples. However, it is suspected that the fabrication must be completely flawless, as the result *might* be due to the perfect nature of the simulations.

The fact that superdupermagnetism is observed, however, and seems to be a stable state, also indicates that the SFM and SAFM states (of which superdupermagnetism is comprised) are stable simultaneously. In other words they are stable in the same structure and under the same conditions, which supports the existence of a switchable SFM/SAFM state.

7.2 Fabricated samples

Some fabricated samples showed signs of incompete lift-off. Incomplete lift-off will lead to an increased amount of magnetic thin film in the affected regions of the sample. The contrast in the MFM images is expected to convey this increase of magnetic material as there will be a larger, total magnetic moment to interact with the magnetic MFM tip.

The sample defects are, however, rather small, as seen from the graph in Figure 6.11, and would contribute with only a tiny amount of magnetization. Thus, it is reasonable to assume that these defects were not detected in the SEM images due to their minuscule size. The small size also implies that it is reasonable to assume that they are not critically devastating defects. However, they introduce an unknown element and possibly some degree of magnetic shape anisotropy to the fabricated nanomagnets. Discrepancies in the observed magnetic behavior and the simulated behavior might be due to tiny defects like this, or other similar, undetected defects. The defects might be due to the fact that an undercut profile of the resist, which is ideal for lift-off processes, was not used. Thus, it might be possible to improve the quality of the fabricated samples by fabricating the resist with an undercut profile.

In summary, the samples were of a high quality and true to the designed pattern. Some parts of the samples had minor defects, which might explain deviations from the exact simulations. However, minor defects are expected, as any physical system will always contain some degree of imperfection.

7.3 MFM

This section will discuss the results from the experimental MFM observation. The discussion is supported by the results presented in Sections 6.1, 6.2, and 6.3. In other words,

the simulation results as well as the experimentally observed results.

7.3.1 Long-range ordered magnetic structure

The observed magnetic microstructure is larger than individual magnets. While it is hard to discern the true, in-plane magnetization direction of the ensemble in Figure 6.12, it is reasonable to assume that there is some long-range ordering. The presence of long-range ordering larger than individual disks can be argued from the fact that the white, brown and black regions observed are larger than the possible contrast from individual disks. An SFM domain will not provide any MFM contrast except at the interface between other SFM domains of a different magnetization, as evidenced by the MFM simulations discussed in Section 6.1. Therefore, it is possible that the low-contrast areas represent SFM domains, and the bright and dark regions are the SFM domain intersection where the stray field extends vertically and reveals contrast. The hypothesis that the contrast is due to the presence of SFM domains is further supported by the contrast found along the edges of the ensemble, where the stray field of a uniformly magnetized region necessarily extends in all directions when the magnetic material is terminated. The spread of the demagnetizing field provides contrast in the MFM image due to the vertical component (z-component) of the stray field interacting with the MFM tip.

The low contrast areas could also be explained by the magnets manifesting vortex states, which would give little contrast, as demonstrated by MFM simulations of such states. However, vortex states would also give low contrast along the edges, and as there clearly is a significant amount of demagnetizing field along the edges, this supports the existence of SFM states.

7.3.2 Net magnetized SFM states

Several interesting observations can be made from the data represented in Figure 6.13. First of all, it is clear that the ensemble transitions into a macroscopically ordered state with a near-uniform magnetization. The net magnetization direction is parallel to the applied field, as expected of an SFM material. The final state can be considered to be a magnetized SFM state, similar to the magnetized state of a regular FM material.

Figure 6.13 shows the transition into this net magnetized SFM state at a field strength of approximately 7.5 mT. In the top part of the scan it clearly appears to have transitioned into its final, magnetized state. The sample-tip interaction was further investigated as seen in Figure 6.14.

It is clear that a transition of the ensemble into its net magnetized state occurs during the first scan. Such a transition can be argued from the fact that the last part of the scanned image is concurrent with the net magnetized state subsequently imaged. The tip is lifted and the ensemble is demonstrated to be in the net magnetized state. When re-lowering the tip, no further disturbing interaction can be observed. The lack of tip disturbance after the tip is lowered indicates that the new state is a stable state, which

the disturbance of the tip is not large enough to change.

From this transition dynamic it is reasonable to assume that there is an energy barrier between the stable initial state and the stable final state. At 5 mT, the extra disruption from the tip was not enough to push the ensemble over the threshold to the final state. However, at 7.5 mT, the state is closer to the threshold and the tip disruption is enough to push it over the barrier and into its final, net magnetized state.

7.3.3 Magnetic anomalies in net magnetized SFM states

As mentioned in Section 6.3.3, there seems to be some magnetic anomalies which can be removed by a strong field as indicated in Figure 6.15. The magnetic anomalies might be explained by magnetic particles in a vortex state, which requires a certain applied energy in order to overcome the energy threshold and become monodomain. Vortex states would disrupt the otherwise uniform magnetization of the SFM ensemble and produce field lines from the terminated SFM domains. An explanation with vortex states fits with the permanent disappearance of the anomalies once a strong enough field is applied. However, if the anomalies are solely due to vortex states, all anomalies should disappear at about the same applied field strength, as they share the same energy barrier. However, the observed anomalies indicate that the energy barriers can be widely different for separate anomalies.

Another hypothesis could involve a configuration of SFM domains of non-parallel magnetization that are pinned at an intersection. The pinning could be preserved by a high energy barrier. If one of the pinned SFM domains is more aligned with the applied field, an increase in field strength might provide the required energy to overcome the magnetization of the competing SFM domain and align both domains parallel to the applied field. However, this theory is, for now, purely speculation and has no experimental foundation yet.

The anomalies could also be explained by imperfections in the fabricated structures, inducing a strong magnetization anisotropy in certain individual magnets. Thus, the shape anisotropy barrier in each nanomagnet would have to be overcome by the applied field in order for a magnetization reversal to occur. A shape anisotropy in the individual disks would explain the permanent disappearance of the anomalies happening at different field strengths, as the degree of shape anisotropy can vary from disk to disk.

7.3.4 Remanent SFM magnetization

The net magnetized states discussed until now have been observed while subjected to an external magnetic field. However, under such an applied magnetic field, even paramagnetic materials are capable of exhibiting net magnetization, as they are magnetizable. The real test whether these structures are in a SFM magnetized state is to observe them under no applied external field. A SFM material, similar to a FM material, is expected to have some hysteresis, or remanent magnetization, in the absence of an applied field

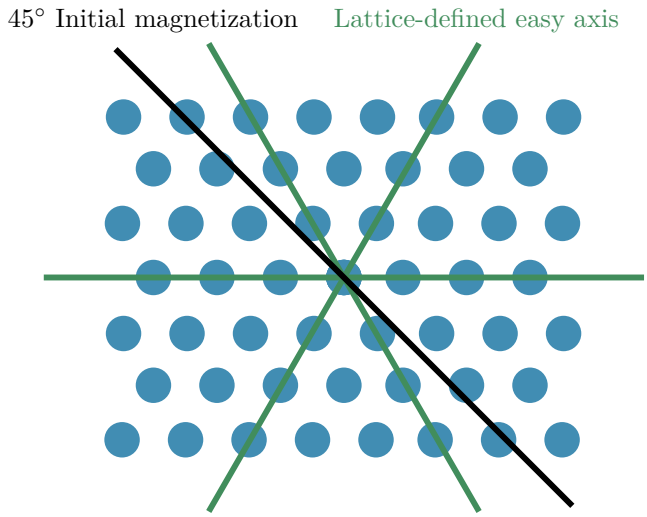

Figure 7.2: Illustration of lattice defined easy axes (green) in a trigonally stacked lattice. Also shown is the initial 45° magnetization direction (black). Note that the lattice presented here only represents a small portion of an ensemble lattice, which includes many more magnets.

(after an initial magnetization, naturally).

As mentioned in Section 6.3.4, there is a clear remanent magnetization in the observed structures. The remanent magnetization imaged in Figure 6.16 seems to relax to a horizontal direction once the field is removed. Such a change in magnetization direction might be related to the observation made in Section 6.1 where the SFM domains tend to lie along the dense axes of the ensemble. The explanation fits well with the observed result, as the horizontal axis is one of the three densely packed axes.

However, the initial 45° magnetization direction is closer to the 60° densely packed, lattice-defined easy axis, as illustrated in Figure 7.2. If the lattice stacking was the only factor determining the reorientation of the remanent magnetization, it would be expected to lie along this non-horizontal easy axis as there should be a smaller energy barrier for that reorientation (due to a suspected hard axis at the 30° direction). On the other hand, it is important to consider the finite size of the studied ensemble. The ensemble has a square shape and is terminated in a jagged fashion along two of its sides. The difference in ensemble termination might contribute to an *ensemble* shape anisotropy, which could favor a horizontal magnetization direction. Other contributions could also affect and induce such behavior, such as remanent magnetization in the experimental equipment or stray fields from other nearby materials or ensembles. The suspected EBL anisotropy that might be found in individual disks would also favor a horizontal magnetization. The true cause of the reorientation could be further investigated by creating a sample with in-plane rotated, similar structures.

7.3.5 Effect of ensemble parameters

The ensemble which has been studied the most is the trigonal lattice with 100 nm disk diameter and 30 nm spacing. This ensemble was one of the first studied structures that showed signs of a micromagnetic structure and has therefore been a prime candidate for the discussion of the behavior outlined in the previous sections.

From Figure 6.17, showing the behavior of several differently structured ensembles, it is clear that the ensembles exhibit qualitatively separate behavior, despite their parameters being closely related. These differences include the field strength necessary to completely magnetize the ensembles, the remanent magnetization microstructure and, notably, the magnetization direction altogether. The last observation, that the 150 nm diameter disk ensembles obtain a net remanent magnetization that is orthogonal to the other ensembles, is a quite surprising and interesting find. However, the behaviors of the ensembles with different size disks are expected to be qualitatively different, as the larger disks are expected to manifest vortex states, which would drastically alter the emergent ensemble properties.

Figure 6.18 can be used to identify the relative magnetic remanence and coercivity for the imaged structures. By noting the point at which the ensembles flip magnetization states, the relative coercivity can be established. Similarly, by examining the net magnetization of the state without an applied field, an ensemble's remanent magnetization can be estimated relative to the other ensembles. Interestingly, the smaller disks have a greater degree of remanent magnetization and a significantly larger coercivity. The larger coercivity in the smaller disks might be due to the fact that the larger disks exhibit vortex states, as the imaged sample (in this case) has not experienced strong applied fields. Vortex states would contribute to lowering the coercivity of the sample, as they do not provide a reinforcing, dipolar coupling along the net magnetization direction.

Figure 6.19 provides the same insight for the smaller ensembles. The imaged set of hexagonally bound ensembles reconfirmed the coercivity and remanent magnetization difference of the larger ones from Figure 6.18, but was otherwise not significantly different. The larger disk sizes imaged in Figure 6.19 behave quite different from the smaller ones. Again the lower coercivity in larger disk sizes can be explained by the prevalent existence of vortex states in larger disk diameters.

7.3.6 Magnetization rotation

During a change in magnetization direction, the structures imaged in Figure 6.20 seem to have a rotating magnetization. An in-plane rotation of the magnetization is a quite peculiar result, and attempts at recreating the results in simulations have been unsuccessful. At the present time, no plausible hypothesis to explain this phenomena has been formulated, and it might be a result worthy of further investigations.

7.3.7 Square lattices

The observations of square lattices support the discussion and assumptions relating to the trigonal lattices and the presence of SFM states. However, the main goal of the square lattices was to establish experimental evidence for the SAFM states, as evidenced as a possible state by the simulation runs. While there were many attempts to find examples of SAFM states in the square lattice ensembles, a clear indicator of such states proved elusive. An external magnetic field was applied both diagonally and orthogonally to the lattices, but the remanent state (nearly) always indicated a net magnetization, similar to an SFM net magnetization. If SAFM states were present, the net magnetization is expected to be drastically reduced, as a perfect SAFM state would produce zero net magnetization. The fact that SAFM states provides low contrast in MFM imaging (on a large scale) might explain the reduced magnetic contrast of the ensembles in both Figures 6.21 and 6.22, which is consistent with a hypothesized SAFM state.

There are many potential pit falls that may have caused the lacking observations of SAFM states. One likely candidate is the presence of vortex states, favoring a relaxed SFM state rather than SAFM. The presence of vortex states could be prevented if a sufficiently strong field is applied, which would annihilate the vortex states and favor relaxed monodomain states.

However, there were *some* indications of SAFM states, such as the image series provided in Figure 6.21. It is clear that the small contrast from the ensembles in the first MFM scan is followed by a significantly improved contrast on the second MFM scan. Between the two MFM scans there was an intermittent AFM scan. The change might indicate that the ensembles were in an unstable SAFM state, which was disturbed by the close proximity of the tip during the AFM scans and were pushed into a chaotic SFM state or a vortex riddled state.

7.3.8 Stacked ellipses

From the acquired MFM images in Figure 6.22 it is clear that the coercivity of the different ensembles varies quite a bit with the specific ensemble parameters. As expected, the coercivity is higher for ellipses of larger eccentricity. The coercivity also seems to correlate with the disk size, as the 100 nm disks have a higher coercivity than the 150 nm disks.

One other interesting note is the fact that it is possible to achieve a state that has a very small net magnetization, as seen in the 0 mT image following an applied field of 40 mT. The low-contrast state is quite interesting, as it either means that the quite eccentric ellipses in that ensemble either have a magnetization that breaks their uniaxial shape anisotropy, or the ensemble's disks have ordered themselves in an antiparallel fashion. As the ellipses in that ensemble are more elongated than the most of the fabricated ensembles, the supposition that they have a magnetization orthogonal to their uniaxial easy axis is not likely. This might indicate that the ensemble is in a SAFM state. Or it might just

be an ensemble containing vortex states, although this is unlikely due to the elongated shape reducing the overall size of the nanomagnets.

7.3.9 Challenges

As mentioned throughout the discussion, there are many sources of discrepancies that could explain the sometimes qualitatively different results between the simulations and the experimentally observed structures. This section will briefly detail some of the suspected main contributions to such discrepancies and the challenges they pose.

One obvious reason for simulation and experimental discrepancy is the existence of fabrication defects. As discussed in Section 6.2, there are defects in the fabrication, although these are quite small. Defects might introduce some anisotropy to each individual magnet which can cause discrepancies like the apparent magnetization rotation. Introducing similar imperfections to the simulated systems might help produce qualitatively similar results. Although the exact defects of the experimental system cannot be reproduced, some insight might be gained from simulating such an imperfect system.

Another fabrication imperfection might be that each nanomagnet has a slight shape anisotropy. As the EBL writes the disks in a horizontal fashion, the beam is expected to travel horizontally between writing most of the nanomagnets. The prevalence of horizontal beam traveling might introduce an instability in the beam that affects the writing of the disks and causes them to be a little elongated in the horizontal direction. The resulting, minuscule, anisotropy might be undetectable by SEM, simply because the anisotropy is so small. However, such anisotropy would perfectly explain the tendency for the trigonal lattices to lie along the horizontal direction rather than the non-horizontal easy axis, as discussed in Section 7.3.4. It is much harder to write a perfectly circular disk than any elliptical disk, as the circle is only a single, perfect instance of an elliptical shape. However, there are many methods that could be utilized in order to circumvent this shortcoming. For instance, structures could be rotated in-plane or slightly compensated along the suspected anisotropic direction. A slight anisotropy in individual disks could also be included in the simulations.

The existence of vortex states has been hypothesized to be a significant contribution to these discrepancies. In order to avoid uncertainty connected to possible vortex states, larger magnetic fields could be applied to decrease the chance of vortex states remaining in the sample. The vortex core would be pushed out of the magnet and be annihilated, thus the magnetization would be uniform given a sufficiently strong applied field. Fabricating smaller disks would also decrease the likelihood of vortex states.

It is not only the experimental results that should be evaluated while looking for discrepancies, the simulations themselves must also be considered carefully. One of the main difference might stem from the fact that the material parameters used in the simulation might not be true to the physical thin film. The thin film might have slightly different values in M_{S}, A_{exch}, or even anisotropy. In order to establish a true correspondence of the material parameters to the simulations, some calibration experiments could be performed.

For instance, the field required to push a vortex core out of bounds in a square piece of continuous film could be such a physically unmistakable experiment.

Another shortcoming of the simulations is the way the MFM image is acquired. In the real world, the tip will have a significant size and its own magnetic moment which will be interacting with the sample. The effect of tip-sample interaction has already been observed and can be seen in Figure 6.13. The experimental MFM is, unlike the simulated MFM, limited in resolution, so while the simulated MFM can pick up contrast from individual disks, the physical MFM is dependent on contrast across larger regions. However, in order to observe the low-contrast effect that the SAFM states are suspected to exhibit, a low-resolution can be advantageous, as it averages the field over some larger region where the SAFM state has a zero net magnetization.

Chapter 8

Summary and Conclusion

In this project work, the topic of supermagnetic behavior in ensembles of flat permalloy nanomagnets has been introduced and relevant theoretical background has been discussed. The system of interest has been investigated through two complimentary approaches. One approach included micromagnetic modeling of the ensembles utilizing GPU-accelerated software. The other approach consisted of MFM imaging and application of a magnetic field to manipulate and probe the behavior of physically fabricated ensembles. In addition to this, a method for designing complex EBL mask designs with large parameter spaces has been developed, implemented and used for fabrication purposes.

The results of the simulations were used to discover relevant material- and structure parameters. The relevant parameters include nanomagnet size, stacking geometry, magnet separation and ensemble size and bounding shape. Additionally, the effect of parameters such as an external field or different initialized states have been tested.

Both superferromagnetic and superantiferromagnetic stable states were found in the simulations. Trigonal lattices only exhibited stable SFM states. Simulated square lattice ensembles exhibited stable SFM and stable SAFM states. The behavior of these states were characterized in order to distinguish a physical manifestation of such states in the fabricated samples.

The results of the fabricated samples indicate stable SFM states for both trigonal and square lattices. The SAFM state found in simulations of square lattices has not been unambiguously identified, although some results might indicate the presence of such states. There are many potential explanations for the lack of a clear observarion of the SAFM state, such as imperfections in the fabrication process, disturbance from the magnetic MFM tip, or simply failure to interpret the system state as SAFM.

In conclusion, SFM states have been predicted by simulations and observed experimentally for nanofabricated ensembles. However, the predicted SAFM state of square lattice ensembles has not been sufficiently established in physical samples investigated by MFM. Despite the clear discrepancy between the obtained results from simulations and physical investigation, the thesis work has successfully given strong evidence for a

new, physically observed SFM state in large nanomagnetic ensembles. Additionally, it has opened the door to an exotic, physically realizable, switchable SFM/SAFM state, which is also fairly easy to fabricate.

If the challenges of fabricating and observing the SAFM state in square lattices can be overcome, a completely new material with this switching property could pave the way for future technological innovation. There is good reason to suspect that magnetically exotic materials, such as the ones discussed in this thesis, will play an important role in coming technological advancements.

8.1 Further work

Further work should aim to understand and explain the discrepancy between simulated results and observed physical results. Investigation of this discrepancy could be done by a thorough review of the assumptions made in the setup of the micromagnetic modeling. Also, careful attention to detail and a review of the MFM setup might reveal unknown uncertainties as the root cause of the discrepancy observed in the obtained results. Studying more examples, more physically fabricated ensembles that is, would undoubtedly prove insightful into the true behavior of the structures.

The effect of vortex states and their competition with monodomain states should be thoroughly analyzed and quantified, which could be done by performing similar analyses as Slöetjes et al. [33]. Additionally, even stronger applied magnetic fields are possible in the current experimental setup, which might eliminate vortex states.

There are many parameters that could be explored further in order to gain additional insight. Following are some parameters that were left out of this thesis due to time constraints. The temperature of the system could be changed, both in simulations and experimental observations. It would be particularly interesting to see how the SFM state behaves at higher temperatures, and how it might transition into a non-SFM state. High performance MFM tips could be utilized, instead of the standard tips supplied by the manufacturer. Better tips might help increase the resolution of the scans. The cryostat could be turned of while scanning in order to produce better images due to less vibration. Many of the structures could be made larger in order to investigate boundary effects. The structures could be rotated in-plane to limit the effect of non-symmetrical, systematic errors, such as the hypothesized EBL-induced anisotropy.

The auxiliary results mentioned in this thesis might offer other paths to further work. The effect of the shape anisotropy in the nanomagnets, as seen in the ellipsoidal disks, could be further quantified and might prove useful in order to catalyze a SAFM state. The spin ice system, presented in Appendix B, is a novel idea that has been modeled to exhibit very promising behavior within the field of unconventional computing, and there are many ways to further investigate these states with an MFM. The states could be subjected to strong fields at different angles, and the evolution could be captured by subsequent images. In order to automate the classification of the spin ice states, machine

learning techniques could be utilized.

In summary, this thesis has observed what could be the seed of many interesting further investigations, and there are promising results in several separate directions.

Bibliography

[1] D. C. Mattis. *History of Magnetism*, pages 1–38. Springer Berlin Heidelberg, Berlin, Heidelberg, 1981. ISBN 978-3-642-83238-3. doi: 10.1007/978-3-642-83238-3_1.

[2] S. D. Bader. Colloquium: Opportunities in nanomagnetism. *Reviews of Modern Physics*, 78(1):1–15, jan 2006. doi: 10.1103/revmodphys.78.1.

[3] A. Moser, K. Takano, D. T. Margulies, M. Albrecht, Y. Sonobe, Y. Ikeda, S. Sun, and E. E. Fullerton. Magnetic recording: advancing into the future. *Journal of Physics D: Applied Physics*, 35(19):R157, sep 2002.

[4] R. C. O'Handley. *Modern Magnetic Materials - Principles and Applications*. John Wiley and Sons ltd, 1999. ISBN 0471155667.

[5] P. Tartaj, M. Morales, S. Veintemillas-Verdaguer, T. González-Carreño, and C. J. Serna. The preparation of magnetic nanoparticles for applications in biomedicine. *Journal of Physics D: Applied Physics*, 36(13):R182, jun 2003.

[6] S. A. Wolf. Spintronics: A spin-based electronics vision for the future. *Science*, 294 (5546):1488–1495, nov 2001. doi: 10.1126/science.1065389.

[7] M. Johnson and R. H. Silsbee. Interfacial charge-spin coupling: Injection and detection of spin magnetization in metals. *Physical Review Letters*, 55(17):1790–1793, oct 1985. doi: 10.1103/physrevlett.55.1790.

[8] M. N. Baibich, J. M. Broto, A. Fert, F. Nguyen Van Dau, F. Petroff, P. Etienne, G. Creuzet, A. Friederich, and J. Chazelas. Giant Magnetoresistance of (001)Fe/(001)Cr Magnetic Superlattices. *Physical Review Letters*, 61(21):2472–2475, nov 1988. doi: 10.1103/physrevlett.61.2472.

[9] G. Binasch, P. Grünberg, F. Saurenbach, and W. Zinn. Enhanced magnetoresistance in layered magnetic structures with antiferromagnetic interlayer exchange. *Physical Review B*, 39(7):4828–4830, mar 1989. doi: 10.1103/physrevb.39.4828.

[10] S. Bedanta and W. Kleemann. Supermagnetism. *Journal of Physics D: Applied Physics*, 42(1), dec 2009. ISSN 00223727. doi: 10.1088/0022-3727/42/1/013001.

[11] H. Brune. Probing magnetism at the nanoscale. *Nature Nanotechnology*, 2(11): 674–675, nov 2007. doi: 10.1038/nnano.2007.359.

[12] D. Vasyukov, Y. Anahory, L. Embon, D. Halbertal, J. Cuppens, L. Neeman, A. Finkler, Y. Segev, Y. Myasoedov, M. L. Rappaport, M. E. Huber, and E. Zeldov. A scanning superconducting quantum interference device with single electron spin sensitivity. *Nature Nanotechnology*, 8(9):639–644, sep 2013. doi: 10.1038/nnano.2013.169.

[13] M. Lundstrom. APPLIED PHYSICS: Enhanced: Moore's law forever? *Science*, 299 (5604):210–211, jan 2003. doi: 10.1126/science.1079567.

[14] I. L. Markov. Limits on fundamental limits to computation. *Nature*, 512(7513): 147–154, aug 2014. doi: 10.1038/nature13570.

[15] N. Nagaosa and Y. Tokura. Topological properties and dynamics of magnetic skyrmions. *Nature Nanotechnology*, 8(12):899–911, dec 2013. doi: 10.1038/nnano.2013.243.

[16] M. Guidry. Author, 2017. doi: 10.1063/1.5016130.

[17] H. N. Miras, J. Y., D. Long, and L. Cronin. Engineering polyoxometalates with emergent properties. *Chemical Society Reviews*, 41(22):7403, aug 2012. doi: 10.1039/c2cs35190k.

[18] S. Bedanta, T. Eimüller, W. Kleemann, J. Rhensius, F. Stromberg, E. Amaladass, S. Cardoso, and P. P. Freitas. Overcoming the dipolar disorder in dense cofe nanoparticle ensembles: Superferromagnetism. *Phys. Rev. Lett.*, 98:176601, apr 2007. doi: 10.1103/PhysRevLett.98.176601.

[19] R. Lavrijsen, J. Lee, A. Fernández-Pacheco, D. C. M. C. Petit, R. Mansell, and R. P. Cowburn. Magnetic ratchet for three-dimensional spintronic memory and logic. *Nature*, 493(7434):647–650, jan 2013. doi: 10.1038/nature11733.

[20] H. H. Lee. *Micromagnetic Modelling of Thermally Induced Errors in Nanomagnetic Logic*. NTNU Master's thesis, 2018.

[21] K. Roy, D. Fan, X. Fong, Y. Kim, M. Sharad, S. Paul, S. Chatterjee, S. Bhunia, and S. Mukhopadhyay. Exploring spin transfer torque devices for unconventional computing. *IEEE Journal on Emerging and Selected Topics in Circuits and Systems*, 5(1):5–16, mar 2015. doi: 10.1109/jetcas.2015.2405171.

[22] Y. Nakamura, R. Suzuki, M. Umeno, S. Cho, N. Tanaka, and M. Ichikawa. Observation of the quantum-confinement effect in individual β-FeSi2 nanoislands epitaxially grown on si (111) surfaces using scanning tunneling spectroscopy. *Applied Physics Letters*, 89(12):123104, sep 2006. doi: 10.1063/1.2349842.

[23] S. Liang, R. Islam, D. J. Smith, P. A. Bennett, J. R. O'Brien, and B. Taylor. Magnetic iron silicide nanowires on Si(110). *Applied Physics Letters*, 88(11):113111, mar 2006. doi: 10.1063/1.2185610.

[24] K. Seo, S. Lee, Y. Jo, M. Jung, J. Kim, D. G. Churchill, and B. Kim. Room Temperature Ferromagnetism in Single-Crystalline Fe5Si3 Nanowires. *The Journal of Physical Chemistry C*, 113(17):6902–6905, apr 2009. doi: 10.1021/jp902010j.

[25] B. D. Terris and T. Thomson. Nanofabricated and self-assembled magnetic structures as data storage media. *Journal of Physics D: Applied Physics*, 38(12):R199, jun 2005.

[26] V. Håkonsen. *Self-Assembly of Magnetic Nanoparticles into Superstructures for Magnonics*. NTNU Master's thesis, 2015.

[27] J. K. Tripathi, G. Markovich, and I. Goldfarb. Self-ordered magnetic α-FeSi2 nanostripes on si(111). *Applied Physics Letters*, 102(25):251604, jun 2013. doi: 10.1063/1.4812239.

[28] Y. Shiroishi, K. Shiiki, I. Yuitoo, H. Tanabe, H. Fujiwara, and M. Kudo. Patterning effect on easy axis alignment in permalloy thin film. *IEEE Transactions on Magnetics*, 20(3):485–488, may 1984. doi: 10.1109/tmag.1984.1063116.

[29] R. M. H. New. Submicron patterning of thin cobalt films for magnetic storage. *Journal of Vacuum Science & Technology B: Microelectronics and Nanometer Structures*, 12(6):3196, nov 1994. doi: 10.1116/1.587499.

[30] H. Tanabe and M. Kitada. Effect of film thickness on the magnetic and electrical properties of permalloy magnetoresistive sensors. *Journal of the Japan Institute of Metals*, 55(1):98–104, apr 1991. doi: 10.2320/jinstmet1952.55.1_98.

[31] J. C. Wu, H. W. Huang, and T. Wu. Evolution of magnetization reversal on patterned magnetic elements. *IEEE Transactions on Magnetics*, 36(5):2978–2980, sep 2000. doi: 10.1109/20.908646.

[32] S. Bedanta, T. Seki, H. Iwama, T. Shima, and K. Takanashi. Superferromagnetism in dipolarly coupled l10 FePt nanodots with perpendicular magnetization. *Applied Physics Letters*, 107(15):152410, oct 2015. doi: 10.1063/1.4933381.

[33] S. D. Slöetjes, H. H. Urdahl, J. K. Grepstad, and E. Folven. Tailoring the magnetic order in a supermagnetic metamaterial. *AIP Advances*, 7(5):056325, mar 2017. doi: 10.1063/1.4978319.

[34] N. A. Spaldin. *Magnetic Materials: Fundamentals and Device Applications*. Number July. Cambridge University Press, 2009. ISBN 9780521885768.

[35] R. G. Piccioni. Special relativity and magnetism in an introductory physics course. *The Physics Teacher*, 45(3):152–156, mar 2007. doi: 10.1119/1.2709673.

[36] J. C. Maxwell. A dynamical theory of the electromagnetic field. *Philosophical Transactions of the Royal Society of London*, 155(0):459–512, jan 1865. doi: 10.1098/rstl.1865.0008.

[37] B. D. Cullity and C. D. Graham. *Introduction to Magnetic Materials*. Wiley-IEEE Press, 2008. ISBN 0471477419.

[38] R. Shankar. *Principles of Quantum Mechanics*. Plenum Press, 1994. ISBN 0306403978.

[39] R.C. O'Handley. *Modern Magnetic Materials - Principles and Applications*. John Wiley and Sons ltd., 1999. ISBN 0471155667.

[40] M. L. Néel. Propriétés magnétiques des ferrites: ferrimagnétisme et antiferromagnétisme. *Annales de Physique*, 12(3):137–198, apr 1948. doi: 10.1051/anphys/194812030137.

[41] H. Kronmüller and M. Fähnle. *Micromagnetism and the Microstructure of Ferromagnetic Solids (Cambridge Studies in Magnetism)*. Cambridge University Press, 2003. ISBN 0521331358.

[42] P. Zhou, Y. Qi, C. Yang, Z. Mei, A. Y., K. Liang, Z. Ma, Z. Xia, and T. Zhang. Magnetic anisotropy of epitaxial la2/3sr1/3mno3 thin films on SrTiO3 with different orientations. *AIP Advances*, 6(12):125044, dec 2016. doi: 10.1063/1.4972955.

[43] A. C. Mishra. Effect of composition on magnetic softness and magnetoimpedance of electrodeposited NiFe/Cu. *Indian Journal of Physics*, 88(4):367–373, nov 2013. doi: 10.1007/s12648-013-0423-0.

[44] K. A. Dill and S. Bromberg. *Molecular Driving Forces: Statistical Thermodynamics in Biology, Chemistry, Physics, and Nanoscience, 2nd Edition*. Garland Science, 2010. ISBN 0815344309.

[45] A. V. Svalov, I. R. Aseguinolaza, A. Garcia-Arribas, I. Orue, J. M. Barandiaran, J. Alonso, M. L. Fernández-Gubieda, and G. V. Kurlyandskaya. Structure and magnetic properties of thin permalloy films near the "transcritical" state. *IEEE Transactions on Magnetics*, 46(2):333–336, feb 2010. doi: 10.1109/tmag.2009.2032519.

[46] William Coffey. *The Langevin equation : with applications to stochastic problems in physics, chemistry, and electrical engineering*, volume v. 27 of *World Scientific series in contemporary chemical physics ;*. World Scientific, River Edge, NJ, 3rd ed. edition, 2012. ISBN 981-4355-67-4.

[47] H. H. Urdahl. *Exploring supermagnetism in patterned thin films of La0.7Sr0.3MnO3*. NTNU Master's thesis, 2016.

[48] A. Vansteenkiste, J. Leliaert, M. Dvornik, M. Helsen, F. Garcia-Sanchez, and B. Van Waeyenberge. The design and verification of MuMax3. *AIP Advances*, 4(10), oct 2014. ISSN 21583226. doi: 10.1063/1.4899186.

[49] A. Aharoni. *Introduction to the Theory of Ferromagnetism (The International Series of Monographs on Physics)*. Oxford University Press, 1996. ISBN 0198517912.

[50] W. F. Brown. *Micromagnetics*. Krieger Pub Co, 1978. ISBN 0882756656.

[51] L. D. Landau and E. Lifshitz. On the theory of the dispersion of magnetic permeability in ferromagnetic bodies. *Phys. Z. Sowjet.*, 8:153, 1935.

[52] J.C. Mallinson. Damped gyromagnetic switching. *IEEE Transactions on Magnetics*, 36(4):1976–1981, jul 2000. doi: 10.1109/20.875251.

[53] Y. Nakatani, Y. Uesaka, and N. Hayashi. Direct Solution of the Landau-Lifshitz-Gilbert Equation for Micromagnetics. *Japanese Journal of Applied Physics*, 28(12R): 2485, dec 1989.

[54] C. Serpico, I. D. Mayergoyz, and G. Bertotti. Numerical technique for integration of the landau–lifshitz equation. *Journal of Applied Physics*, 89(11):6991–6993, jun 2001. doi: 10.1063/1.1358818.

[55] C. Serpico, I. D. Mayergoyz, and G. Bertotti. Analytical solutions of Landau–Lifshitz equation for precessional switching. *Journal of Applied Physics*, 93(10):6909–6911, may 2003. doi: 10.1063/1.1557278.

[56] H. D. Arnold and G. W. Elmen. Permalloy, a new magnetic material of very high permeability. *Bell System Technical Journal*, 2(3):101–111, jul 1923. doi: 10.1002/j.1538-7305.1923.tb03595.x.

Appendix A

EBL mask design process

Throughout the work in this thesis, the complexity of the EBL mask designs have required the development of the following outlined method. The design process involves the use of an open-source Python package, gdsCAD. The gdsCAD package provides a programming framework for creating and manipulating the elements of the GDSII file format.

In the GDSII file format there is a hierarchy of structures, including paths, shapes, cells and layouts. The fundamental building block is the versatile cell object. A cell may in turn contain other cells, cell references, and can be everything from constituent parts of a complex design to a simple geometric object.

In order to populate the cells with geometric structures, paths and shapes are used. A path is exactly what it seems like, a sequence of lines that may be the boundary of a constructed geometric structure. Shapes are instances of simple geometric shapes, such as circles, rectangles, or disks, and may be defined according to typical parameters and placed in cells.

The all-encompassing layer of the hierarchy is the layout. A layout will hold all cells and constituent parts and is what we refer to as the design.

There are plenty of ways to manipulate the objects through both simple and more complicated functionality. Any wanted design may thus utilize the different elements of the GDSII standard and be assembled to any program-specified structures. This provides great flexibility in terms of generated structures as a function of a parameter space, and may help parametrize complex design patterns over several iterations without the need to redesign everything in a layout editor.

The following section will provide an introduction to the procedure by illustrating an introductory sample. This tutorial was originally intended for the other members of the research group who would benefit from this approach. Following that section there is a section containing common utility functions specifically written for the purpose of stacking and manipulating lattices of simple objects. Finally, the last section will illustrate how the second, and the most studied sample in this thesis, was designed.

A.1 Introduction by example

This code snippet was originally intended as a tutorial for the research group, and is therefore written in a non-formal language. It is a very simple example to illustrate how easy one can get started and also underline the power of this process.

```
# First, let's import the python packages we need:
get_ipython().magic('matplotlib inline')
from gdsCAD.gdsCAD import *
import numpy as np
import matplotlib.pyplot as plt
import math
import gdsUtils as gu # Self-written utility functions

# Now, let us create a Disk shape that we can later stack in our lattice.
radius = .2
disk = shapes.Disk((0,0), radius)
disk.show()


# Great. The next element we will look at is the Cell.
# The Cell is the most versatile component used in the gdsCAD package,
# and we should try to structure our code around the use of them.
# Cells can contain references to other cells, and thus they are the most
    practical building block of our design.
# Cells must have a name, and we provide one when we create them.
# After creation, other objects can be added to the cell, and will be
    incorporated as references.
#
# Let us add our disk to a cell building block.

diskcell = core.Cell('diskcell') # Create the disk cell
diskcell.add(disk) # Add the disk shape
diskcell.show()


# The advantage is not instantly apparent, but it will be much more
    practical to have our disk represented as a cell later on.
# Let's try to stack our newly created cell in an array, using an inbuilt
    function.

trigcellarray = core.CellArray(diskcell, 10, 10, ((1,0), (math.cos(math.pi
    /3),math.sin(math.pi/3)) ))

# We can't view this CellArray-element directly, as it doesn't have it's
```

```
    own show()-function, and we need to add it to a cell first:
trigarray = core.Cell('TRIGARRAY')
trigarray.add(trigcellarray)
trigarray.show()


# If this is all we wanted for our design, we could create a layout and add the cell.
# If we wanted many other types of cells, we could create a top cell and add all other cells
# to that before adding the top cell to the layout.
# There are many ways to play around with and create structures. The most important part is to keep track of everything.
# Let's add our design to a layout and save to a .gds-file.

# Add more designs into top cell
topcell = core.Cell('TOPCELL')
topcell.add(trigarray)
topcell.add(trigarray, origin=(20,0))
topcell.add(trigarray, origin=(40,0), rotation=60)

# Layout
layout = core.Layout('TRIGLAYOUT')
layout.add(topcell)
layout.save('Triglayout.gds')
layout.show()
```

A.2 Common utility functions

The following code defines several useful utility functions specifically written for creating and manipulating stacks and lattices of nanomagnets. One of the great versatile aspects of the functions is that anything may be stacked. This includes circles of different sizes and spacings, but also other geometric shapes such as an ellipse or even hexagonal nanoparticles.

```
from gdsCAD.gdsCAD import *
import numpy as np
import matplotlib.pyplot as plt
from matplotlib.collections import PatchCollection
import math


def squarestack(base_element, a, xrange, yrange, the_origin=(0, 0)):
    # Create lattice basis as a cell
```

```
    squarebase = core.Cell('SQUAREBASE')
    squarebase.add(base_element)

    # Calculate how many cells fit in xrange, yrange
    n_cell_x = round(xrange / a)
    n_cell_y = round(yrange / a)

    # Create CellArray
    square_array = core.CellArray(squarebase, n_cell_x, n_cell_y, (a,a),
    origin=the_origin )
    # Put CellArray in Cell
    square_stack = core.Cell('SQUARESTACK')
    square_stack.add(square_array)

    return square_stack


# General stacking function
def anglestack(base_cell, pitch, angle, fieldsize, shape='square'):
    # Create lattice basis as a cell
    stack = core.Cell('STACKpitch{}deg{}{}'.format(pitch, angle, shape))

    # Create basis vectors
    anglerad = angle*math.pi/180
    basevec0 = (pitch, 0) # Horizontal basis vector
    basevec1 = (math.cos(anglerad)*pitch, math.sin(anglerad)*pitch)

    # Set field width and height
    if isinstance(fieldsize, tuple):
        fieldwidth = fieldsize[0]
        fieldheight = fieldsize[1]
    else:
        fieldwidth = fieldsize
        fieldheight = fieldsize

    if shape=='natural':
        nx = int(fieldwidth/basevec0[0])
        ny = int(fieldheight/basevec1[1])
        stack.add(core.CellArray(base_cell, nx,ny, (basevec0, basevec1)))
    elif shape=='square':
        unitcell = core.Cell('UNITCELLpitch{}deg{}'.format(pitch,angle))
        unitcell.add(base_cell)
        unitcell.add(base_cell, origin=basevec1)

        nx = int(fieldwidth/basevec0[0])
```

```
54          ny = int(fieldheight/basevec1[1])
55          stack.add(core.CellArray(unitcell, nx,ny, (2*math.cos(anglerad)*
        pitch,2*pitch*math.sin(anglerad))))
56      elif shape=='hex':
57          print("COMING SOON")
58      else:
59          print("ERROR! No such fieldshape.")
60
61      return stack
62
63
64  def trigstack(base_element, a, xrange, yrange, the_origin=(0, 0)):
65      # Create lattice basis of elements as a cell
66      trigbase = core.Cell('TRIGBASE')
67      trigbase.add(base_element)
68      # trigbase.add(utils.translate(base_element, (a / 2, a * np.sqrt(3) /
        2)))
69      trigbase.add(base_element, origin=(a / 2, a * np.sqrt(3) / 2))
70
71      # Calculate how many cells fit in xrange, yrange
72      n_cell_x = round(xrange / a)
73      n_cell_y = round(yrange / (np.sqrt(3) * a))
74
75      # Create CellArray
76      trig_array = core.CellArray(trigbase, n_cell_x, n_cell_y, (a, a * np.
        sqrt(3)), origin=the_origin)
77      # Put CellArray in Cell
78      trig_stack = core.Cell('TRIGSTACK')
79      trig_stack.add(trig_array)
80
81      return trig_stack
82
83
84  # hexagonally bound trig stacked
85  def trigstack_hexbound(base_element, a, xrange, yrange, the_origin=(0, 0)):
86
87      # Calculate how many cells fit in xrange, yrange
88      n_cell_x = int(round(xrange / (2*a)))
89      n_cell_y = int(round(yrange / (2*a)))
90
91      basecell = core.Cell('BASECELL')
92      basecell.add(base_element)
93      arraycell = core.Cell('ARRAY')
94      for y in range(n_cell_y+1):
95          offset = 0.0
```

```
96          if y%2!=0:
97              offset = a/2
98          for x in range(n_cell_x - int(math.ceil(y/2))+1):
99              arraycell.add(basecell, origin=(int(round(x*a+offset+the_origin
    [0]+a*n_cell_x)),\
100                                             int(round(y*math.sqrt(3)*a/2)+
    the_origin[1]+a*n_cell_y)))
101             arraycell.add(basecell, origin=(int(round(-x*a-offset+
    the_origin[0]+a*n_cell_x)),\
102                                             int(round(y*math.sqrt(3)*a/2)+
    the_origin[1]+a*n_cell_y)))
103             arraycell.add(basecell, origin=(int(round(x*a+offset+the_origin
    [0]+a*n_cell_x)),\
104                                             int(round(-y*math.sqrt(3)*a/2)+
    the_origin[1]+a*n_cell_y)))
105             arraycell.add(basecell, origin=(int(round(-x*a-offset+
    the_origin[0]+a*n_cell_x)),\
106                                             int(round(-y*math.sqrt(3)*a/2)+
    the_origin[1]+a*n_cell_y)))
107
108     return arraycell
109
110 def savecellaspng(cell, filename='test.png', xrange=None, yrange=None,
    pixels=None):
111     patches = cell.artist()
112     fig, ax = plt.subplots()
113
114     collection = PatchCollection(patches)
115     collection.set_facecolor('k')
116     ax.add_collection(collection)
117
118     # Set up correct area
119     box = cell.bounding_box
120     if xrange is not None:
121         xdiff = xrange - (box[1][0]-box[0][0])
122         xlims = (box[0][0]-xdiff/2, box[1][0]+xdiff/2)
123         ax.set_xlim(xlims)
124     if yrange is not None:
125         ydiff = yrange - (box[1][1]-box[0][1])
126         ylims = (box[0][1]-ydiff/2, box[1][1]+ydiff/2)
127         ax.set_ylim(ylims)
128
129     plt.axis('off')
130     ax.axis('off')
131
```

```
132     # TODO: This feature does not work correctly, wrong DPI, entire
        handling of fig should be redesigned
133     # Calculate DPI if certain pixelrange is desired:
134     if pixels is not None and xrange is not None and yrange is not None:
135         dpi = fig.get_dpi()
136         fig.set_size_inches(pixels[0] / float(dpi), pixels[1] / float(dpi))
137 
138     ax.set_aspect('equal')
139     fig.savefig(filename, bbox_inches='tight')  # For some reason this is
        required to get correct aspect ratio
140     extent = ax.get_window_extent().transformed(fig.dpi_scale_trans.
        inverted())
141     fig.savefig(filename, bbox_inches=extent)
142 
143 
144 def showblackcell(cell,xrange=None,yrange=None):
145     patches = cell.artist()
146     fig, ax = plt.subplots()
147 
148     collection = PatchCollection(patches)
149     collection.set_facecolor('k')
150     ax.add_collection(collection)
151 
152     # Set up correct area
153     box = cell.bounding_box
154     if xrange is None:
155         xlims = (box[0][0], box[1][0])
156     else:
157         xdiff = xrange - (box[1][0]-box[0][0])
158         xlims = (box[0][0]-xdiff/2, box[1][0]+xdiff/2)
159     if yrange is None:
160         ylims = (box[0][1], box[1][1])
161     else:
162         ydiff = yrange - (box[1][1]-box[0][1])
163         ylims = (box[0][1]-ydiff/2, box[1][1]+ydiff/2)
164     ax.set_xlim(xlims)
165     ax.set_ylim(ylims)
166 
167     ax.set_aspect('equal')
168     #plt.axis('off')
169     plt.show()
```

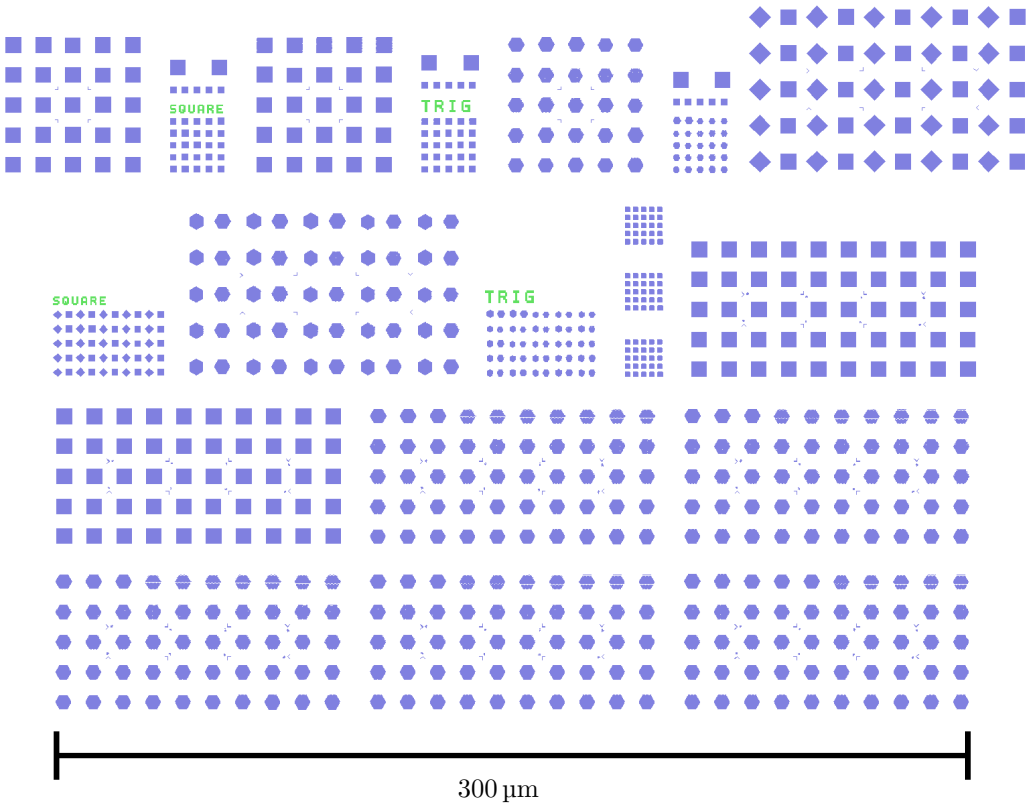

Figure A.1: Layout of designed EBL mask. The layout demonstrates the immense complexity possible with this method, although it represents only a small subset of the designed masks. Each blue field is an ensemble structure with unique parameters.

A.3 Implemented mask design

The second sample that was created for this thesis, and which coincidentally is the most studied sample, is defined in the following script. Other samples were also made, but only this design is included here. Best coding practices are *not* applied, as the final layout of the design was not finalized but formed throughout coding of the script. Thus, some excerpts might look, and indeed are, inefficient. However, it is possible to argue that this is one of the strengths of this approach as it still achieves a design prototype in a limited amount of time spent designing.

An example overview of the design is provided in Figure A.1.

```
1 get_ipython().magic('matplotlib inline')
2 from gdsCAD.gdsCAD import *
3 import numpy as np
4 import matplotlib.pyplot as plt
5 import math
```

```
import gdsUtils as gu

#Global parameters
patternpadding = 10000
allstructs = []  # Array used to hold and arrange all structures along the horizontal direction

# circular disks, 5um fields
diameters = np.linspace(50, 250, 5)
spacings = np.linspace(30, 50, 5)
xfield = 5000
yfield = xfield
parameterpadding = xfield
trigstacks = core.Cell('TRIGCIRC5UM')
squarestacks = core.Cell('SQAURECIRC5UM')
trigstacks_hexbound = core.Cell('TRIGCIRC5UMHEX')
trigrots = core.Cell('TRIG5UMROT')
squarerots = core.Cell('SQUARE5UMROT')
x, y = 0, 0  # ORIGIN coordinates
xrot, yrot = 0, 0
for diameter in diameters:
    disk = shapes.Disk((diameter/2, diameter/2), diameter/2)
    x = 0
    xrot = 0
    for spacing in spacings:
        squarestacks.add(gu.squarestack(disk, diameter+spacing, xfield, yfield, (x,y)))
        trigstacks.add(gu.trigstack(disk, diameter+spacing, xfield, yfield, (x,y)))
        trigstacks_hexbound.add(gu.trigstack_hexbound(disk, diameter+spacing, xfield, yfield, (x,y)))

        # Create fields with rotated neigbhours
        squarestacked = core.Cell('SQUAREROTd{}spac{}'.format(diameter, spacing))
        squarestacked.add(gu.squarestack(disk, diameter+spacing, xfield, yfield))
        squarerots.add(squarestacked, rotation = 45, origin = (xrot,yrot))
        squarerots.add(squarestacked, rotation = 0, origin = (xrot+math.sqrt(2)*xfield, yrot+(math.sqrt(2)-1)*xfield/2))
        trigstacked = core.Cell('TRIGROTd{}spac{}'.format(diameter,spacing))
        trigstacked.add(gu.trigstack_hexbound(disk, diameter+spacing, xfield, yfield))
        trigrots.add(trigstacked, rotation = 30, origin = (xrot,yrot))
```

```
42          trigrots.add(trigstacked, rotation = 0, origin = (xrot+math.sqrt(2)
        *xfield, yrot+(math.sqrt(2)-1)*xfield/2))
43
44          x += parameterpadding + xfield
45          xrot += parameterpadding + 2*math.sqrt(2)*xfield
46      y += parameterpadding + yfield
47      yrot += parameterpadding + math.sqrt(2)*yfield
48  #squarerots.add(shapes.Label('SQUARE', 10000, (0,(squarerots.bounding_box
        [1][1]+1000))))
49  #trigrots.add(shapes.Label('TRIG', 10000, (0,(trigrots.bounding_box
        [1][1]+1000))))
50  # Create L-markers within parameterlattices for orientation
51  lmark_length = 1000
52  lmark_placement = 7/18 # Fraction into lattice
53  lmark = core.Cell('LMARK')
54  lmark.add(core.Path([(-lmark_length,0), (0,0), (0,-lmark_length)], width
        =20, pathtype=1))
55  box = squarestacks.bounding_box
56  squarestacks.add(lmark, origin=(box[1][0]*lmark_placement,box[1][1]*
        lmark_placement))
57  squarestacks.add(lmark, origin=(box[1][0]*(1-lmark_placement),box[1][1]*
        lmark_placement), rotation=90)
58  squarestacks.add(lmark, origin=(box[1][0]*(1-lmark_placement),box[1][1]*(1-
        lmark_placement)), rotation=180)
59  squarestacks.add(lmark, origin=(box[1][0]*lmark_placement,box[1][1]*(1-
        lmark_placement)), rotation = 270)
60  box = trigstacks.bounding_box
61  trigstacks.add(lmark, origin=(box[1][0]*lmark_placement,box[1][1]*
        lmark_placement))
62  trigstacks.add(lmark, origin=(box[1][0]*(1-lmark_placement),box[1][1]*
        lmark_placement), rotation=90)
63  trigstacks.add(lmark, origin=(box[1][0]*(1-lmark_placement),box[1][1]*(1-
        lmark_placement)), rotation=180)
64  trigstacks.add(lmark, origin=(box[1][0]*lmark_placement,box[1][1]*(1-
        lmark_placement)), rotation = 270)
65  box = trigstacks_hexbound.bounding_box
66  trigstacks_hexbound.add(lmark, origin=(box[1][0]*lmark_placement,box[1][1]*
        lmark_placement))
67  trigstacks_hexbound.add(lmark, origin=(box[1][0]*(1-lmark_placement),box
        [1][1]*lmark_placement), rotation=90)
68  trigstacks_hexbound.add(lmark, origin=(box[1][0]*(1-lmark_placement),box
        [1][1]*(1-lmark_placement)), rotation=180)
69  trigstacks_hexbound.add(lmark, origin=(box[1][0]*lmark_placement,box
        [1][1]*(1-lmark_placement)), rotation = 270)
70  lmark45 = 7/38
```

```
box = squarerots.bounding_box
squarerots.add(lmark, origin=(box[1][0]*lmark_placement,box[1][1]*
    lmark_placement))
squarerots.add(lmark, origin=(box[1][0]*(1-lmark_placement),box[1][1]*
    lmark_placement), rotation=90)
squarerots.add(lmark, origin=(box[1][0]*(1-lmark_placement),box[1][1]*(1-
    lmark_placement)), rotation=180)
squarerots.add(lmark, origin=(box[1][0]*lmark_placement,box[1][1]*(1-
    lmark_placement)), rotation = 270)
squarerots.add(lmark, origin=(box[1][0]*lmark45,box[1][1]*lmark_placement),
     rotation=45)
squarerots.add(lmark, origin=(box[1][0]*(1-lmark45),box[1][1]*
    lmark_placement), rotation=135)
squarerots.add(lmark, origin=(box[1][0]*(1-lmark45),box[1][1]*(1-
    lmark_placement)), rotation=225)
squarerots.add(lmark, origin=(box[1][0]*lmark45,box[1][1]*(1-
    lmark_placement)), rotation = 315)
box = trigrots.bounding_box
trigrots.add(lmark, origin=(box[1][0]*lmark_placement,box[1][1]*
    lmark_placement))
trigrots.add(lmark, origin=(box[1][0]*(1-lmark_placement),box[1][1]*
    lmark_placement), rotation=90)
trigrots.add(lmark, origin=(box[1][0]*(1-lmark_placement),box[1][1]*(1-
    lmark_placement)), rotation=180)
trigrots.add(lmark, origin=(box[1][0]*lmark_placement,box[1][1]*(1-
    lmark_placement)), rotation = 270)
trigrots.add(lmark, origin=(box[1][0]*lmark45,box[1][1]*lmark_placement),
    rotation=45)
trigrots.add(lmark, origin=(box[1][0]*(1-lmark45),box[1][1]*lmark_placement
    ), rotation=135)
trigrots.add(lmark, origin=(box[1][0]*(1-lmark45),box[1][1]*(1-
    lmark_placement)), rotation=225)
trigrots.add(lmark, origin=(box[1][0]*lmark45,box[1][1]*(1-lmark_placement)
    ), rotation = 315)


# circular disks, 2um fields
xfield = 2000
yfield = xfield
parameterpadding = xfield
trigstacks_small = core.Cell('TRIGCIRC2UM')
squarestacks_small = core.Cell('SQAURECIRC2UM')
trigstacks_hexbound_small = core.Cell('TRIGCIRC2UMHEX')
trigrots_small = core.Cell('TRIG2UMROT')
squarerots_small = core.Cell('SQUARE2UMROT')
```

```
x, y = 0, 0  # ORIGIN coordinates
yrot = 0.0
for diameter in diameters:
    disk = shapes.Disk((diameter/2, diameter/2), diameter/2)
    x = 0
    xrot = 0.0
    for spacing in spacings:
        trigstacks_small.add(gu.trigstack(disk, diameter+spacing, xfield, yfield, (x,y)))
        squarestacks_small.add(gu.squarestack(disk, diameter+spacing, xfield, yfield, (x,y)))
        trigstacks_hexbound_small.add(gu.trigstack_hexbound(disk, diameter+spacing, xfield, yfield, (x,y)))

        # Create fields with rotated neigbhours
        squarestacked = core.Cell('SQUAREROTd{}spac{}'.format(diameter, spacing))
        squarestacked.add(gu.squarestack(disk, diameter+spacing, xfield, yfield))
        squarerots_small.add(squarestacked, rotation = 45, origin = (xrot, yrot))
        squarerots_small.add(squarestacked, rotation = 0, origin = (xrot+math.sqrt(2)*xfield, yrot+(math.sqrt(2)-1)*xfield/2))
        trigstacked = core.Cell('TRIGROTd{}spac{}'.format(diameter,spacing))
        trigstacked.add(gu.trigstack_hexbound(disk, diameter+spacing, xfield, yfield))
        trigrots_small.add(trigstacked, rotation = 30, origin = (xrot,yrot))
        trigrots_small.add(trigstacked, rotation = 0, origin = (xrot+math.sqrt(2)*xfield, yrot+(math.sqrt(2)-1)*xfield/2))

        x += parameterpadding + xfield
        xrot += parameterpadding + 2*math.sqrt(2)*xfield
    y += parameterpadding + yfield
    yrot += parameterpadding + math.sqrt(2)*yfield
# Add labels above small fields
box = trigstacks_small.bounding_box
text = shapes.Label('TRIG', 5000, (box[0][0], box[1][1]+1000), layer=2)
trigstacks_small.add(text)
box = trigrots_small.bounding_box
text = shapes.Label('TRIG', 5000, (box[0][0], box[1][1]+1000), layer=2)
trigrots_small.add(text)
box = squarestacks_small.bounding_box
text = shapes.Label('SQUARE', 3500, (box[0][0], box[1][1]+1000), layer=2)
```

```
squarestacks_small.add(text)
box = squarerots_small.bounding_box
text = shapes.Label('SQUARE', 3500, (box[0][0], box[1][1]+1000), layer=2)
squarerots_small.add(text)

# Add continous films above small fields
largefields = 5000
contfilms = core.Cell('CONTFILMS')
rectshape = shapes.Rectangle((0,0),(largefields,largefields))
rectangle = core.Cell('RECTANGLE')
rectangle.add(rectshape)
rectshape_small = shapes.Rectangle((0,0),(xfield,yfield))
rectangle_small = core.Cell('RECTANGLE_SMALL')
rectangle_small.add(rectshape_small)
contfilms.add(rectangle_small)
contfilms.add(rectangle_small, origin=(2*xfield,0))
contfilms.add(rectangle_small, origin=(4*xfield,0))
contfilms.add(rectangle_small, origin=(6*xfield,0))
contfilms.add(rectangle_small, origin=(8*xfield,0))
contfilms.add(rectangle, origin=(0,3*xfield))
contfilms.add(rectangle, origin=(7*xfield,3*xfield))
box = trigstacks_small.bounding_box
trigstacks_small.add(contfilms, origin=(0,box[1][1]+xfield*2))
box = squarestacks_small.bounding_box
squarestacks_small.add(contfilms, origin=(0,box[1][1]+xfield*2))
box = trigstacks_hexbound_small.bounding_box
trigstacks_hexbound_small.add(contfilms, origin=(0,box[1][1]+xfield*2))

# Define spin ice lattice
widths = np.linspace(80, 60, 5)
lengths = np.linspace(220, 180, 5)
lattice = 320
spinicetop = core.Cell('SPINICETOP')
y = 0.0
for width in widths:
    x = 0.0
    for length in lengths:
        spinice = core.Cell('SPINICEw{}len{}'.format(width, length))
        vertbase = core.Cell('VERTBOXw{}len{}'.format(width, length))
        horizbase = core.Cell('HORIZBOXw{}len{}'.format(width, length))

        vertbase.add(shapes.Rectangle((0,0),(width, length)))
        horizbase.add(shapes.Rectangle((0,0),(length, width)))
        vertarray = core.CellArray(vertbase, 5,4, (lattice,lattice), origin
    =(0,(lattice-width-length)/2+width))
```

```
178         horizarray = core.CellArray(horizbase, 4,5, (lattice,lattice),
        origin=((lattice-width-length)/2+width,0))
179
180         spinice.add(vertarray)
181         spinice.add(horizarray)
182         spinicetop.add(spinice, origin=(x,y))
183         x += spinice.bounding_box[1][0]*2
184     y+= spinice.bounding_box[1][1]*2
185
186 trippelspinice = core.Cell('3xSPINICE')
187 trippelspinice.add(spinicetop)
188 trippelspinice.add(spinicetop, origin=(0, trippelspinice.bounding_box
        [1][1]+patternpadding))
189 trippelspinice.add(spinicetop, origin=(0, trippelspinice.bounding_box
        [1][1]+patternpadding))
190
191 tc = core.Cell('TOP')
192 tc.add(spinicetop)
193 layout = core.Layout('LAYOUT')
194 layout.add(tc)
195 layout.save('spinice.gds')
196
197 # Add things to allstructs and add to layout
198 layout = core.Layout('LAYOUT', unit=1e-09, precision=0.01e-09)
199 top = core.Cell('TOP')
200 posx = 0.0
201 patternpadding = 10000
202 allstructs = ([squarestacks, squarestacks_small,
203                   trigstacks, trigstacks_small,
204                   trigstacks_hexbound, trigstacks_hexbound_small,
205                   squarerots, squarerots_small,
206                   trigrots, trigrots_small,
207                   trippelspinice
208                  ])
209
210 # Ellipsoids, 5um fields
211 diameters = np.linspace(50, 250, 5)
212 spacing = 30
213 minmax_radius_frac = np.linspace(1, 0.55, 10)
214 xfield = 5000
215 yfield = xfield
216 parameterpadding = xfield
217 squarestacks_ellipse = core.Cell('SQAUREELLIPS5UM')
218 squarestacks_ellipse45 = core.Cell('SQAUREELLIPS5UM45DEG')
219 trigstacks_ellipse = core.Cell('TRIGELLIPS5UM')
```

```
220 trigstacks_ellipse30 = core.Cell('TRIGELLIPS5UM30DEG')
221 trigstacks_ellipse45 = core.Cell('TRIGELLIPS5UM45DEG')
222 x, y = 0, 0  # ORIGIN coordinates
223 for diameter in diameters:
224     x = 0
225     for radius_frac in minmax_radius_frac:
226         ellipse = shapes.Ellipse((diameter/2, diameter/2), diameter/2,
    diameter/2*radius_frac)
227         squarestacks_ellipse.add(gu.squarestack(ellipse, diameter+spacing,
    xfield, yfield, (x,y)))
228         squarestacks_ellipse45.add(gu.squarestack(utils.rotate(ellipse,45),
     diameter+spacing, xfield, yfield, (x,y)))
229         trigstacks_ellipse.add(gu.trigstack_hexbound(ellipse, diameter+
    spacing, xfield, yfield, (x,y)))
230         trigstacks_ellipse30.add(gu.trigstack_hexbound(utils.rotate(ellipse
    ,30), diameter+spacing, xfield, yfield, (x,y)))
231         trigstacks_ellipse45.add(gu.trigstack_hexbound(utils.rotate(ellipse
    ,45), diameter+spacing, xfield, yfield, (x,y)))
232
233
234         x += parameterpadding + xfield
235     y += parameterpadding + yfield
236 ellipsestructs = [squarestacks_ellipse,squarestacks_ellipse45,
    trigstacks_ellipse,trigstacks_ellipse30,trigstacks_ellipse45]
237 lmark_hplacement = 15/38
238 lmark_vplacement = 7/18
239 lmark_hplacement45 = 7/38
240 structnum = 0
241 #allstructs = []
242 box = ellipsestructs[0].bounding_box
243 for s in ellipsestructs:
244     lmarknum = core.Cell('LMARKNUM{}'.format(structnum))
245     lmarknum.add(lmark)
246     lmarknum.add(shapes.Label('{}'.format(structnum), 750, (lmark.
    bounding_box[1][0]+500),0))
247     s.add(lmarknum, origin=(box[1][0]*lmark_hplacement,box[1][1]*
    lmark_vplacement))
248     s.add(lmarknum, origin=(box[1][0]*(1-lmark_hplacement),box[1][1]*
    lmark_vplacement), rotation=90)
249     s.add(lmarknum, origin=(box[1][0]*(1-lmark_hplacement),box[1][1]*(1-
    lmark_vplacement)), rotation=180)
250     s.add(lmarknum, origin=(box[1][0]*lmark_hplacement,box[1][1]*(1-
    lmark_vplacement)), rotation = 270)
251     s.add(lmarknum, origin=(box[1][0]*lmark_hplacement45,box[1][1]*
    lmark_vplacement), rotation=45)
```

```
252     s.add(lmarknum, origin=(box[1][0]*(1-lmark_hplacement45),box[1][1]*
        lmark_vplacement), rotation=135)
253     s.add(lmarknum, origin=(box[1][0]*(1-lmark_hplacement45),box[1][1]*(1-
        lmark_vplacement)), rotation=225)
254     s.add(lmarknum, origin=(box[1][0]*lmark_hplacement45,box[1][1]*(1-
        lmark_vplacement)), rotation = 315)
255     structnum += 1
256     allstructs.append(s)
257
258 posx = 0.0
259 for structure in allstructs:
260     print("Adding structure")
261     top.add(structure, origin=(posx,0))
262     print("Finding new box")
263     posx += structure.bounding_box[1][0]+patternpadding
264
265 layout.add(top)
266
267 layout.save('layout.gds')
268
269 posx=0.0
270 lay = core.Layout('LAY', unit=1e-9)
271 tc = core.Cell('TOPCELL')
272 for structure in allstructs:
273     print("Adding structure")
274     tc.add(structure, origin=(posx,0))
275     print("Finding box")
276     posx = tc.bounding_box[1][0]+patternpadding
277 lay.add(tc)
278 print("Saving")
279 lay.save('lay.gds')
```

Appendix B

Spin ice systems

This appendix chapter will treat a topic not directly related to supermagnetism, instead it will consider applications of ensembles of nanomagnets. Specifically, it will discuss the so-called spin ice systems. MFM-images of obtained spin ice states will be briefly discussed and analyzed. In addition to this, directions for further work to investigate such systems by MFM will be provided.

Spin ice systems get their name from an analogy to the way the polarity of water molecules arrange while in the crystalline water-ice phase. The spin ice system, however, does not have charge polarities that are aligned but rather spin polarities, or magnetic dipoles. Common to these systems are so-called frustrated states. This can be described as a system where there are several relaxed states and where there is some degree of high-energy configuration and no well-defined ground state, even at an absolute zero temperature.

These systems might have many interesting use cases, and among them is their use in unconventional computing. Unconventional computing is a new approach to computing that does not rely on the strict binary system with logic gates that conventional computers utilize. Instead, complex interactions and bits of intermediate values might provide computational systems that work in a fashion that more closely resembles the neural networks of the brain. This is a vast topic and it will not be covered in more detail here, as it suffices to say that such systems might be of tremendous interest in today's modern world and development towards artificial intelligence.

A spin ice system characteristically has components which have a well-defined magnetic moment. This can be implemented as small elongated magnets that have a moment directed along its length, but which may point in either of the two directions. Stacking such magnets leads to a spin ice system, where neighboring magnets orientation is affecting each other. One example of such a design is provided in Figure B.1.

The spin ice system fabricated in this thesis is based on the design in Figure B.1, with a separation $d = 100\,\text{nm}$, a length $l = 220\,\text{nm}$, and a width $w = 80\,\text{nm}$. In reality, a multitude of design parameters were fabricated, but this discussion will focus on the

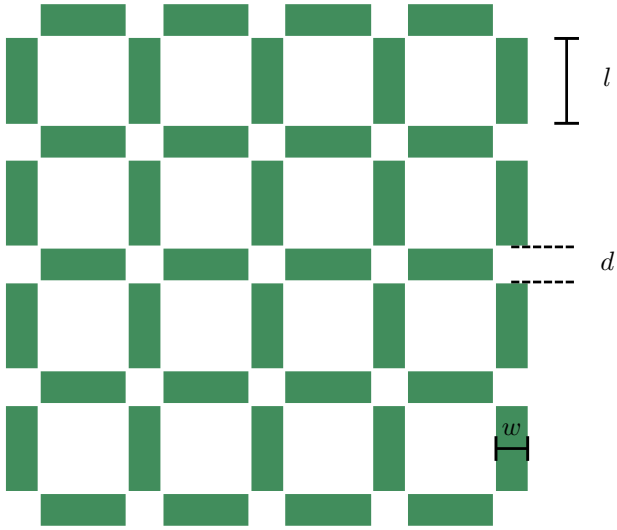

Figure B.1: Spin ice system design. The system consists of several long, rectangular magnets which will have a magnetization directed along their length. The indicated geometry parameters are usually on the order of a micrometer. The magnets are close enough to be dipolarly coupled, and thus their magnetization directions affect each other.

provided geometry parameters. The samples were fabricated in the same way as the disk ensembles from the main part of the thesis (in fact, the structures were fabricated on the same sample).

After fabrication, the samples were inspected with MFM in order to determine their state. An example MFM image of such a structure, and an analysis of its state is provided in Figure B.2. It is clear that this ensemble is not in the "ground state" as there are two broken magnetization loops.

There is much more that could be discussed and investigating regarding these spin ice systems. One of the purposes of this appendix is to demonstrate the ease at which a spin ice system's state can be identified with the available equipment. Further work that could be interesting to pursue is to do a statistical analysis of the states in the fabricated samples. To ease the data analysis, machine learning techniques could be applied in order to identify the direction of the magnetic dipoles.

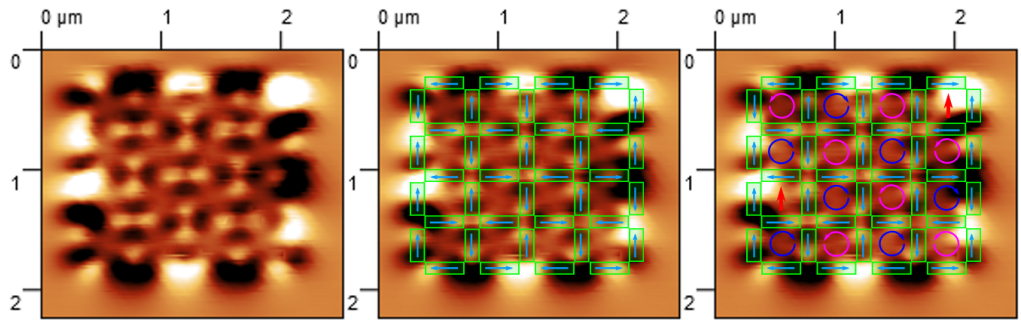

Figure B.2: Analysis of spin ice state obtained through MFM images. The left image shows the captured MFM image of a fabricated spin ice system. Discerning the state directly from the picture is not trivial. In the middle image, the structure of the fabricated spin ice is overlaid and this eases the analysis considerably. Additionally, arrows are drawn from dark to bright regions, indicating the direction of the magnetic dipoles. Once the state of the system, i.e., the orientation of the arrows, is determined, the state can be visualized by drawing the magnetic loops found in the system. In the right image, it becomes clear that there are two exceptions to the structure forming continuous magnetic loops, and these both have a net magnetization in the vertically up direction.